HYDROGEOLOGIC WINDOWS: REGIONAL SIGNATURE DETECTION FOR BLIND AND TRADITIONAL GEOTHERMAL PLAY FAIRWAYS

Final Report, October 16th 2015

Jeffrey Bielicki — The Ohio State University
David Blackwell — Southern Methodist University
Dylan Harp — Los Alamos National Laboratory
Satish Karra — Los Alamos National Laboratory
Richard Kelley — Los Alamos National Laboratory
Shari Kelley — New Mexico Institute of Mining & Technology
Richard Middleton — Los Alamos National Laboratory
Jeffrey Pepin — New Mexico Institute of Mining & Technology
Mark Person — New Mexico Institute of Mining & Technology
Glenn Sutula — The Ohio State University
James Witcher — Witcher & Associates

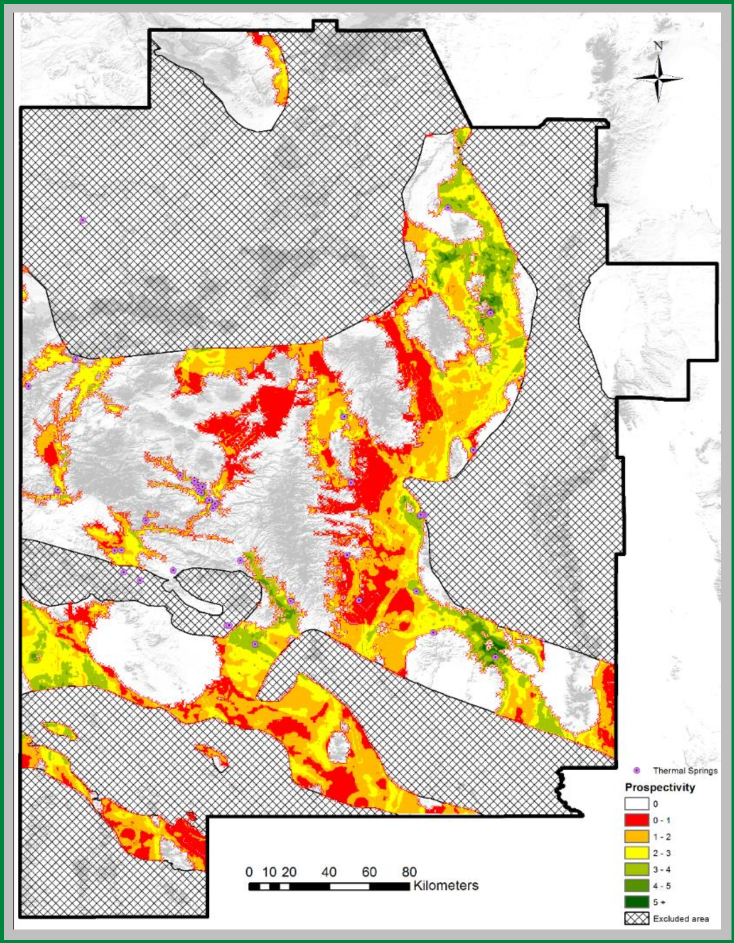

LA-UR-15-28360

TABLE OF CONTENTS

TABLE OF FIGURES

TABLE OF TABLES

Section 1. Executive Overview

The overarching goal of this project was to develop new ways to analyze available geologic, geochemical, and geophysical data to reduce the risk and increase the prospects of successful geothermal exploration and development. Data gathered during this project were organized and analyzed in the context of an integrated framework (Figure 2-4) that we developed in order to combine the data for various signatures of a geothermal resource into a cohesive analysis. Key data that were incorporated into the framework included structural information (earthquake location and magnitude, geophysical data, fault location and age, basement depth), topographic and water table elevations, conservative ion concentrations, and thermal information (heat flow, bottom hole temperature, discharge temperature, and basement heat generation). ArcGIS layers were produced for each type of data and those layers were combined to create structural analysis, slope, geothermometry, and thermal maps. In addition to these standard maps, we created two unique layers, a subcrop map and a discharge map (Figure 2-7), that proved useful in identifying known geothermal systems and helped narrow the search for new geothermal prospects. Possible erosionally- or structurally-controlled breaches in regional-scale aquitards are located using the subcrop map; these breaches form the basis of the hydrogeologic windows concept (Figure 2-1and Figure 2-6). The elevation of groundwater discharge through modern thermal springs or paleo-thermal springs is constrained by the discharge map. When these two maps are combined, large areas outside the hydrogeologic windows and above the groundwater discharge elevation are eliminated from further exploration. The remaining ArcGIS layers were created from the results of a new method for spatial association analysis that we developed for this project. This new methodology was applied to the numerous types of data to determine their relationships with known geothermal sites. The mapping efforts ranked prospects at low elevation inside hydrogeologic windows. Each layer was assigned a relative score between 0-1. The different spatial analyses were then added together. The prospectivity index varied between 0-6, with 6 indicating highest geothermal potential. The mean value of the prospectivity value for known hot springs and geothermal wells was 3.6. Although we focused our efforts on southwestern New Mexico, the framework, workflow, and prospectivity ranking developed here can be broadly applied to other arid areas in the southwestern United States and elsewhere.

We also tested the utility of two new exploration techniques based on the principles of advective-dispersive solute transport of the geochemical tracers boron and lithium. Elevated boron concentrations are commonly associated with geothermal resources in our study area. About 4000 wells that have boron data within our study area were available to us. Hot springs and geothermal wells had a median boron concentration of about 0.5 mg/L which is significantly higher than background (median) levels from all wells (0.05 mg/L). We extended the use of reverse particle-tracking techniques to help locate new geothermal systems. Our approach places mathematical particles at the location of wells containing geochemical tracer data. The algorithm then moves those particles up gradient perpendicular to the water-table elevation contours to determine where they enter the hydrogeologic system. Adjacent particles of contrasting geochemical tracer concentration but similar trajectory may indicate a zone of geothermal upwelling or a hydrogeologic window. The method was tested on the well-understood Socorro-La Jencia Basin geothermal system. The approach successfully identified a broad region containing the known hydrogeologic window, although the analysis was hindered by an insufficient number of up-gradient wells in the La Jencia Basin that have geochemical data. When applied to other domains, the particle-tracking analysis identified a potential prospect along the Comanche Fault in the Lucero uplift, and another along the Gila River near Cliff-Riverside. We also developed forward models of the Acoma basin region using an advective-dispersive transport model. We computed the steady-state boron concentrations for 625 potential geothermal upflow zones and computed the root mean squared error using all available wells with measured boron concentrations. The approach plausibly located the most likely (lowest error) upflow zone to be to the east of the Comanche Fault near the Lucero uplift. Both approaches suffered from a scarcity of available geochemical data. Lithium modeling, in particular, turned out to provide rather inconclusive results due to a lack of widespread concentration data. These methodologies can be further tested during Phase II by collecting additional boron and lithium data from existing wells in the region that have not previously been sampled.

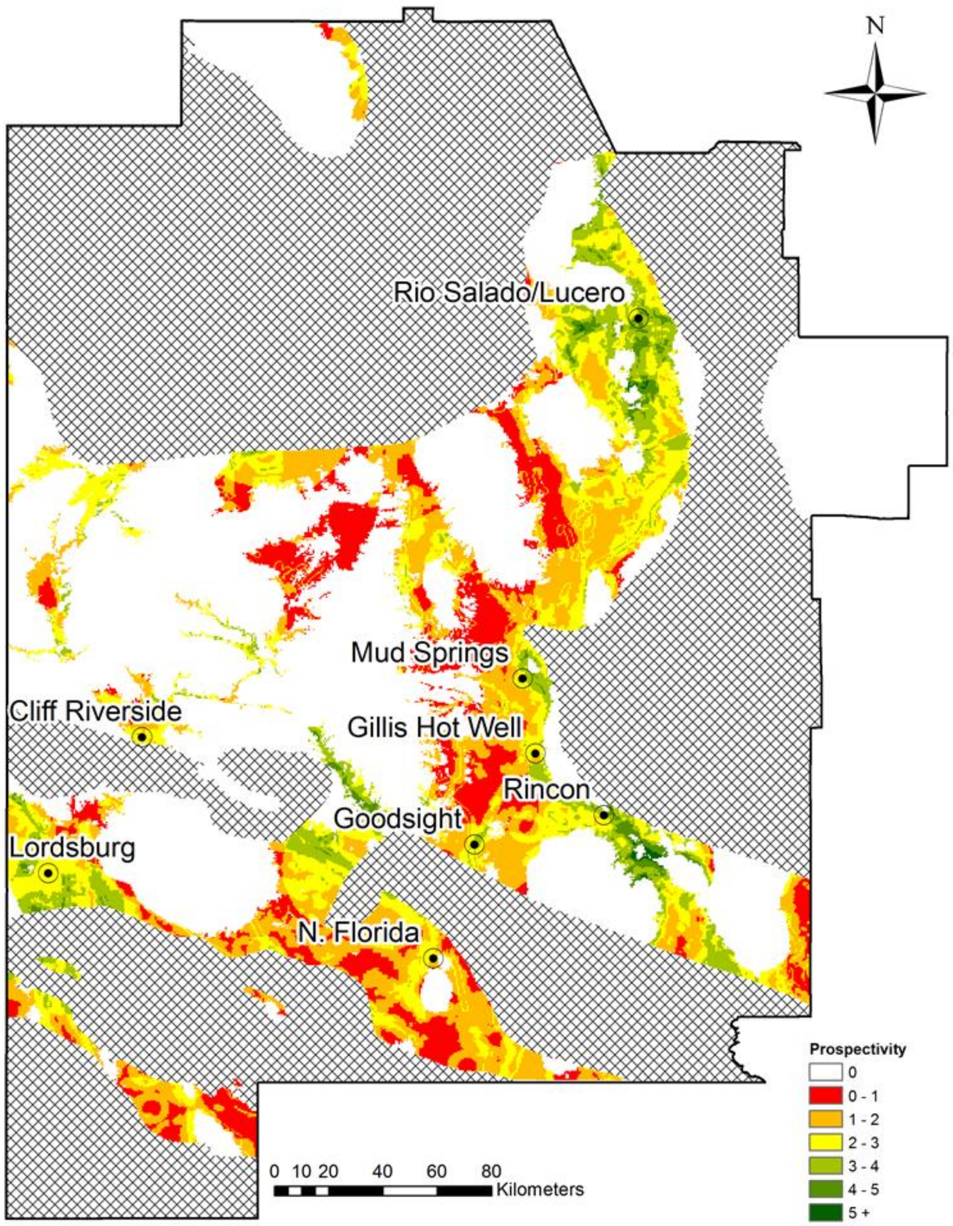

Three preliminary cross-sectional hydrothermal models were developed for Rincon, Acoma basin, and San Acacia study areas. The latter region overlies the Socorro magma body. The Rincon system is associated with a relatively narrow fault controlled hydrogeologic window while the other two models have zones about 2-3 km wide where crystalline basement rocks are at the surface. Model results suggest that fault controlled discharge, such as at Rincon, produce higher temperature resources (up to 85 ºC at less than 200 m depth) while crystalline basement hydrogeologic window provide lower temperature geothermal resources (between about 40 to 47 ºC at less than 100 m depth) because discharge is less focused. These models help to validate, in part, the hydrogeologic windows conceptual model.

Section 2. Phase I Final Report

2.1 Introduction

This project seeks to reduce exploration risk and identify new prospective targets using available geologic, geochemical, and geophysical data sets that are commonly gathered during geothermal exploration. These data include structural information that provide indications of permeability and fluid volumes (e.g., mapped faults, gravity and magnetic data, earthquake locations) and thermal data that constrain the heat content of a resource (e.g., heat flow, bottom-hole temperature data, groundwater discharge temperature). During the course of this project, we developed and applied a framework to organize and efficiently analyze these data to create prospectivity maps that quantitatively indicate the potential of a geothermal resource being present in a location.

We developed two unique ArcGIS layers that were particularly effective in narrowing the search for new geothermal prospects. One layer, called a subcrop map, is used to locate possible erosionally- or structurally-controlled breaches in regional aquitards, which are referred to as hydrogeologic windows. A second layer, called a discharge map, identifies the elevation at which modern and paleo-thermal springs discharge at the surface. Large areas outside of the hydrogeologic windows and above the groundwater discharge elevation are thus eliminated from further exploration.

Although the focus of this project is on southwestern New Mexico, the techniques that were developed during this project are widely applicable elsewhere, particularly in arid regions. In these settings, the character of geothermal systems largely varies and is often not well understood. Locating geothermal resources in these regions is usually difficult, as surface thermal manifestations are rare. New Mexico is endowed with relatively high geothermal potential. The Rio Grande rift is especially promising, as it is both tectonically and volcanically active and has several known commercial scale geothermal systems. There is no doubt that additional geothermal resources exist in New Mexico. It is our intention to develop tools, such as the subcrop and discharge maps, that make locating these systems simpler and less expensive.

Another key concept of this project is the analysis of conservative ion data using reverse particle-tracking (upwinding) and advective-dispersion models to locate the source of geothermal plumes. Although we learned that these techniques highly depend on our understanding of the configuration of the water table and on the spatial distribution of the sampled wells, we believe that these methods can be widely applied in geothermal exploration to narrow the search for prospective areas.

We also developed a new method to understand the spatial relationship (i.e., spatial association) between various signatures of the presence of a geothermal resource and the locations of known geothermal sites. While many analyses may focus on individual sites or the characteristics of particular locations, this methodology was applied across observations of signatures and known geothermal sites to develop the prospectivity map. This prospectivity map was better able to identify known and potential geothermal resources than other approaches with a reduced number of signatures.

We begin the report by describing the hydrogeologic window concept in the context of the regional scale geologic history of southwestern New Mexico. This concept can be modified for other areas with similar (Colorado) or different (Nevada, Utah) geologic histories and settings. We next describe the integrated framework, the data used in this analysis, and the methods used to create the ArcGIS layers. We then present hydrogeologic cross-sectional models developed for two known geothermal resources and two poorly understood prospect. Next, the particle-tracking and advection-dispersion concepts are explained and the results of this analysis are discussed. Finally, the details of the methods used to create the propectivity maps are presented, along with their results.

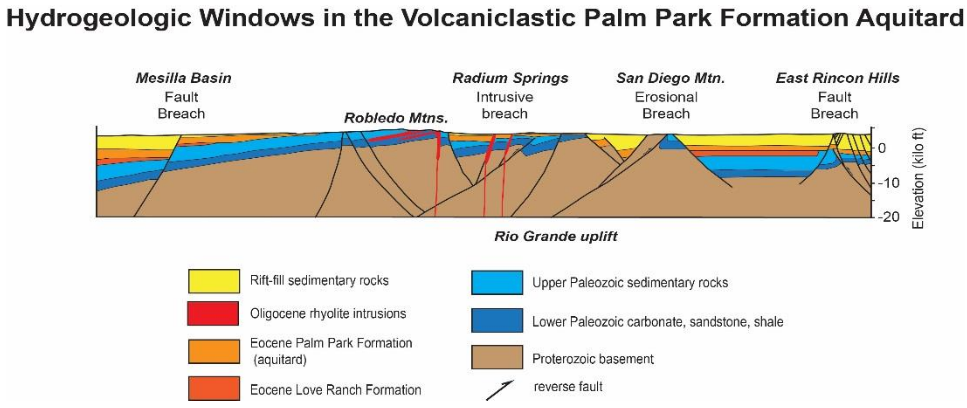

Figure 2-1: Cross-section, modified from Seager, et al., (1987) highlighting the three main types of hydrogeologic windows. The location of this cross-section is illustrated on Figure 2-2.

2.2 Background

2.2.1 Hydrogeologic Window Fairway Play

Our geothermal play focuses on advective geothermal systems in southwestern New Mexico that occur within the Rio Grande rift (RGR), in the southern Basin and Range (SBR), and along the eastern margin of the Colorado Plateau in a cratonic crust with a relatively thin Phanerozoic cover. The known geothermal systems in southwestern New Mexico do not tend to have a magmatic component. Instead, the geothermal systems in this area are gravity-driven systems with recharge in the highlands and groundwater discharge at low elevation (Smith and Chapman, 1983) from hydrogeologic windows. A hydrogeologic window is an area regional aquitards are erosionally thinned or breached by intrusions or faulting (Witcher, 1988; Figure 2-1). For example, sub-vertical dikes form a hydrogeologic window at Radium Springs, NM along the Rio Grande (Figure 2-1; 100°C at 241 m; Witcher, 2001; Witcher and Lund, 2002) and the juxtaposition of aquitards and aquifers across a permeable fault zone forces 85°C fluids into a shallow outflow plume at Rincon, NM (Witcher, 1998). These gravity-driven systems pick up heat and chemical constituents along their flow paths within fractured reservoirs at depth. In New Mexico, the fluids are heated by the elevated heat flow within the thinned crust of the Rio Grande rift. Crustal heat flow in this region ranges from 70 to 105 mW/m^2 (Reiter et al., 1975). Crustal thickness is 40 km on the margins of the rift and is 26 km near the axis of the rift (Wilson et al., 2004). This conceptual model is based on a number of prior studies in the southern Rocky Mountains and in the southern Basin and Range/ Rio Grande rift. (Witcher, 1988; Barroll and Reiter, 1995; Mailloux et al., 1999; Morgan and Witcher, 2001; Pepin et al. 2015).

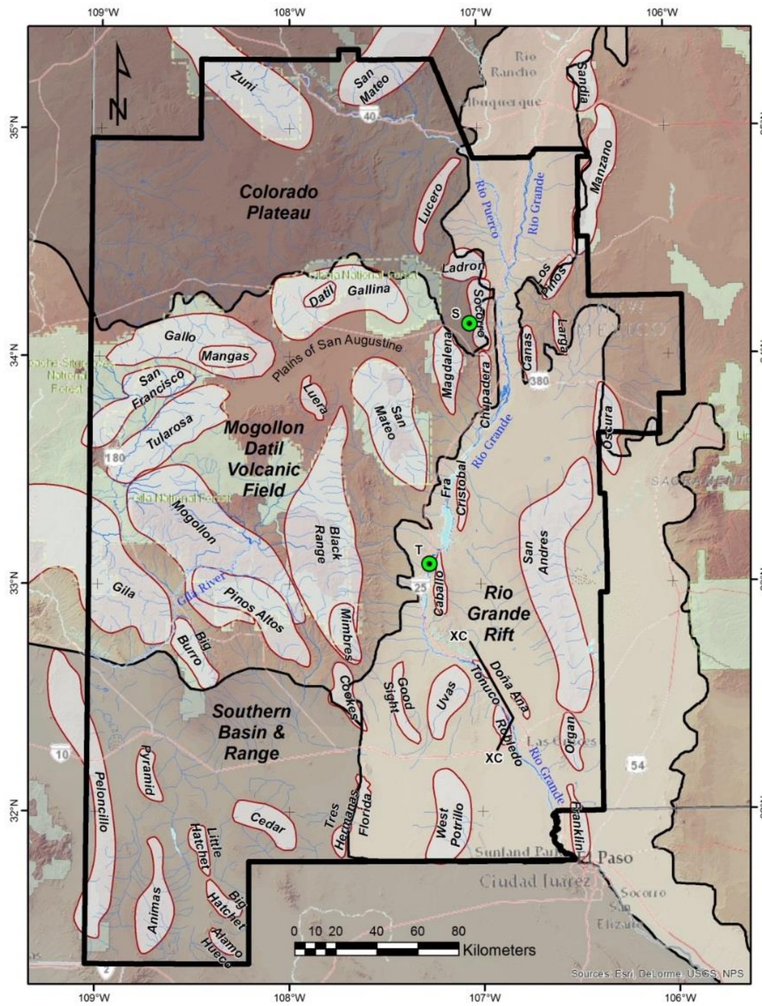

Figure 2-2: Map illustrating the major mountain ranges, drainage systems and physiographic provinces of southwestern New Mexico. "S" = La Jencia-Socorro geothermal system, "T" = Truth or Consequences geothermal system, and the cross-section in Figure 2-1 is shown by the dark line titled "XC".

This type of system is perhaps best illustrated within the Socorro-La Jencia Basin geothermal system in central New Mexico on the western margins of the Rio Grande rift (Barroll and Reiter, 1991). The uplands of the La Jencia Basin have unusually low heat flow (25-50 mW/m^2) consistent with a groundwater recharge area (Smith and Chapman, 1983). The groundwater discharge area occurs at the base of Socorro Peak where bedrock crops out and heat flow exceeds 400 mW/m^2. An important feature of this conceptual model is that geothermal groundwater flows within not only permeable sedimentary facies but also within fractured crystalline rocks. Using hydrothermal modeling, Mailloux et al. (1999) and Pepin et al. (2015) estimated that the effective permeability of the crystalline basement ranges between 10^{-14} to 10^{-12} m^2 (10 to 1,000 mD) at depths of 4-8 km in segments of the Rio Grande rift in south-central New Mexico. A recent aquifer test conducted this summer revealed significantly elevated permeabilities (5×10^{-10} to 2×10^{-12} m^2) in fractured Precambrian basement rocks near a significant fault zone that influences the location of the Truth or Consequences, NM geothermal resource (Person and Witcher, unpublished data,

2015). This reinforces the importance of identifying high permeability fracture networks that influence flow paths and groundwater discharge in gravity-driven systems.

The Rio Grande rift and southern Basin and Range of New Mexico form a unique and important geothermal province in the Western United States. The region is nationally recognized as a leader in the economic development of large-scale, direct-use greenhouses and aquaculture; this area offers huge potential for further development. Recent installation of small-scale commercial power production with a binary plant highlights potential for modest power production. Ormat Technologies, Inc (ORMAT) has a Bureau of Land Management exploration lease near Rincon, NM and is actively assessing the region's geothermal potential.

Up to a quarter of the known geothermal systems in this area had no surface discharge expression prior to their drilling and accidental discovery. Later in this report, we demonstrate that these known blind systems often coincide with hydrogeologic windows, like those illustrated in Figure 2-1.

2.2.2 Regional Geologic Setting

The Proterozoic basement in southwestern New Mexico is composed primarily of 1.6 to 1.7 Ga metatvolcanic, metasedimentary, and plutonic rocks. The Proterozoic rocks originally were volcanic rocks, sandstone, and shale deposited in an extensional basin about 1.65 to 1.60 billion years ago. These volcanic and sedimentary rocks were buried, deformed, and heated during an arc-related mountain building event about 1.6 billion years ago. Later, 1.4 Ga granite intruded into the older metamorphic rocks that had formed in the roots of this ancient northeast-trending ~1.6 billion year-old mountain belt.

After a long period of erosion, a shallow ocean covered the region starting about 510 million years ago. Shallow seas advanced and retreated across the area several times between 510 and 340 million years ago, depositing first sandstone (Cambro-Ordovician Bliss Sandstone), then limestone and dolomite (Ordovician El Paso and Montoya formations and Silurian Fusselman Dolomite), and finally shale (Percha Shale), until the second mountain building event, Ancestral Rockies deformation, began. These early Paleozoic units are preserved in the southern part of the area of interest; they pinch out northwestward about halfway across the study area. The Ordovician to Silurian carbonates form regional-scale karstic aquifers and the Percha Shale is a regional-scale aquitard (Figure 2-3).

Late Paleozoic Ancestral Rocky Mountain uplifts trend north to northwest and are separated by basins that are filled with both marine sediments and sediments shed from the adjacent highlands. Rocks older than early Mississippian in age (>340 million years old) were tilted toward the southeast and eroded prior to deposition of early Pennsylvanian limestone and shale about 312 million years ago. In the early stages of this tectonic episode, shallow seas persisted in the region until ~290 million years ago, when sea level dropped and rivers started to flow southward across the area (Abo Formation). The Abo Formation, away from the axial channel sandstone deposits, is typically fine grained and this unit tends to be an aquitard (Figure 2-3). The margin of the ocean returned late in Permian time and moved back and forth across the area, depositing limestone, dolomite, gypsum, and sandstone (Yeso Formation; Figure 2-3). Fractured limestones in the Yeso Formation can form local aquifers, but generally water quality in these aquifers is poor. The shallow marine to marginal marine Permian San Andres Limestone and Glorieta Sandstone were deposited on the Yeso Formation; these two units form an important aquifer throughout southwestern New Mexico (Figure 2-3).

Most of the Mesozoic section in the study area was either never deposited on or was eroded from the areas north of the "bootheel" of New Mexico, because this area was a highland on the flank of a northwest-trending Jurassic rift basin known as the Bisbee Basin. Deposition persisted in this basin until Middle Cretaceous time. Total structural relief between rift shoulders and the base of the rift deposit is on the order of 500 m. Lawton (2000) highlighted two distinct processes associated with the depositional history of the basin. The lower Bisbee Group rocks (including the U-Bar Formation; Figure 2-3) were deposited as the basin subsided during extension. These rocks include 1 km of shallow marine deltaic sedimentary rocks and 200 m of mafic lava flows. The younger Mojado Formation accumulated as the basin thermally subsided while the crust cooled after Jurassic to Early Cretaceous rifting. The upper Bisbee Group is composed of intercalated shallow marine and continental rocks. Upper Cretaceous rocks lapped onto and buried the basin and the rift shoulder. The Upper Cretaceous rocks preserve a history of the oscillating landward and seaward migration of the shoreline of the Western Interior Seaway across this area about 95 to 80 million years ago.

The third mountain building event, the compressional Laramide deformation began in late Cretaceous time and reached its peak during Eocene time, forming northwest-trending uplifts and basins that followed the trend of the earlier Jurassic to Cretaceous rifting event. Many of the NW-trending normal faults associated with Jurassic rifting were reactivated as reverse faults during Laramide deformation (Lawton, 2000).

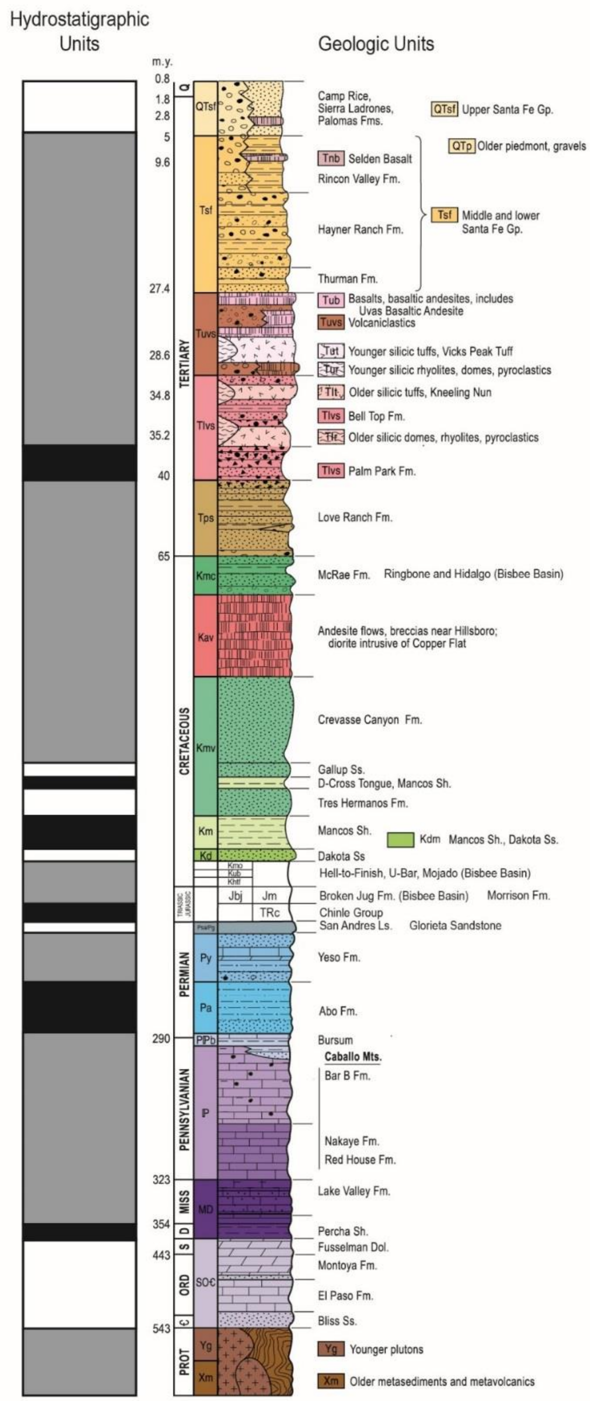

Figure 2-3: Generalized stratigraphy of southwestern New Mexico modified from Wilkes (2005). The column to the left highlights the general hydrostratigraphic characteristics of the units. Black = aquitard; white = aquifer; gray = localized or fair aquifers, especially when fractured.

Large andesitic stratovolcanic centers developed in the Mogollon-Datil volcanic field at 38 Ma, shedding debris flow and laharic aprons that form tight aquitards on top of the older Laramide highlands and basins (Figure 2-3). Starting at 36 Ma, caldera eruptions blanketed the area with rhyolitic tuff and tuffaceous volcaniclastic sediments, while basaltic andesite from shield volcanoes and fissure eruptive centers flowed across the region.

Mack et al. (1994a, b) propose that the southern Rio Grande rift has been affected by three episodes of extension beginning at about 36 Ma. The main phases of faulting include (1) latest Eocene to late Oligocene minor faulting coincident with extensive volcanism, (2) late Oligocene to late Miocene rapid extension with minor volcanism, and (3) latest Miocene to early Pliocene continued faulting and volcanism, with each phase disrupting earlier rift basins, and in some cases, reversing the dip of the early rift half-grabens.

2.2.3 Regional Physiographic setting

Our study area encompasses southwestern New Mexico and includes the southern Rio Grande rift, the southern Basin and Range, and the southeastern Colorado Plateau (Figure 2-2). Narrow ranges bound by normal faults that are separated by basins filled with deposits derived from the adjacent highlands characterize both the RGR and SBR provinces. The basins between the ranges tend to be deeper in the Rio Grande rift compared to the southern Basin and Range, and the number of Quaternary faults and youthful volcanic fields (<1 Ma) is greater within the rift. The southeastern Colorado Plateau is a relatively undeformed plateau occasionally interrupted by sharp monoclines and gentle folds. The preserved thickness of the Mesozoic section increases toward the north on the Colorado Plateau. The diverse landscape and structural setting in these three provinces provide an excellent laboratory for developing our exploration framework. Significant highlands in the area include the mountains capped by deposits from the Eocene to Oligocene Mogollon-Datil volcanic field (e.g., Mogollon Mountains, Black Range, Tularosa, and San Mateo), which straddles the Colorado Plateau – RGR and SBR boundaries (Figure 2-2). Other highlands are the Laramide Zuni uplift on the Colorado Plateau, the flanks of the RGR, and narrow ranges of the SBR (e.g., Animas, Big and Little Hatchets; Figure 2-2).

Most of the region is traversed by the regional ocean-integrated drainage of the Rio Grande and Gila River and tributaries. Exceptions are the Mimbres, Playas, and Animas valleys of southwest New Mexico, and the Plains of San Augustin in west- central New Mexico, where large playas form in the structural and topographic termination of local drainage. All of the through-going drainage shows Quaternary entrenchment into Miocene to Quaternary basin fill (Figure 2-2).

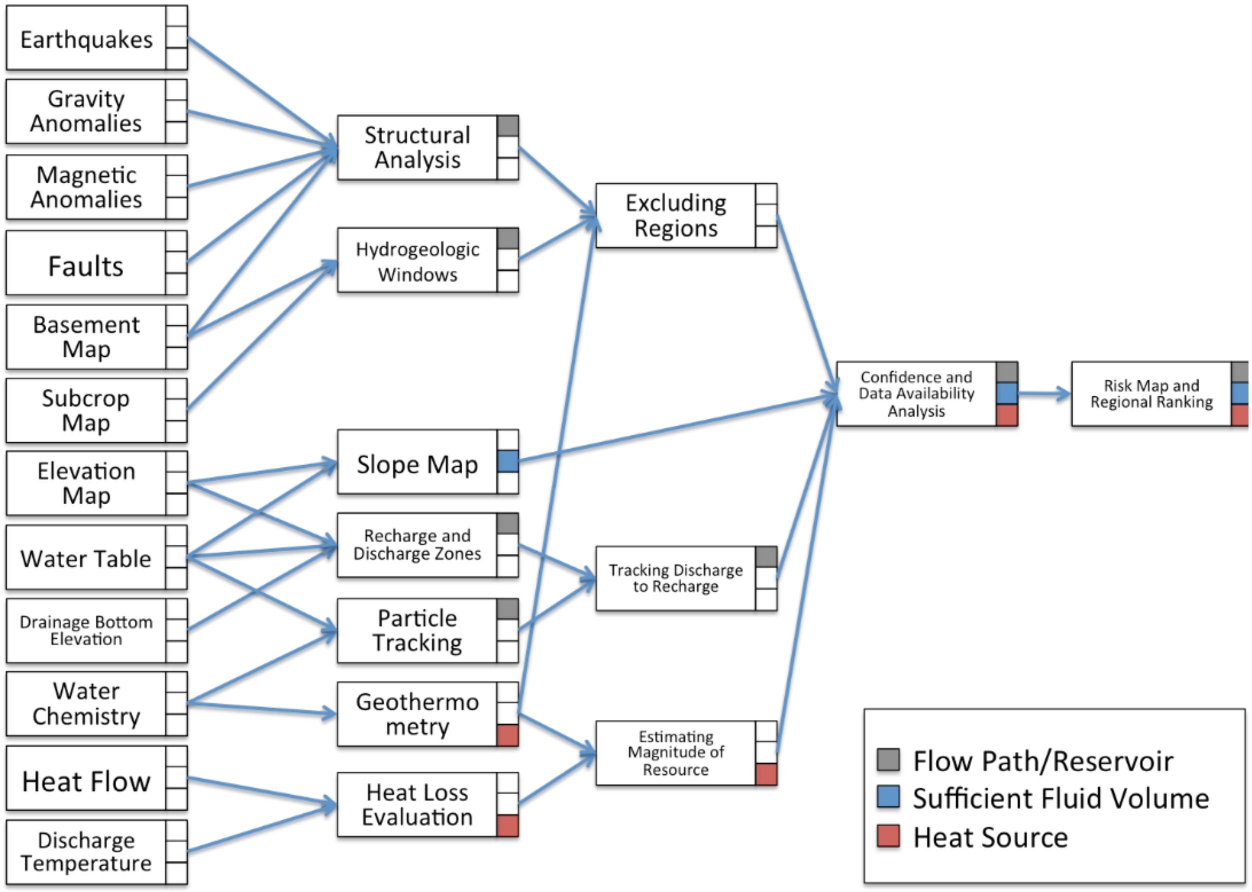

Figure 2-4: The integrated framework for identifying blind geothermal prospects with the hydrogeologic windows concept. Permeability is incorporated into the "Flow Path/Reservoir" category. See section 2.5 for details.

2.2.4 Data Sources and First-Order Observations

The data used in this investigation are organized in an integrated framework according to the three requirements needed to develop an economically viable hydrogeologic window geothermal resource: permeability, water, and heat (Figure 2-4). The structural analysis and subcrop/hydrogeologic windows analysis are used to characterize permeability. The geomorphic analysis of recharge and discharge, and the water table and water chemistry/particle-tracking/hydrogeologic modeling identify possible flow paths and potential water volume. Heat flow, geothermal gradient, and groundwater discharge temperature can also be used to estimate the thermal content of the resource. Using this framework, we will identify likely windows, estimate the amount of discharge and heat content of each potential window, and locate the most likely path taken by the fluid in the window. In addition, the framework will used to establish regions that do not contain hydrogeologic windows. The framework is discussed in detail in Section 2.5.

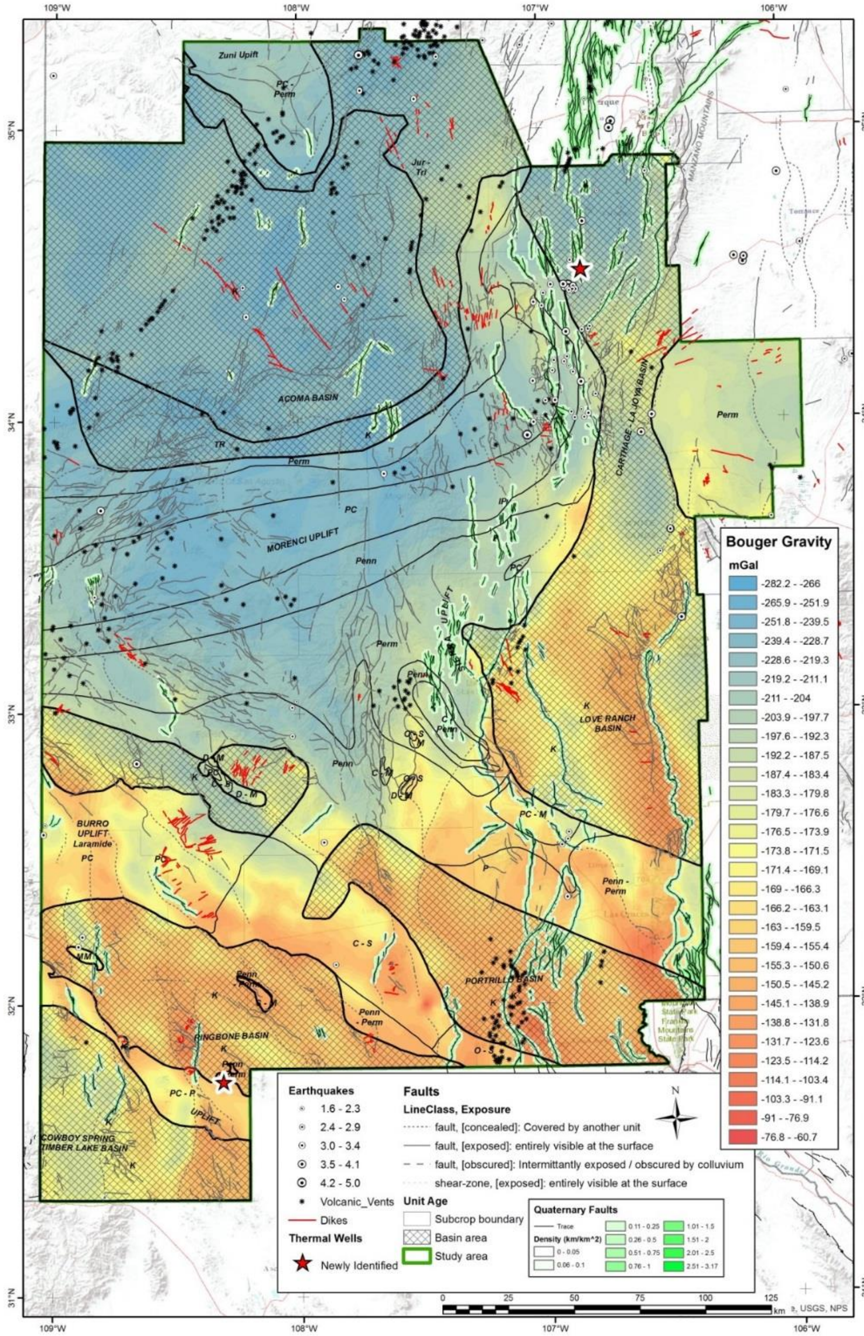

Figure 2-5: Structural analysis map that includes Bouguer gravity, earthquakes, Quaternary and older faults, Quaternary and older volcanic vents, and dikes, which is superimposed on the subcrop map (see Section 2.2.6). Newly discovered thermal wells identified during analysis of data during this study are denoted by red stars.

2.2.5 Structural Analysis Maps

Faults and fault intersections play an important role in the forming the plumbing of geothermal systems in the Basin and Range (Coolbaugh et al. 2005; Vice et al. 2007; Person et al. 2012). A series of ArcGIS layers used for fault identification and structural analysis that include regional-scale gravity and aeromagnetic data from the UTEP PACES and USGS web sites, depth to Proterozoic basement, Quaternary and older faults, Quaternary and older volcanic vents, dikes, and earthquakes have been prepared to locate avenues of high permeability in the vicinity of hydrogeologic windows (e.g. Figure 2-5). Gravitational and magnetic anomalies provide information about the depth of potential resources and can be used to identify buried intrusions while gravity first-derivative maps can help locate buried faults. The Proterozoic basement map reveals areas that have been uplifted, resulting in increased permeability as aquitards are eroded. Here we present just one of a series of three maps that use gravity, magnetics, or depth to basement as a base. Limited and localized published MT and resistivity data for New Mexico (Jiracek et al., 1977, 1983; Hohmann and Jiracek, 1979; Jiracek, and Mahoney, 1981; Ander et al., 1984) have been compiled and are incorporated into the analysis at a local scale.

2.2.6 Subcrop Layers

Subcrop mapping is used to identify potential hydrogeologic discharge and recharge windows on a regional scale. Discharge hydrogeologic windows are zones at relatively low elevation where regional or local aquitards are thinned or breached by faulting, erosion, or fractured intrusions, allowing relatively rapid vertical flow of geothermal water toward the surface. We use our understanding of the geologic history of a region and our knowledge of the specific structural and stratigraphic-tectonic packages associated with major geologic events (Section 2.2.2) to locate the places where regional aquitards have been stripped by erosion or penetrated by faults or intrusions. By analyzing these layers we can exclude large areas within our study region that do not fit the criteria for a hydrogeologic window (Figure 2-6).

The hand-crafted Laramide subcrop map made by James Witcher in 1988 has been updated in ArcGIS using the geologic map of New Mexico (NMBGMR, 2003) and formation top data stored in the NMBGMR NMWells database. New geologic mapping (e.g., Jochems et al., 2014) was also incorporated into the subcrop map (Figure 2-6). Rock units below the Eocene-Oligocene unconformity were identified and the landscape preserved beneath the unconformity following Laramide deformation in southwestern New Mexico was mapped. Cretaceous basins filled with intercalated fine-grained sedimentary rocks that act as aquitards and thin sands that serve as minor aquifers are shown in the green-cross hatched pattern; these areas are not likely to have windows. Possible hydrogeologic windows in the northwest striking Proterozoic- to Paleozoic-cored Laramide highlands are shown in shades of brown, pink, and blue. Areas where the Devonian Percha Shale aquitard has been stripped from Ordovician to Silurian karstic carbonate aquifers (Jochems et al., 2014) are among the best targets. Note the close association of known thermal springs with the windows (yellow dots in Figure 2-6). As mentioned earlier, the Lower Paleozoic aquifers pinch out south of the Morenci uplift and thus are absent in the northern part of our area of interest.

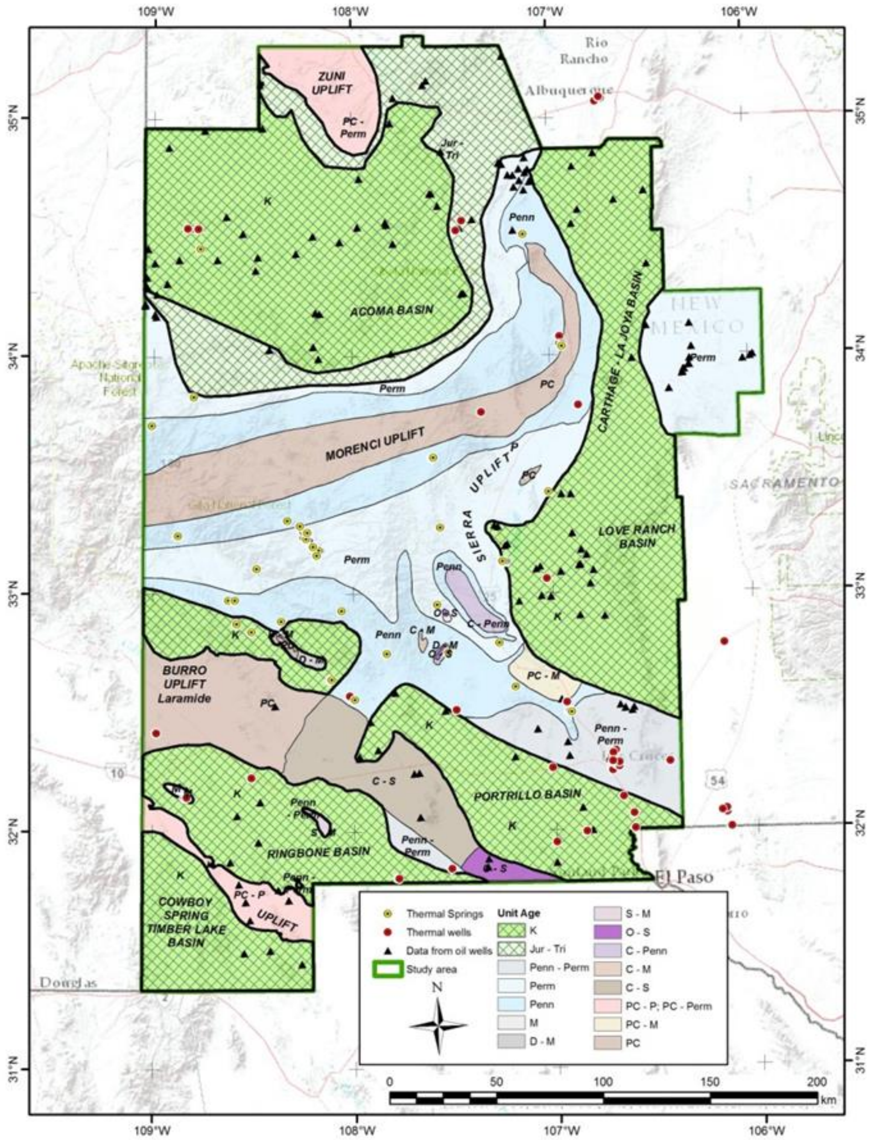

Figure 2-6: Subcrop map depicting the landscape at the end of Laramide deformation, just prior to deposition of Eocene to Oligocene volcanic and volcaniclastic rocks from the Mogollon-Datil volcanic field. The various colors depict the rock unit or units that lie below the unconformity. The NW-striking fabric of southwestern New Mexico is inherited in part from Jurassic rifting associated with the formation of the Bisbee Basin.

The target karstic aquifer in the northern part of the area along the Colorado Plateau-Rio Grande rift boundary is the Permian San Andres Limestone, which lies below a significant unconformity that formed prior to the deposition of the Triassic Chinle Formation, a silty aquitard. The San Andres Limestone is karstic in this area because of the long pre-Chinle exposure of the unit at the surface. The San Andres Limestone and underlying Glorieta Sandstone are the main aquifers in the Acoma Basin on the eastern margin of the Colorado Plateau (Frenzel, 1992; Baldwin and Anderholm, 1992). The Laramide Zuni uplift, the Acoma basin, and the Lucero uplift (Figure 2-2 and Figure 2-6) form the recharge area, flow path, and discharge zone, respectively, for the San Andres Limestone–Glorieta Sandstone aquifer system. The Acoma Basin lies in the transition zone between the Colorado Plateau and the Rio Grande rift and has been the site of several <5 Ma basaltic eruptions along the Jemez lineament. A combination of Laramide reverse faulting and Rio Grande rift normal faulting have created possible windows bringing both the San Andres/Glorieta aquifer and the Proterozoic basement to or near the surface on the eastern side of the Lucero uplift (Figure 2-2 and Figure 2-6).

2.2.7 Geomorphology Analysis for Groundwater Discharge and Recharge

Forced convective or advective heat flow results from ground water flow driven by water table elevation differences. Advective ground water flow is characterized as gravity driven flow (Hubbert, 1940, Toth, 1963, Freeze and Witherspoon, 1967) that is modified by the hydraulic conductivity distribution, the geometry of subsurface rock units, and thevertical and lateral scaling of the host basins. The associated water table elevations generally mimic topography, especially on regional scales. Advective or forced-convective geothermal systems are regional ground water systems that sweep-up heat and chemical constituents along the flow path where the basin or preferred flow path dimensions are favorable for deeply penetrating flow (Domenico and Palciauskas, 1973).

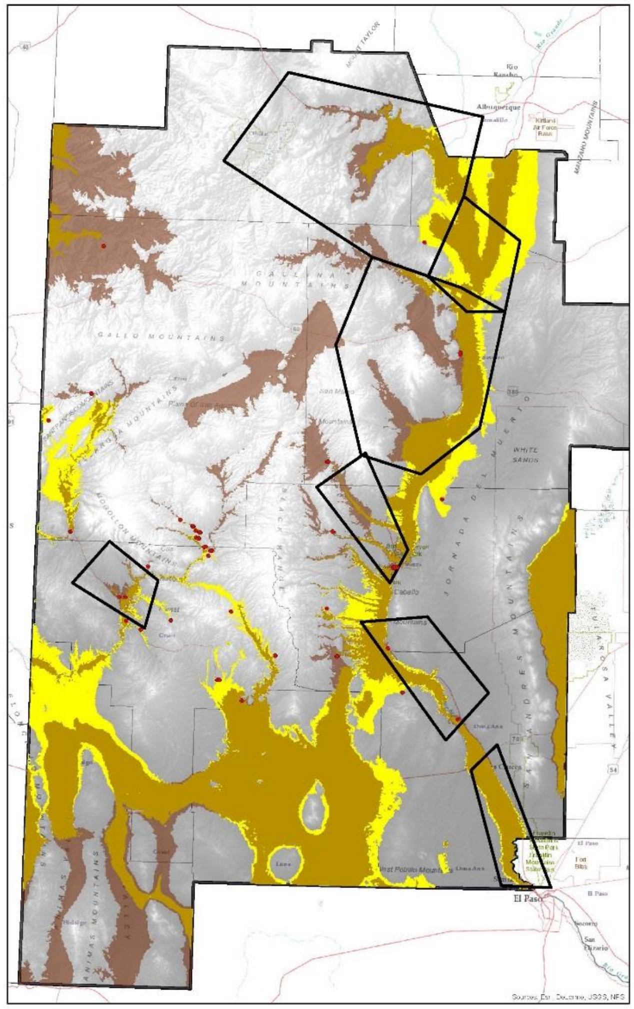

Figure 2-7: Location of water table discharges in lowlands based on the locations of third-order streams and water table lowlands (brown shaded relief pattern). Yellow contours show topographic lowlands based on hot spring elevations. Hot spring locations are shown with red circles and are systematically found in lowlands. The black lines denote sub regions where particle-tracking analysis was performed.

Advective ground water flow systems are commonly classified as local, intermediate, and regional ground water systems (Toth, 1963). Advective geothermal systems represent regional ground water systems with significant lateral and deeply-penetrating flow.

From a geomorphic standpoint, well-drained basins show local, intermediate, and regional attributes that are primarily characterized by different classes of valleys drained by permanent or ephemeral streams that feed increasingly larger valleys or streams (Horton, 1945; and Strahler, 1952). Applying the concepts of Toth (1963), upper and smaller valleys or streams would be underlain by local and intermediate advective ground water flow systems at shallowest subsurface depth and the largest valley or main trunk drainage would generally define the groundwater discharge of a regional advective ground water system that is recharged in the domain characterized by the smaller drainages. In this geomorphic context, potential recharge zones and discharge zones for advective geothermal flow systems are delineated as an interpretive layer to identify active hydrogeologic windows.

A comparative regional discharge elevation surface (RDES) was constructed using the elevation of the main trunk regional stream channels. The surface include the Rio Grande, Gila, San Francisco, Rio Puerco, and Mimbres channel elevations (Figure 2-7). Large feeder drainage channels of the next lower Strahler order number are also used. These drainages have significant length and low gradients.

A plot of thermal spring elevations shows they are near and slightly above the elevation surface constructed for the major drainages. In addition, paleo hot spring deposits of Quaternary age occur with several geothermal systems and are located as much as 300 ft above the present day Rio Grande channel elevation (yellow shaded pattern in Figure 2-7) as a result of regional drainage integration to the Gulf of Mexico that was followed by entrenchment of the river roughly 700,000 years ago (Jarvis and others, 1998; and Mack and others, 2012).

For closed basins that are not integrated into the region's drainage framework, elevations of the lowest constructional surface, such as playas and major internal longitudinal drainage, are combined with channel elevations to construct the groundwater discharge elevation surface.

The regional discharge elevation surface (RDES) plus 300 ft is subtracted from the regional DEM topography and the area delineated below the topographic high residual represents the area with highest potential for discharge hydrogeologic windows. The area represented by the topographic high residual, especially at elevations above 6,000 feet and where highly dissected by low Strahler order number drainages, represents potential for hydrogeologic recharge windows for regional advective geothermal systems.

In addition to low-land delineation, we also estimated the amount of recharge within a watershed in order to estimate the vigour of groundwater circulation. The Eakin (1966) method for recharge is applied to estimate order of magnitude fluid fluxes across potential recharge hydrogeologic windows by determining the regional change in annual precipitation with altitude for the Basin and Range and Transition Zone (Mogollon-Datil) of southwest New Mexico and applying an elevation dependent percentage of annual rainfall to estimate annual recharge. The areal extent of discrete elevation steps (ft^2) is multiplied times the annual recharge (ft) and divided by 43,560 to determine acre-ft of recharge.

2.2.8 Water Chemistry/Geothermometry

Nature of conservative ions. Conservative trace element analysis is commonly used in geothermal exploration (Arehart and Donelick, 2006) because rock-water geochemical reactions at temperatures above 100 °C liberate these elements. Lithium, boron, and bromide are among the trace elements that are known to correlate with chloride-dominated geothermal waters within the Basin and Range of Nevada and the Rio Grande rift of New Mexico (Arehart, and Donelick, 2006; Owens, 2013). The approach assumes that the conservative ion tracers are retained in relatively high concentrations as they flow upwards from a geothermal reservoir into comparatively cool, water-table aquifers. For example, a plume of hydrothermal fluids in the Socorro Basin at the base of Socorro Peak in central New Mexico cools as it moves laterally toward the Rio Grande to the east and south (Figure 2-2 and Figure 2-8), but lithium and boron are retained at relatively high concentrations (~ 0.1 mg/l) in non-thermal water supply wells (Owens, 2013). The highest lithium concentration in the Socorro system (0.97 mg/l; Owens, 2013) is found within the

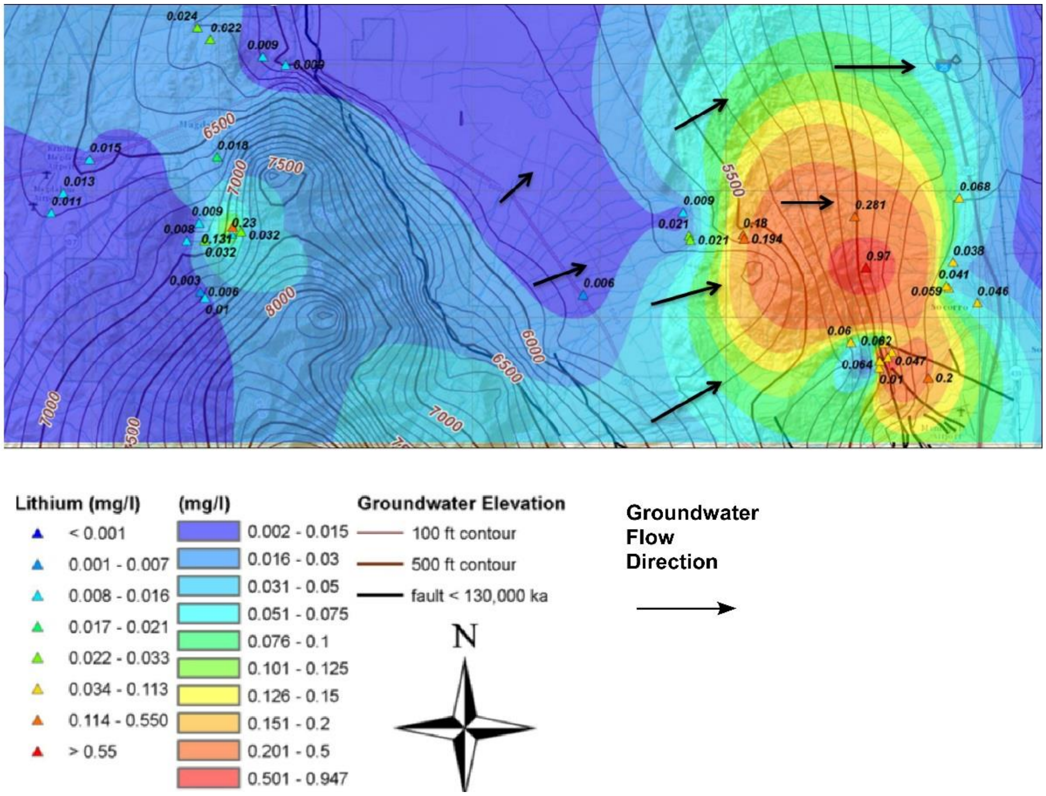

Figure 2-8: Lithium outflow plume originating within the region of high heat flow within the Socorro geothermal at the base of M-Mountain (data from Owens, 2013).

Woods Tunnel geothermal well, drilled into the apex of highest heat flow anomaly (> 400 mW/m^2; Barroll and Reiter, 1990). Concentrations do diminish as solutes disperse while the fluids flow down gradient. This dilution likely occurs within about 10 km of the source region.

Boron is an important component of tourmaline and can be present in biotite, amphibole, and other minerals in metamorphic rocks (Grew, 1996). Upon weathering, boron is sometimes incorporated into other compounds, but more commonly the uncharged ion dominates in water up to a pH of 9.24 (Hem, 1985). The uncharged or anionic boron does not absorb onto mineral surfaces and thus remains in solution. Boron measurements are essential to agricultural assessments because boron is toxic to certain plants (Hem, 1985). As a consequence, boron is commonly measured as part of routine water quality analysis. Lithium is found in spodumene and lepidolite in pegmatites and is found in rock-forming minerals like microcline and albite (Deer et al., 1992). Mica-rich granites, ash flow tuffs, and rhyolitic glass can also be sources of lithium (Witcher, 1988). Like boron, lithium does not absorb onto minerals once released into solution during weathering and it is toxic to certain plants. Both lithium and boron can be concentrated in playa deposits in closed basins. Bromide, a halogen, is an important component in seawater and evaporite minerals. Bromide has a large ionic radius, so it is uncommon in rock forming minerals.

Data compilation. Laura Bexfield of the U.S. Geological Survey office in Albuquerque provided statewide water quality files containing conservative ion (boron, lithium, and bromide), silica and chloride data, groundwater discharge temperature, and water-table elevations. Boron is more commonly analyzed (~ 4000 records; Figure 2-9) than lithium and bromide (~1500 records). In addition, we extracted data from University of New Mexico (Cron, 2011; Williams et al., 2013) and New Mexico Tech theses (Owens, 2013), the National Geothermal Database System (NGDS), the Environmental Protection Agency website, the New Mexico Environment Department, and the New Mexico Bureau of Geology and Mineral Resources Aquifer Mapping database. Boron, lithium, silica and bromide concentrations (mg/l), calculated Cl/Br ratios, and water-table elevations were plotted in ArcGIS. Quality control for the large water quality data set involved removal of data with obvious typos and in some cases an evaluation of the original source of the data, looking for systematic trends in source data sets that might indicate differences in laboratory analysis procedures.

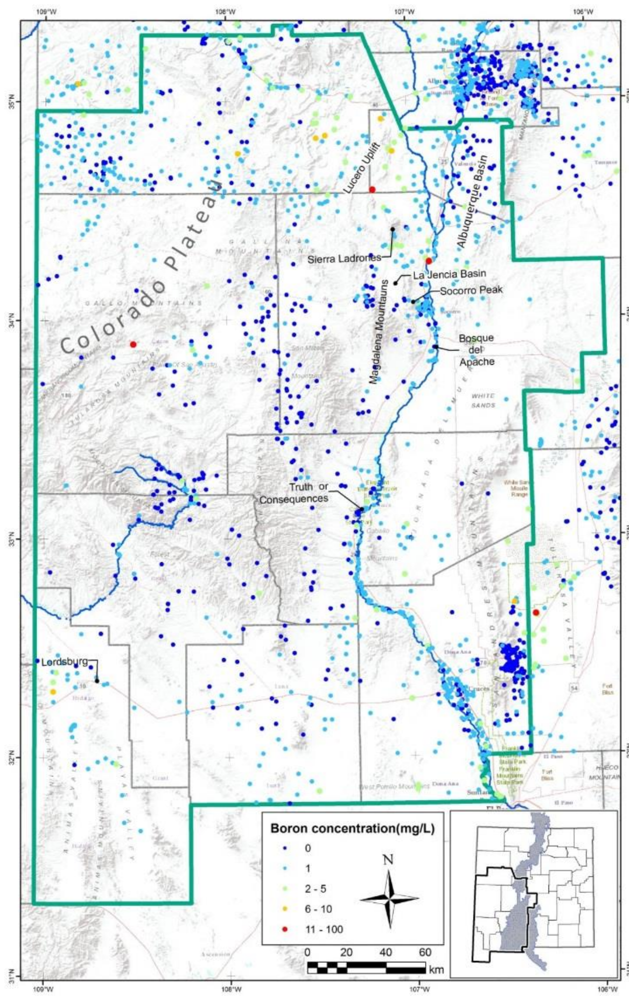

Figure 2-9: Boron concentration map of southwestern New Mexico.

Preliminary Spatial Analysis. Analysis of these maps reveals that known geothermal systems in southwestern New Mexico, like Truth or Consequences and Socorro have elevated concentrations of the conservative ions, as expected. The elevated boron concentrations near Lordsburg in southwestern New Mexico are probably related to evaporation in playas and lakes. All ions are elevated at White Sands National Monument in the Tularosa Basin; this could be related to the presence of the gypsum dunes, the shallow water table, or the high evaporation rates in this area. A couple of new areas of possible geothermal interest that show up on all three conservative ion maps are located near Salado Spring in the Rio Salado at the south end of the Sierra Ladrones in central New Mexico and in a large area in the Acoma Basin and the Lucero Uplift in the transition between the Colorado Plateau and the Rio Grande rift. Water quality data are sparse in some key areas of southwestern New Mexico.

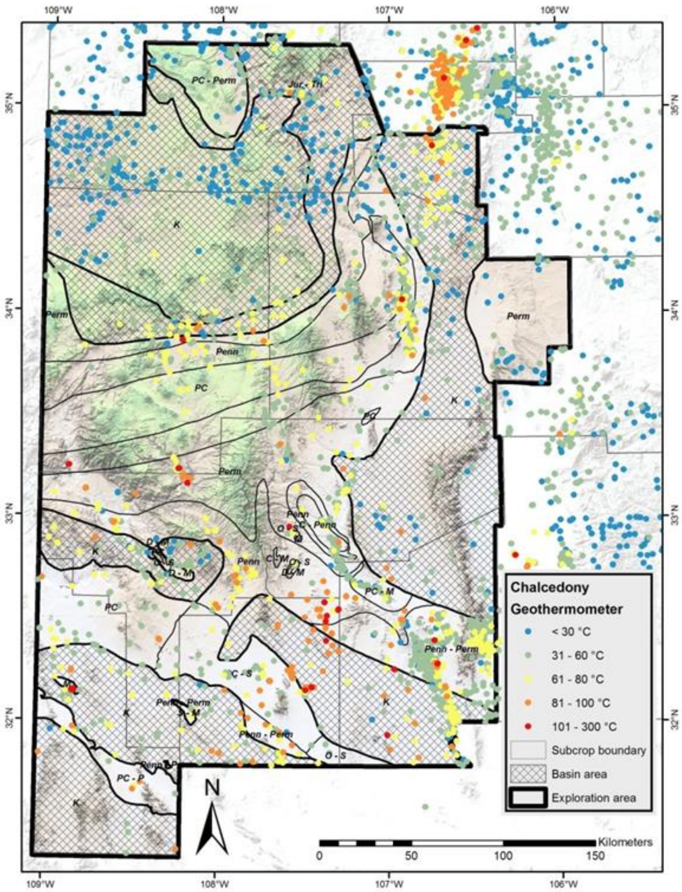

Figure 2-10: Estimated reservoir temperatures based on the chalcedony geothermometer superimposed on the subcrop map. Note that the red dots generally lie on or near the mapped windows.

Silica Geothermometry. In addition, we compiled silica concentration data and calculated estimated reservoir temperatures using the chalcedony geothermometer of Fournier (1977, 1981), updating the work done years ago by Harder et al. (1980) and Morgan et al. (1981). The resulting map suggests higher reservoir temperatures in the southern part of the study area (Figure 2-10). This pattern may, in part, reflect the distribution of silica rich volcanic rocks associated with the Eocene to Oligocene Mogollon-Datil volcanic field. Once again, the Acoma Basin shows up with elevated concentrations of silica. High estimated reservoir temperatures near the Salado Spring may be associated with a blind geothermal system on the margin of the Socorro magma body.

Construction of Water Table Maps. Accurate water-table maps are required for the particle-tracking analysis described below (Figure 2-11).

Water table elevation data was obtained from the New Mexico Office of the State Engineer. Repeat water-table elevations for many of the wells in the database can evaluated in several ways. Here, the earliest measurements for all wells were plotted and contoured; this assumes pre-development water-level conditions (Figure 2-11). In the future, we plan to evaluate measurements collected during the winter, when irrigation rates are low, along with using annual high, annual low, and annual average water-level values (see Phase II description). These different approaches will help quantify the potential uncertainty of groundwater flow directions.

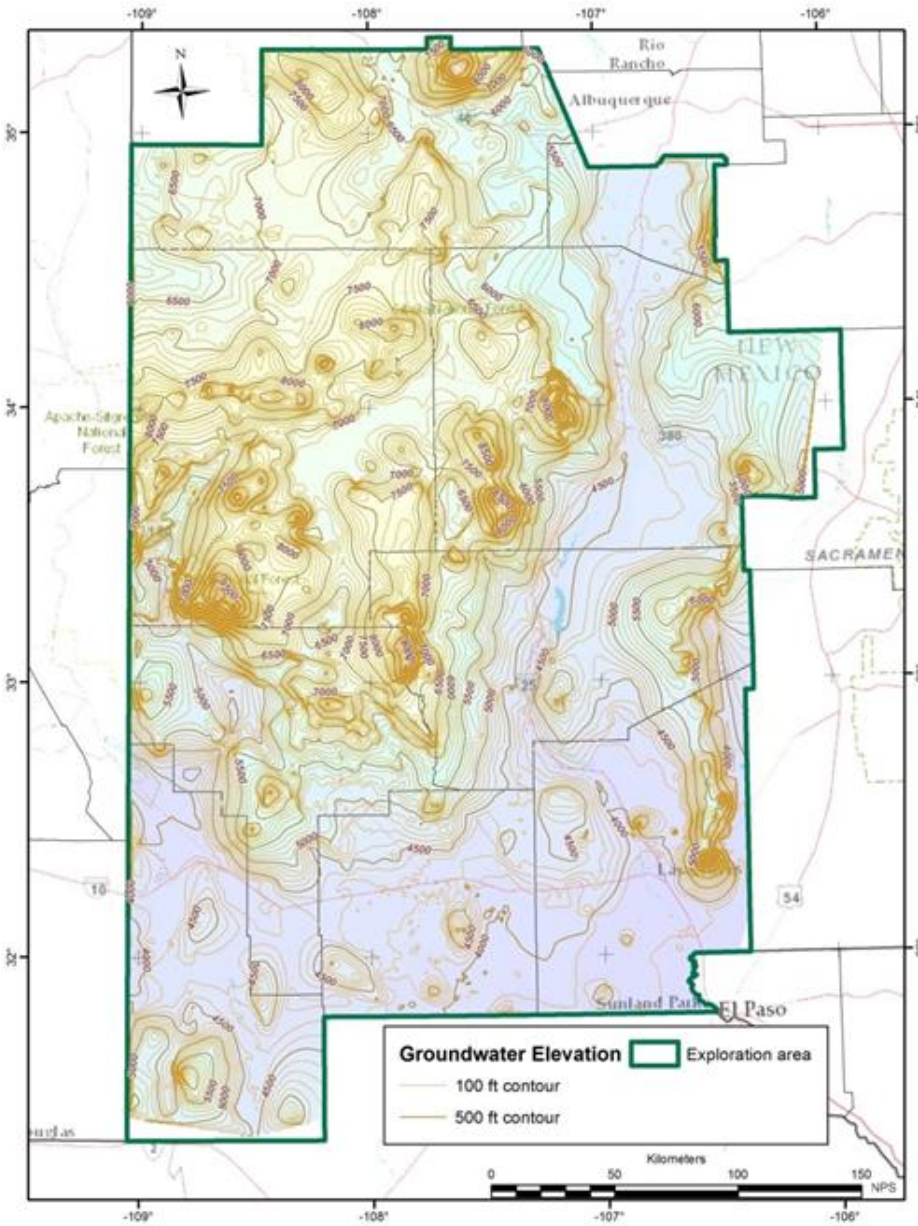

Figure 2-11: Water table elevation map of southwestern New Mexico

2.2.9 Direct Measures of Temperature & Heat Flow

Heat flow/ geothermal gradient map. Heat flow data for the state of New Mexico were compiled as part of the National Geothermal Database System (NGDS) effort. These data largely come from two sources: (1) published data from wells >200 m deep (e.g. Reiter et al., 1975) that measure the regional scale background heat flow, and (2) industry data (AMAX, Hunt, etc.) from wells < 200 m deep that measure heat transfer in more localized hydrogeologic systems. The map in Figure 2-12 includes both shallow and deep heat flow data. A map showing the distribution of groundwater discharge temperatures greater than 30°C from springs and shallow wells was also prepared to serve as another indicator of elevated geothermal gradient.

We compiled and analyzed BHT and formation top data from about 115 oil wells drilled in the area of interest. An ambient surface air temperature lapse rate of T_s (°C) = -7.22e-3*elevation (m) +25.13 was derived from 43 NOAA climate stations in southwestern New Mexico.

The surface temperature and uncorrected BHT values were used to calculate uncorrected geothermal gradients for these wells (Figure 2-13). Although cuttings samples are archived at the NMBGMR for many of these wells, no thermal conductivity data are available, so no heat flow values were calculated. The gradients derived from the southwestern New Mexico oil wells were combined with gradients from the compiled heat flow values to construct a geothermal gradient map for the area of interest.

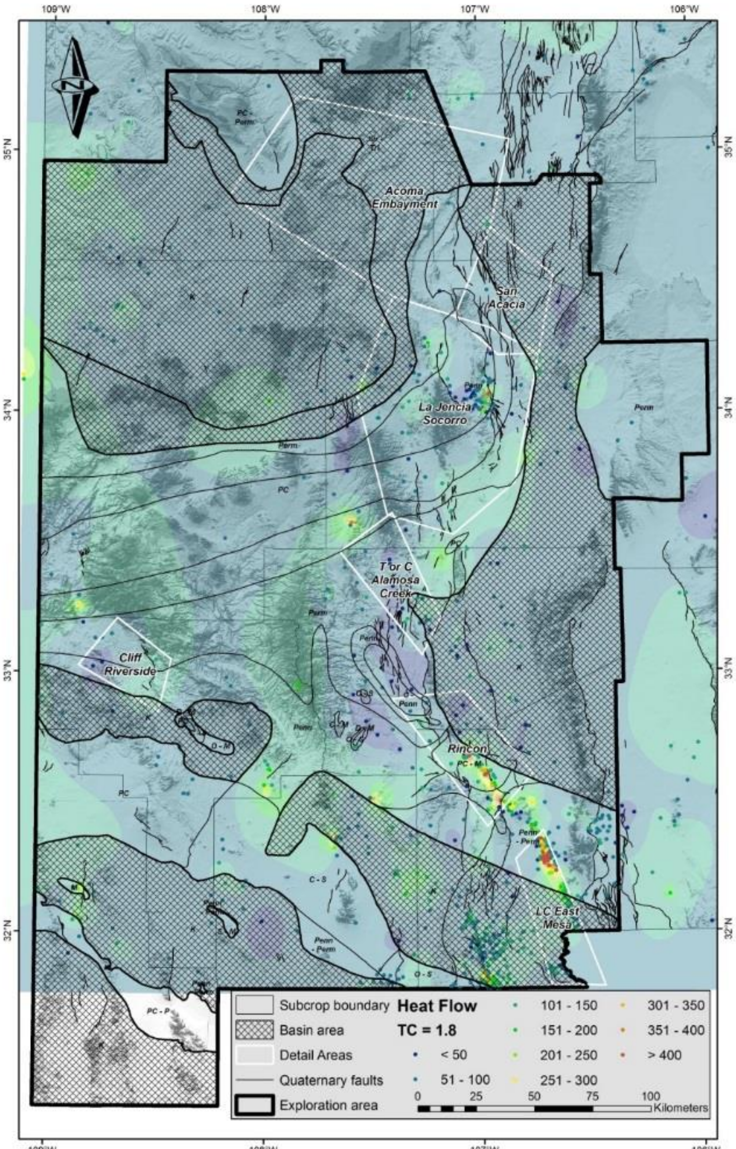

Figure 2-12: Shallow and deep heat flow data superimposed on the subcrop map, Note that all areas of high heat flow are located well within or just on the margin of our mapped windows.

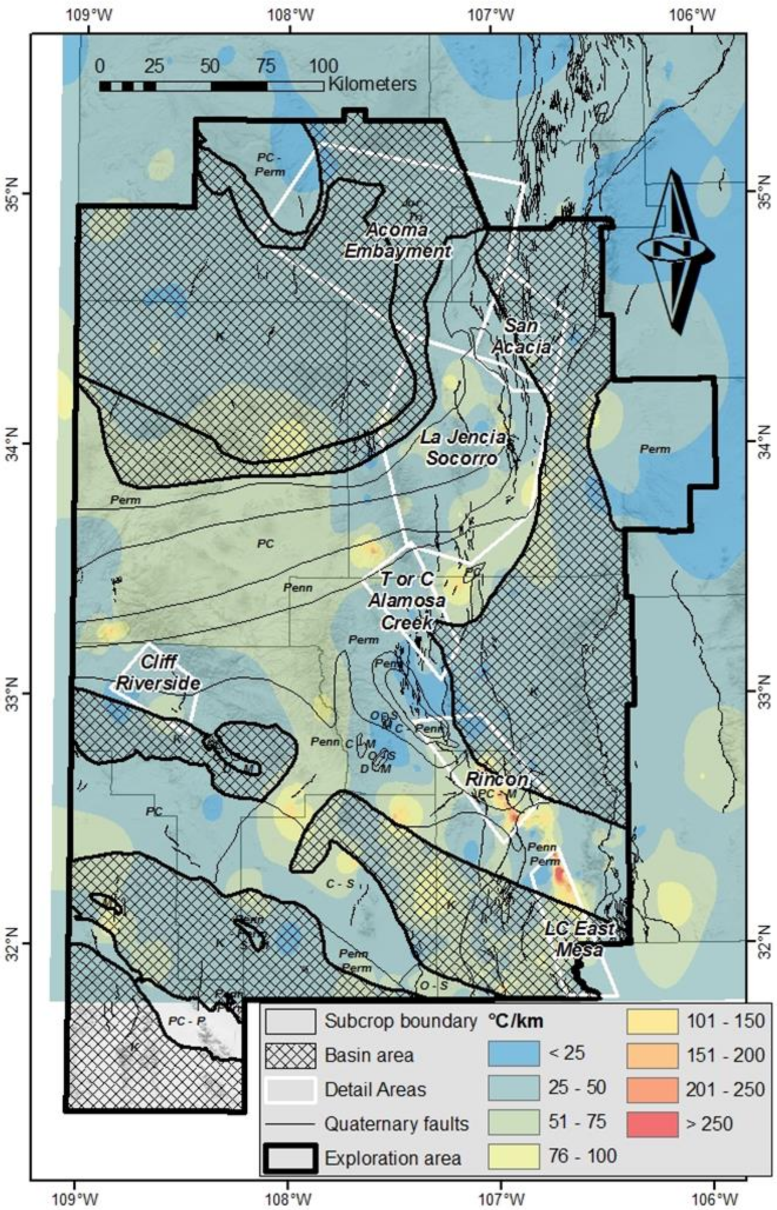

Figure 2-13: Geothermal gradients derived from deep and shallow wells using estimated surface temperatures derived from NOAA data.

Two wells with elevated gradients were identified during the course of this compilation effort. The first is the Twining NAT1 well located in the southeastern Albuquerque Basin near the confluence of the Rio Grande and the Rio Puerco (red star in the northern part of the study area on Figure 2-5). A temperature log measured about 3 months after the completion of the well has a temperature of 190°C (374 °F) at 3.7 km (12,150 ft) and an average geothermal gradient of 45°C/km. The convex-up shape of the temperature profile appears to indicate upflow (Figure 2-14). This well reportedly was completed in rift-fill Santa Fe Group sediments, so the presence or absence of a hydrogeologic window in this instance is difficult to evaluate. Additional detailed geophysical data are needed. A second well is located in the Hachita Valley (red star in the southern part of the study area on Figure 2-5). This well purportedly has 200 °F water at 2,550 feet and bottomed in volcanics. Interestingly, this well seems to be positioned atop a hydrogeologic window composed of Ordovician to Cambrian rocks.

2.2.10 Basement heat generation map.

The gamma ray geophysical well logs from ~ 50 wells penetrating the Proterozoic basement in the area of interest have been scanned and digitized. Only 40 of the logs are of acceptable quality for further analysis. The gamma ray logs are converted to heat production using the equation (Bucker and Rybach, 1996) :

$A[\mu W/m^3] = 0.0158 \text{ (Gamma Ray [API]} - 0.8)$

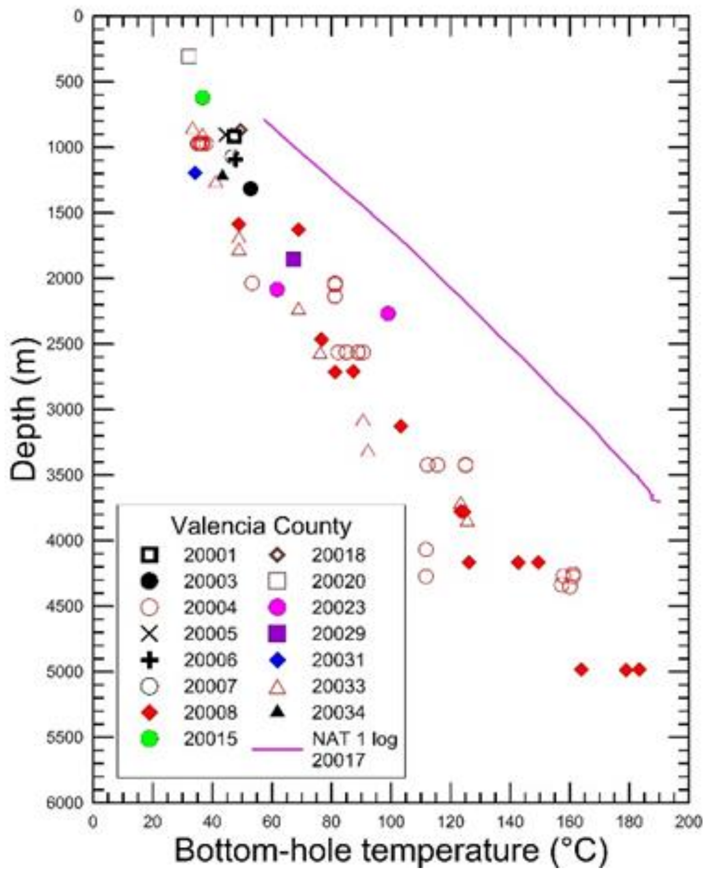

Figure 2-14: Plot of the temperature log measured in Twining NAT 1 compared to measured, uncorrected BHT data from nearby oil wells drilled by Shell and Transocean in the Albuquerque Basin (red symbols) and other wells in the vicinity.

Although numerous subsequent researchers have pointed out that this empirical equation was developed from a small set of data from wells in Europe (e.g. Beardsmore and Cull, 2001) this simple formulation will suffice to ascertain the relative heat production of the basement of New Mexico.

A map summarizing heat generation of Proterozoic basement rocks using gamma ray logs reveals areas of elevated regional scale background heat flow and may point to sites that are well suited to the development of an enhanced geothermal system (EGS) (Figure 2-15). Metamorphic volcanic and sedimentary rocks typically have heat generation values of 0.7 to 1.2 $\mu W/m^3$, and felsic plutonic rocks are generally 1.9 to 2.4 $\mu W/m^3$). Note that most of the basement rocks of New Mexico have typical values of heat generation, but a few scattered areas, including Lightning Dock and the area around T or C have higher-than-normal values.

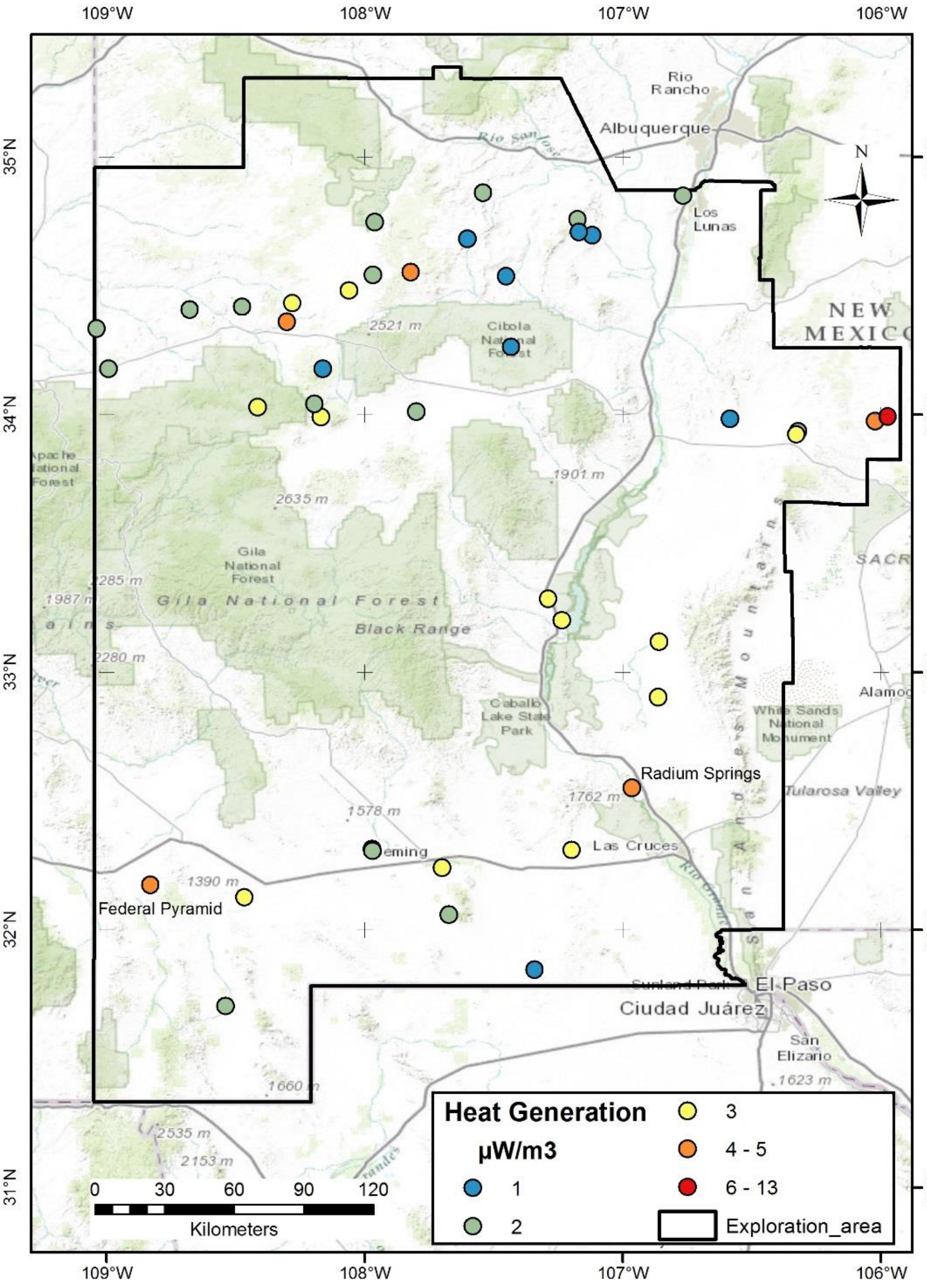

Figure 2-15: Heat generation values calculated from gamma logs completed in Proterozoic basement. High values are associated with two geothermal systems – Radium Springs and Pyramid Federal near Lightning Dock.

2.3 Hydrothermal Modeling

2.3.1 Summary

Three cross-sectional hydrothermal models were developed as part of this project. One is presented below while the two others are described in Appendix C (Section 5). The models produce contour maps of computed groundwater flow directions (stream functions), temperatures, groundwater residence times, and salinity. The models were based on geologic cross-sections developed for this project. The cross-sectional models were used to help test the hydrogeologic windows conceptual model and understand what hydrogeologic conditions favor higher temperature shallow resources across our study area. They were also used to assess what permeability and basal heat flow conditions were needed to match observed thermal gradient measurements. During Phase II, these models can be compared to new and existing temperature logs and ^{14}C groundwater residence time information. There was insufficient time to calibrate all three of these models to available thermal and geochemical data during Phase I. However, these preliminary models did provide insights into how hydrogeologic window geometry controls shallow thermal resource quality. In general, we found that hydrothermal model windows that were relatively wide (> 300m) , which were associated with crystalline basement subcrop features (e.g. Acoma, see appendix; Truth or Consequences, Pepin et al., 2015; Socorro, Mallioux et al., 1999), tended to form lower temperature (~ 40 ^{o}C) thermal anomalies at shallow depths (< 100m depth). Narrower hydrogeologic windows associated with fault zones (e.g. Rincon) formed higher temperature resources (~ 70 ^{o}C, < 200m depth), since regional hydrothermal discharge was focused into a relatively narrow conduit. The hydrothermal model at San Acacia (see appendix) that overlies the Socorro magma body produced thermal convection cells and small amounts of shallow groundwater discharge. These “closed” convection cells had much older groundwater ages that were on the order of hundreds of thousands of years (^{14}C dead). No distinct outflow zone formed within the San Acacia model. An in-progress magnetotelluric (MT) survey across the San Acacia study area will help to provide additional ground truth for this model. For the Acoma cross sectional model, a solute outflow plume was produced adjacent to the crystalline basement hydrogeologic window at Acoma. The calculated discharge temperature within the crystalline basement hydrogeologic window was 40^{o}C and groundwater residence time was 78,000 years (^{14}C dead).

2.3.2 Cross-Sectional Hydrothermal/Groundwater Residence Time Models

Hydrothermal models have proven to be of great benefit in understanding the plumbing of geothermal systems (e.g. Smith and Chapman, 1983; Forster and Smith, 1989). The hydrogeologic windows conceptual model, on which much of this project is based, typically assumes that there is a deep hydrothermal flow system within the crystalline basement. This deep hydrothermal flow system has been inferred from prior cross sectional model studies by Mailloux et al. (1999) and Pepin et al. (2015). We constructed three cross-sectional models to explore how regional groundwater flow systems could modify temperature patterns and groundwater residence time within the crystalline basement at Rincon, Acoma, and San Acacia sub regions (Figure 2-16). The geologic cross sections on which the hydrothermal models are based were utilized existing geologic data from prior studies (e.g. Kelley, 1957) or were constructed as part of this project. All of the models include a thick zone of Precambrian basement overlain by Paleozoic to Quaternary sediments. The geologic cross sections used to create our hydrothermal models were constructed perpendicular to the regional groundwater table. The cross sections extend to adjacent high elevation mountain ranges. The San Acacia and Acoma cross sections include hydrogeologic windows where crystalline basement crops out at the land surface. Along the Rincon section, a re-activated Laramide reverse

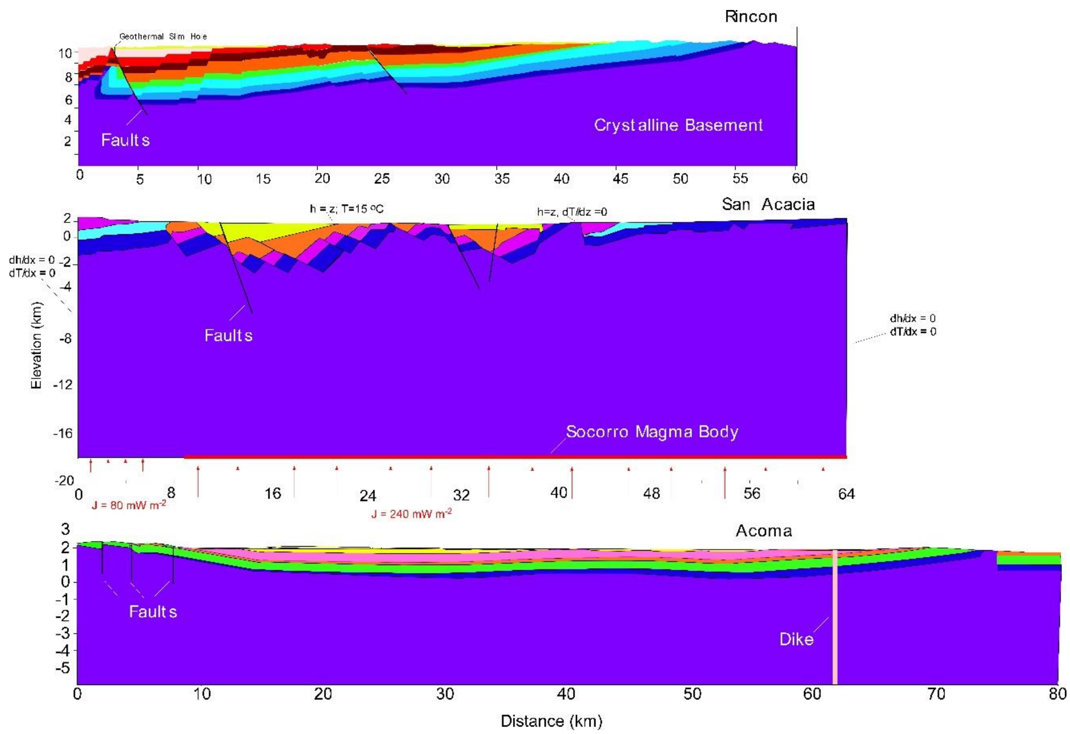

Figure 2-16: Rincon, San Acacia, and Acoma cross-sectional models. Acoma cross-sectional data after Kelley (1957) and Baldwin and Anderholm, 1992. See Figure 2-13 for locations of these areas.

fault appears to be acting as the hydrogeologic window. The fault is situated in a highly deformed anticlinal complex where the crystalline basement is close to the land surface. The maximum depth of these cross sections ranges from 8 to 19 km. The 19 km deep cross section at San Acacia was extended below the brittle ductile transition in order to include the effects of the Socorro Magma body that is present at 19 km depth. Recent InSar analysis suggests that the magma body is inflating (Fialko and Simmons, 2001; Pearse and Fialko, 2010). The lateral extent of the cross sections ranges from 60 to 80 km. This yields an aspect ratio between about 1:3 to 1:10. The aspect ratio of a forced convection geothermal system has important controls on hot spring temperatures (low ratios are favored, Ferguson and Grasby, 2011). Long-distance lateral flow is not conducive to forming a geothermal anomaly.

To date, not all of the cross-sectional models have been calibrated to available temperature, geochemical and residence time data. The Rincon cross section had several thermal gradient wells that were used to calibrate this model. Pepin et al. (2015) used cross sectional hydrothermal models, like the ones constructed here, to reproduce observed temperatures, vertical flow velocities and groundwater residence times within the Truth or Consequences hot-springs district. Their analysis indicated that effective basement permeability is about 10^{-12} m^2 (1000 mD) to depths of 2-8 km near T or C. This required running more than 40 simulations over a two-year period. We anticipate being able to conduct a similar analysis of hydrothermal conditions in our study areas during Phase II of this project. We also intend to collect groundwater chemistry data (including ^{14}C age dates) to calibrate all of our hydrogeologic models during Phase II. The results of the Rincon model are described below. The Acoma and San Acacia sections are discussed in more detail in Appendix C (Section 5).

These hydrothermal models calculate groundwater flow (stream functions), heat transfer, and groundwater residence times. The governing equations solved by the model *FEMOC* are presented in Pepin et al. (2015) and will not be repeated here. The algorithms implemented in this code were originally validated, in part, by reproducing published cross-sectional conductive/convective temperatures presented by Smith and Chapman (1983) and residence times by Goode (1997).

2.3.3 Initial Conditions

We assigned water-table temperatures across the top of our domain of 15 °C. Initial subsurface temperatures were assumed to increase linearly with depth using a 40 °C/km temperature gradient that is representative of the region (Reiter et al. 1986). All model simulations were run to steady-state conditions (1 million years) in order to reduce the influence of initial conditions.

2.3.4 Mesh Configuration

The number of nodes and number of elements within the cross-sectional finite-element grids are listed in Table 2-1. The lateral dimensions of the grid varied from approximately 2000 m away from the windows, down to 50 m within the hydrogeologic windows. Except for very thin hydrostratigraphic units that are 10 to 20 m in thickness, there are regionally 2 to 3 nodes per stratigraphic layer in the vertical direction. Shallow vertical dimensions average 10 to 100 m.

2.3.5 Hydrostratigraphy and Simulation Parameters

We used up to nine hydrostratigraphic units in these models to represent Paleozoic to Quaternary aquifers and confining units in these cross-sections. For Rincon, the hydrogeologic window is associated with a 100 m wide permeable fault zone. In the other models, the hydrogeologic window is associated with crystalline basement cropping out at the surface. The hydrogeologic parameters assigned to each stratigraphic unit are presented in Table 2-1.

Table 2-1: Description of Grids and Permeability used in models

Model Name	Number Nodes	Number Elements	Crys. Perm. (mD)	Fault Perm. (mD)	Sed. Aq. Perm. (mD)	Conf. Unit Perm. (mD)	Number Units
Rincon	1595	3007	800	2000	100	0.001	10
Acoma	1946	3172	100	Na	100	0.001	9
San Acacia	1744	3301	100	Na	100	0.001	9

Crys. – Crystalline Basemen;, Sed. –Sedimentary; Conf.- Confining; Perm. - Permeability

Insufficient well-test data exists to assign locally-derived hydrogeologic parameters to the stratigraphic layers in the model. Therefore, we used representative permeability and porosity values consistent with Freeze and Cherry (1979) for different lithologies. Thermal transport and petrophysical parameters that were assigned to all stratigraphic units and held constant are presented in Table 2-2.

Table 2-2: Thermal and solute transport and physical parameters used in FEMOC cross-sectional hydrothermal model assigned to all hydrostratigraphic units. These parameters were held constant for all simulations.

Symbol	Variable Name	Magnitude
α_L	Longitudinal Dispersivity	100 m
α_T	Transverse Dispersivity	10 m
λ_f	Fluid Thermal Conductivity	0.58 W m^{-1} $^oC^{-1}$
λ_r	Solid Thermal Conductivity	2.5 W m^{-1} $^oC^{-1}$
ρ_s	Rock Density	2600 kg m^{-3}
S_s	Specific Storage	10^{-7} m^{-1}

2.3.6 Numerical Implementation

We solved the aforementioned equations sequentially using the finite-element method. The stream-function based groundwater flow equation was solved using Galerkin's finite-element method using triangular elements and linear trial solutions. The heat-transport equation was solved using the modified method of characteristics (MMOC). Each transport equation was solved on a separate processor using a parallelization algorithm. The models were run for 1,000,000 years using a time step size of 100 years in order to reach steady-state conditions.

2.3.7 Boundary Conditions

Boundary conditions often have great potential to impact modeling results. The boundary conditions we assigned in our model are those that we felt were most consistent with field-evidenced flow conditions. *FEMOC* uses this head gradient to determine a surface flux using the following steady-state stream function equation:

$$\frac{\partial\psi}{\partial z} = -K\frac{\partial h}{\partial x} \qquad (1)$$

where K is the hydraulic conductivity [L^1t^{-1}], h is hydraulic head [L^1], and ψ is the stream function [L^2t^{-1}]. Assigned water-table elevations based on water table maps from the office of the State Engineer. The no-flux boundary condition is imposed on the sides and base of the cross-sections.

For heat transport, a specified temperature boundary condition was assigned across the top of our domain at the water table (Figure 2-16). For the hydrogeologic window, a no-flux boundary condition was imposed allowing the temperatures within the discharge zone to be controlled by the flow system. Along the base of the solution domain, we assigned a basal heat flux typical of the Rio Grande rift of 0.09 W/m^2, which closely resembles measured heat flux values near Truth or Consequences (Sass et al. 1971; Sanford et al. 1979; Reiter et al. 1986). For the San Acacia model in the vicinity of the Socorro Magma body, specified heat flow was set at 0.24 W/m^2. For the Rincon model, we specified a basal heat flux of 0.18 W/m^2. No-flux boundaries were imposed on the sides of the domain.

About two-dozen simulations were run to complete the trial and error calibration process. In this section, we present preliminary model results from the Rincon model cross sectional model below. As mentioned previously, results for the Acoma and San Acacia models are presented in Appendix B (Section 5). We also constructed a three-dimensional model of the Socorro-La Jencia Basin in order to understand why the heat flow anomaly at the base of M-Mountain terminates abruptly. This modeling effort is ongoing and is not presented in the final report.

2.3.8 Rincon Model Results

For the Rincon cross section, the Precambrian basement is exposed on the east side of the San Andreas Mountains (recharge area) about 60 km to the west of the Rincon prospect (Figure 2-17A). Groundwater recharges the Precambrian basement at a rate of about 0.1 m/yr (Darcy flux, q_z). The fault zone permeability was set to $8x10^{-12}$ m^2 (8,000 mD). The crystalline basement permeability was set to 10^{-12} m^2 (1,000 mD). Groundwater circulates to a depth of about 6-7 km, flowing laterally to the west and picking up heat (Figure 2-17). Discharge occurs along a sub-vertical fault zone that is part of a Laramide reverse fault and associated overturned fold system (Figure 2-16). Vertical fluid velocities within the fault zone are about 40 m/yr (q_z). Simulated groundwater age at the base of the fault zone is about 17,000 years (Figure 2-17C). Significant convective heat transport occurs within the fault zone (Figure 2-17B) and simulated temperature profiles within the groundwater discharge area nearly match observed values in shallow gradient wells (Figure 2-18).

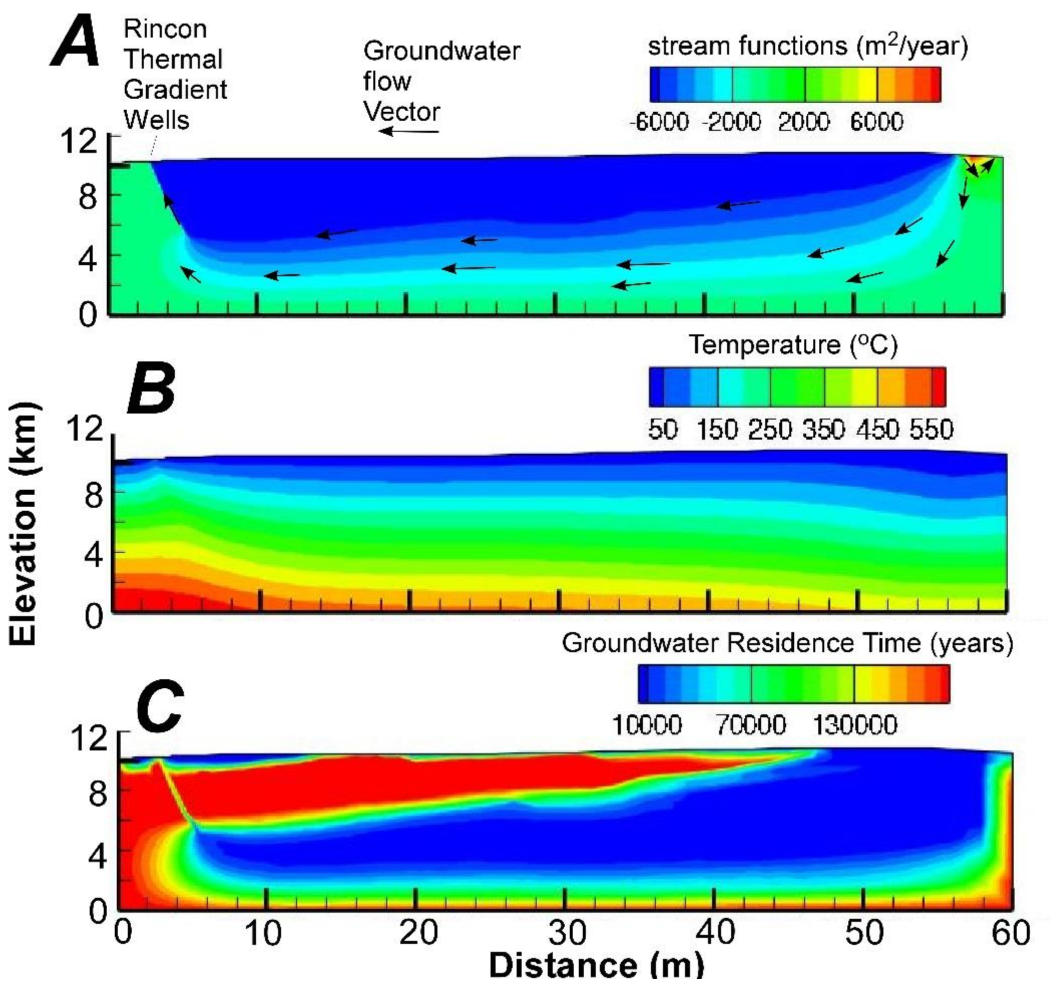

Figure 2-17: Cross-sectional model of Rincon geothermal system. (A) computed stream functions (in m^2/yr), (B) temperature (°C), and (C) groundwater residence times.

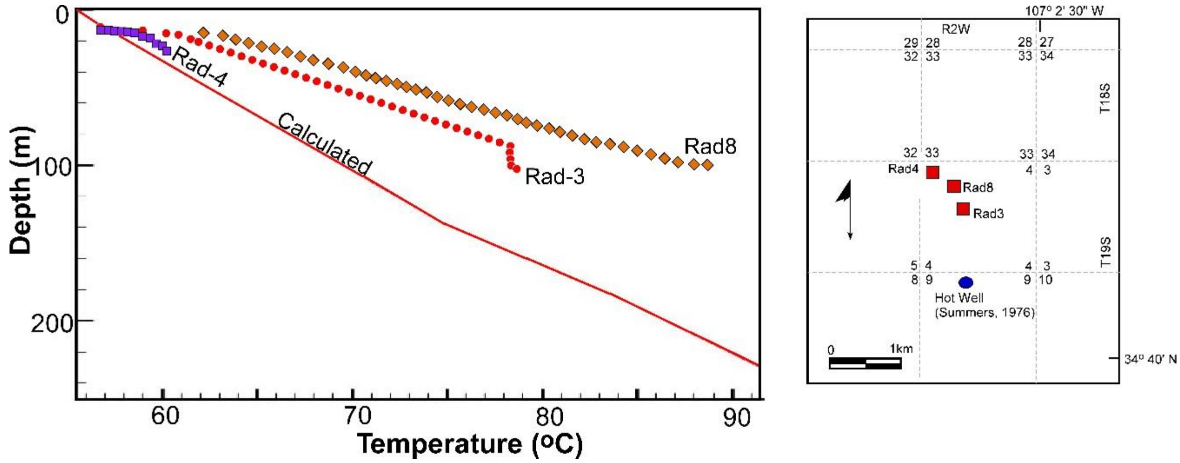

Figure 2-18: Comparison of computed (red line) and observed (symbols) for Rincon geothermal system. The approximate location of the Rincon test wells is shown in Figure 2-17 (after Witcher, 1991).

2.4 Geochemical Tracer Analysis Summary

Geochemical geothermometers are typically used to estimate reservoir temperatures at depth but analysis of their spatial distribution is rare. We hypothesize that these trace elements are retained at high concentrations as they discharge through hydrogeologic windows into the shallow aquifer system (Figure 2-19). As geochemical tracers such as boron and lithium are transported down hydrogeologic gradient, they will eventually disperse reaching concentrations below the limit of detection, probably within about 10 km of the upflow zone. The idea of using principles of advective transport to locate geologic targets is not a new idea. A similar approach was used in the ore deposits industry to locate diamond-rich kimberlite pipes within glaciated regions of the Canadian Shield (McClenaghan and Kjarsgaard, 2001). These authors used dispersal patterns of pyrope, a high pressure/temperature garnet associated with kimberlites, to locate kimberlite pipes overlain by in glacial tills and lacustrine sediments. In this case, the transport agent was ice rather than groundwater. As part of this project, we have tried to determine whether geochemical tracer data from existing wells are of sufficiently high spatial density to locate hydrogeologic windows within our study area using basic principles of advective-diffusive solute transport. There are several assumptions that go into this analysis. First, we assume that high boron concentrations are associated with high temperature fluids. We assume that shallow water table wells access this plume and that the plume moves down hydrogeologic gradient. The distribution and density of wells needs to be sufficiently large so that a plume can be detected and the upflow zone delineated. Particle-tracking analysis applied to dissolved boron concentrations in available wells was used to assess the locations of potential upflow zones within seven regions within our study area (Figure 2-13). As noted in Section 2.2.8, boron concentrations are correlated with geothermal fluids. We found that in some areas, wells with relatively high concentrations were located within hydrogeologic windows, regions of high heat flow, and in some situations, fault zones. Using existing well geochemical data, we identified two prospective regions within the Acoma Basin/Lucero uplift along the Comanche fault zone and in the Riverside-Cliff area along the Gila River. The two prospects both occur within hydrogeologic windows where Cretaceous confining units have been eroded away. Forward models of advective-dispersive transport were developed for the Acoma study area using PFLOTRAN. In our PFLOTRAN analysis, a total of 625 potential source locations with variable source concentrations were simulated. The computed boron concentrations resulting from solving a

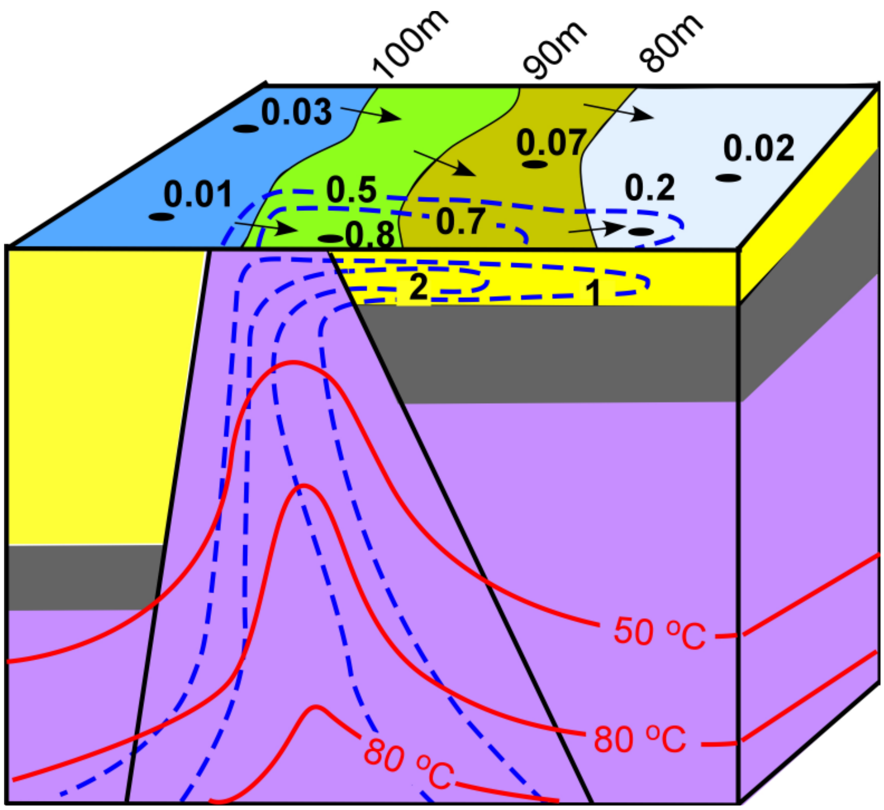

Figure 2-19: Schematic block diagram depicting advective-dispersive transport of geochemical tracer (blue dashed contour lines, e.g. boron, lithium), heat (red contour lines) into a shallow alluvial aquifer. The geochemical tracers are advected down hydrogeologic gradient. We propose that the tracers that are detected in down gradient wells may provide evidence of the up gradient hydrogeologic window.

steady-state advection-dispersion equation were compared to observed well geochemical data using the root mean squared error (RMSE; square root of the sum of the computed minus observed concentrations squared). Results suggest that the actual source location is to the west of the Comanche fault, as expected. The lack of distributed well chemistry data limited our ability to identify the exact location of the geothermal upflow zones in both regions. However, there many wells within two study areas that could be sampled during Phase II that could help to refine the locations of the geothermal upflow zone. Below we present the Gila and Acoma particle-tracking results. These highlight the utility of the approach but also some important short comings due to either low well density or poorly spaced wells. Discussion of the other five particle-tracking analysis for Socorro, San Acacia, Las Cruces East Mesa, and Rincon is presented in Appendix C (Section 6).

2.4.1 Methods

2.4.1.1 Data compilation

As discussed in Section 2.5.3.1 later in the report, Li>1.32 and B>0.84 mg/l are generally associated with known geothermal systems in New Mexico. Most of the lithium, boron and bromide concentrations in geothermal waters in southwestern New Mexico vary between 0.5 and 4 mg/l, although they are as low as 0.01 in some regions (Grant County).

We analyzed all lithium and boron data to see how boron-lithium concentrations correlated with hot spring/geothermal well temperatures (Figure 2-20 compares lithium and boron concentrations against the temperature of wells (produced fluid temperature) or hot springs discharge temperature for all samples available. The highest temperature samples are from geothermal wells within the Valles Caldera. There is a general correlation between produced fluid temperatures and tracer concentrations (Figure 2-20). There is significant variability of boron and lithium concentrations for any given hot spring/geothermal well temperature. This could be due to conductive cooling of samples obtained at hot springs, variable mineralogy within different geothermal reservoirs, evapoconcentration within playa environments, and/or mixing with shallow aquifer fluids. Geothermal fluids within NM are Na-Cl dominated. Because boron concentrations data is about 4 times more abundant than the other two tracers, we used boron in the analysis presented below.

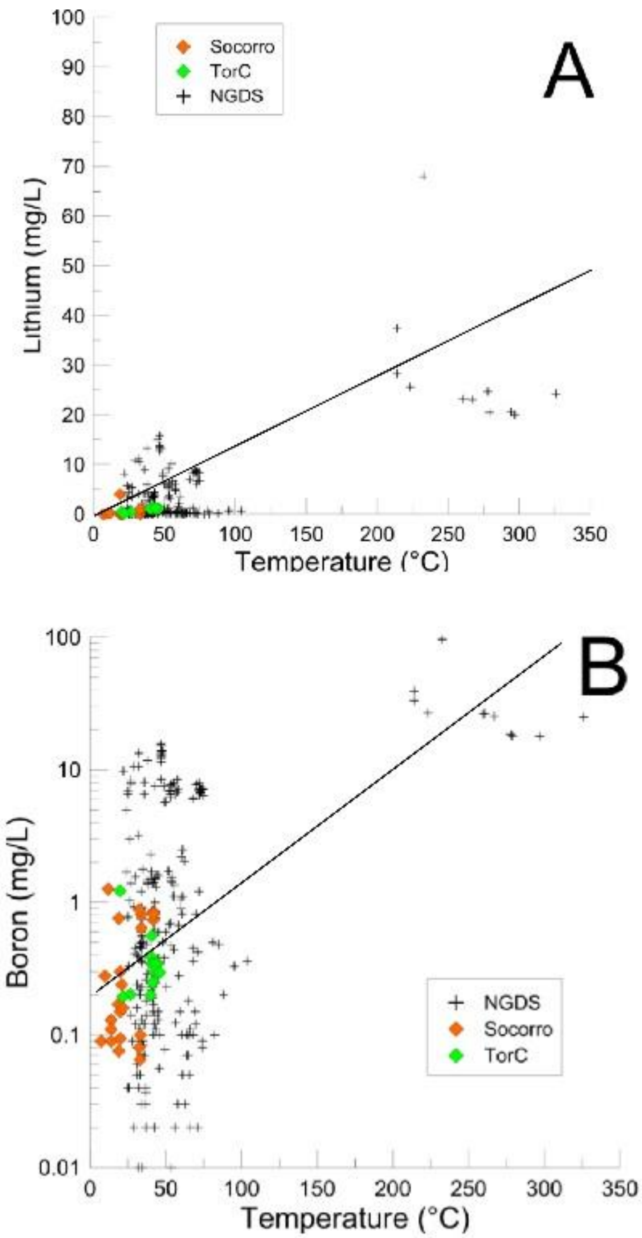

Figure 2-20: Correlation between (A) lithium and (B) boron concentration and spring/produced water temperature from geothermal wells across New Mexico.

2.4.1.2 Particle-tracking

Typically, geochemical geothermometers are used to estimate reservoir temperatures (zero-dimensional analysis). Our first approach was to determine whether or not principles of advective-solute transport can locate hydrogeologic windows and associated upflow plumes. Figure 2-21 schematically illustrates how our procedure works. We assume that a solute plume exists for some distance down gradient from a hydrogeologic window (Figure 2-21a) and that this plume is oriented down hydrogeologic gradient. Particles are introduced and assigned a color based on the concentration of the tracer (red high, blue low concentration; Figure 2-21b). The particles are moved up gradient through the flow field until they contact the hydrogeologic divide using the average linear velocity. Regions in between wells having high tracer concentrations and low (background) concentration wells along the flow path can be used to identify the upflow zone (gray area in Figure 2-21c).

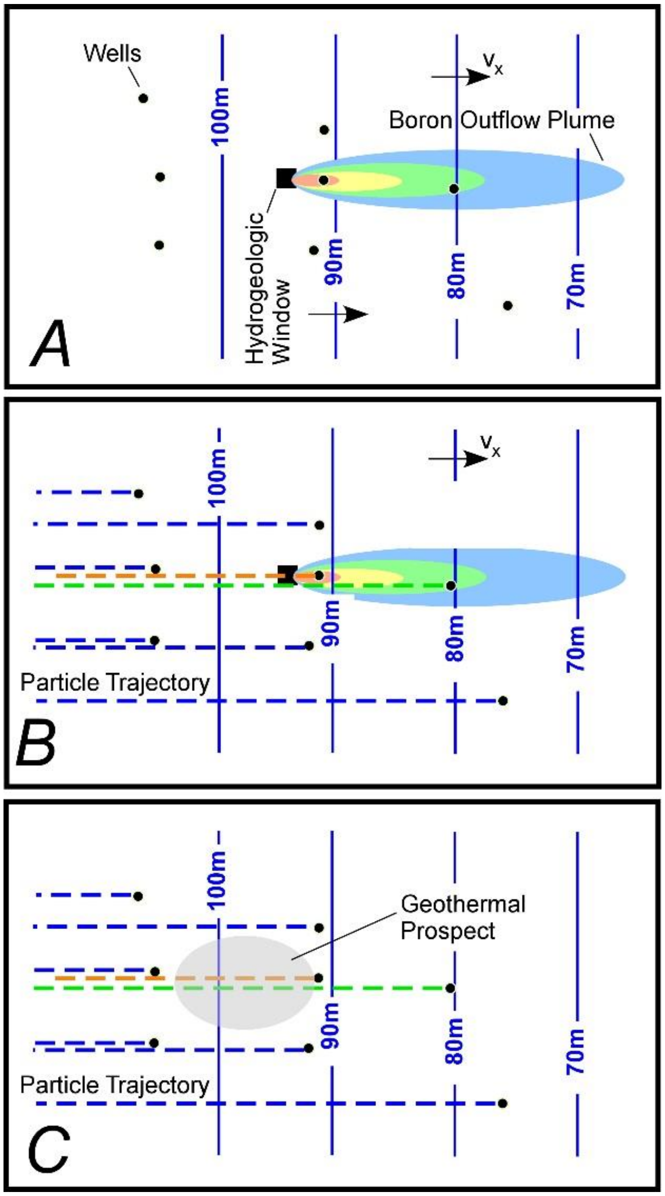

Figure 2-21: (A) Conceptual model depicting outflow plume of boron from a hydrogeologic window. (B) Representation of upwinded particle trajectories (dashed lines). (C) Proposed location of hydrogeologic window based on particle concentrations and trajectories.

The average linear groundwater velocities are computed using the local water table gradient:

$$v_x = -\frac{K}{\phi}\frac{\Delta h}{\Delta x} \qquad v_y = -\frac{K}{\phi}\frac{\Delta h}{\Delta y} \qquad (1)$$

where K is hydraulic conductivity of the water-table aquifer, f is porosity, h is hydraulic head, and v_x and v_y are the components of the groundwater velocities in the *x*- and *y*-directions. In our analysis, we assumed a hydraulic conductivity value of 1 m/yr and a porosity of 0.1. The groundwater flow field is orthogonal to the water table contours. The average linear velocities were used to track geochemical tracers up gradient through the flow field (Pollock, 1994). We placed a mathematical particle at each well location that had a boron or lithium analyses and tracked the particle up gradient from the wells through the shallow aquifer as follows:

$$x_p^{k+1} = x_p^k - \Delta t v_x \qquad\qquad y_p^{k+1} = y_p^k - \Delta t v_y \qquad\qquad (2)$$

where x_p^{k+1}, x_p^k are the particle locations in the x-direction at the old (k) and new (k+1) time levels, and y_p^{k+1}, y_p^k are the particle locations in the y-direction at the old (k) and new (k+1) time levels. We hypothesize that a hydrogeologic window within a blind geothermal system should be some distance up hydrogeologic gradient of a highest concentration well and down gradient of a low concentration well along the ground-water flow path.

We introduce mathematical particles into a triangulated grid at the well locations. The water table elevations at existing well locations and along perennial streams were assigned to each node in the triangulated mesh. The velocity was calculated at each triangle using equations (1-2). Each particle is assigned its respective lithium or boron concentrations. We then use the flow vectors to move the particles upwind across the basin. In areas with sufficient well density, we can identify prospective geothermal up flow zones (gray pattern, Figure 2-21c).

2.4.1.3 Source Identification using Advection-Dispersion Equation in PFLOTRAN

The above approach does not consider solute diffusion or dispersion. We also developed forward models of advective-dispersive transport of boron and lithium varying the upflow zone (hydrogeologic window) location. In this approach we perform source zone identification using inverse analysis coupled to the advection-dispersion equation in PFLOTRAN (Lichtner et al., 2015). PFLOTRAN is a parallel subsurface flow and reactive transport simulator. The groundwater flow field is derived from measurements of water table heights based on a steady-state solution of the groundwater flow equation in PFLOTRAN. Then a steady-state advection-dispersion equation is solved using fluxes from the flow field to simulate tracer transport from an upflow zone (source location). For the steady-state models, we solved the following two-dimensional advection-dispersion equation to simulate lithium/boron transport:

$$\frac{\partial}{\partial x}\left[D_{xx}\frac{\partial c}{\partial x}+D_{xy}\frac{\partial c}{\partial y}\right]+\frac{\partial}{\partial y}\left[D_{xy}\frac{\partial c}{\partial x}+D_{yy}\frac{\partial c}{\partial y}\right]=v_x\frac{\partial c}{\partial x}+v_y\frac{\partial c}{\partial y} \qquad (3)$$

where D_{xx}, D_{xy}, D_{yx}, and D_{yy} are the components of the hydrodynamic dispersion-diffusion tensor, v_x and v_y are the components of groundwater velocity in the x- and y-directions, and c is trace element concentration.

Source location sampling and calibration are performed using the Python-based Model Analysis ToolKit (MATK; http://matk.lanl.gov) developed at Los Alamos National Laboratory. MATK allows for simultaneously running multiple realizations in parallel and provides tools for post processing the data and calibration. Visualization of the results is performed by the software package Robust Analysis of Risk for Exploration and Development of Geothermal Energy (RAREGE; LA-CC-14-105) also developed at Los Alamos National Laboratory. RAREDGE handles disparities between various model meshes, interpolation of data, and exporting of visualization files. We coupled MATK with PyFLOTRAN (Karra and Kitay 2015), which is a Python-based toolkit that facilitates execution of PFLOTRAN.

2.4.1.4 Model Analysis

The Model Analysis ToolKit (MATK; http://matk.lanl.gov) developed at Los Alamos National Laboratory was used to analyze source identification PFLOTRAN simulations. MATK provides functionality to calibrate and perform uncertainty and sensitivity analyses on external model. MATK handles concurrent model simulations on multi-processor architectures and high performance clusters to distribute the computational burden of model analysis. In Phase I, MATK performed source location sampling and calibration. We coupled MATK with PyFLOTRAN (Karra and Kitay 2015), which is a Python-based toolkit that facilitates execution of PFLOTRAN.

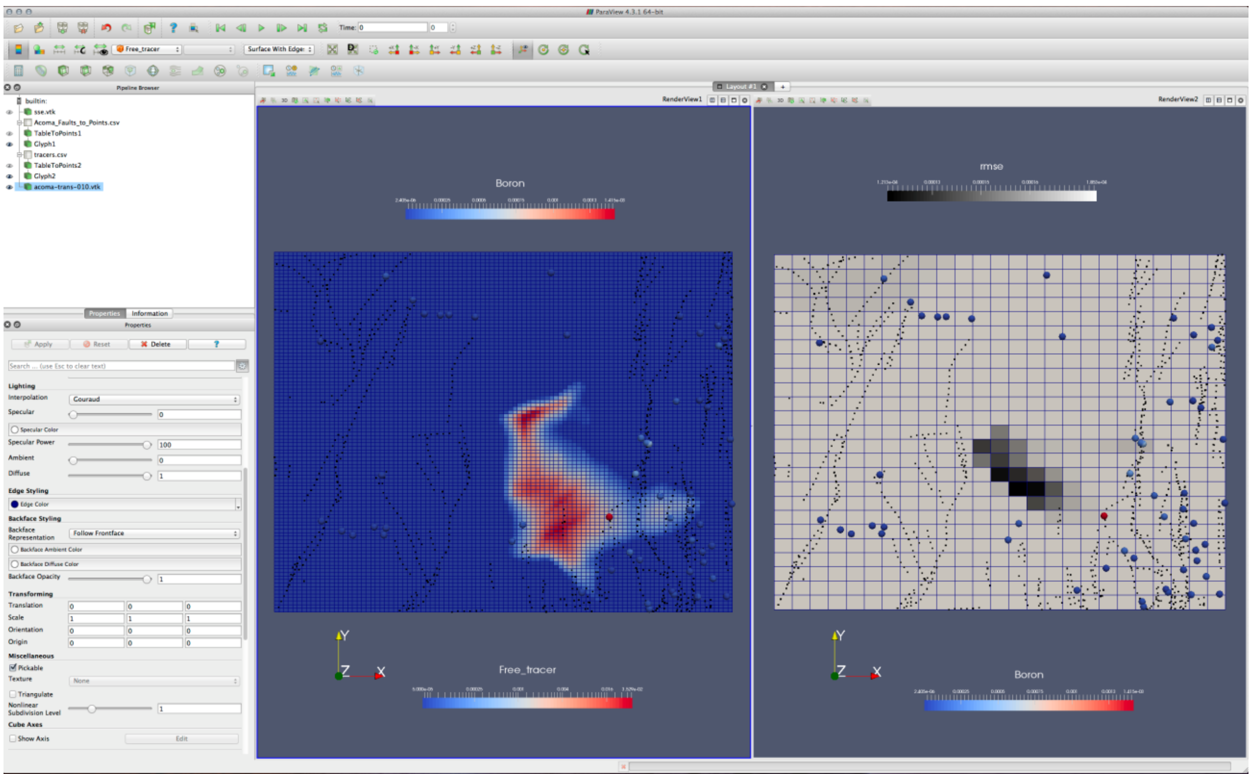

Figure 2-22: Screenshot of RAREDGE geothermal model analysis for the acoma site displayed using the ParaView open source visualization package. The left pane presents the PFLOTRAN simulated concentrations for the best fit source location. The right pane presents a gray scale colormap of the rmse values for source locations. Colored spheres in both panes are measured boron concentrations and dashed black lines are fault locations.

Visualization of the results is performed by the software package Robust Analysis of Risk for Exploration and Development of Geothermal Energy (RAREGE; LA-CC-14-105) also developed at Los Alamos National Laboratory. RAREDGE handles disparities between various model meshes, interpolation of data, and exporting of visualization files in the open source Visualization ToolKit (VTK) format. Open source visualization packages, such as ParaView and VisIt can be used to visualize and interrogate the model analysis results. Figure 2-22 provides a screenshot of a RAREDGE geothermal analysis that is automatically opened upon completion of the model analysis. RAREDGE coupled with MATK provides a comprehensive model analysis/visualization framework.

2.4.2 Results

2.4.2.1 Sub Region Overview

We developed particle trajectory maps for seven locations including San Acacia region, southern San Acacia, Acoma Basin region, Truth or Consequences region, Socorro-La Jencia Basin, Gila River region near Cliff, NM, Las Cruces-East Mesa along the Rio Grande, and Rincon region along the Rio Grande include the Radium Springs area (see Figure 2-7 above). The well density across these areas varied between about 1 wells/100 km^2 (Gila) to 10 wells/km^2 (Las Cruces-East Mesa; Table 2-3). In the final report, we present results for the Socorro (known geothermal resource) as well as the Gila and Acoma regions (two prospective resource areas). The remainder of the particle-tracking results are presented in Appendix C (Section 6).

Table 2-3: Well Density of sub regions used in Particle-tracking Analysis

Location	Boron Well Density (wells/100 km^2)	Lithium Well Density (wells/100 km^2)
Las Cruces East Mesa	10.4	1.2
Rincon	4.7	1.6
Acoma	0.7	0.3
Gila	3.2	0.7
Socorro	3.8	3.4
San Acacia	7.9	4.1
Truth or Consequences	2.8	1.3

2.4.2.2 Socorro-La Jencia Basin

The Socorro – La Jencia Basin geothermal system is a known low-temperature geothermal resource area (Chapin et al., 1978). Geothermal fluids discharge across a hydrogeologic window at the base of Socorro Peak. Here fault block rotation has dissected Tertiary confining units, permitting crystalline basement to crop out (Barroll and Reiter, 1991). Because the location of the geothermal upflow zone is well known here, the particle-tracking analysis serves as a test of our approach. Within the upflow zone, boron and lithium concentrations are high (> 1 mg/l; Owens, 2013) in wells associated with high heat flow (> 200 mW/m^2; inset, Figure 2-23). Shallow (100-300 m) temperatures within the upflow zone reach about 41 ^oC (Owens, 2013). Over this depth range, the temperatures are largely isothermal indicating an upflow zone (Bredehoeft and Papodopolus, 1968). Wells with geochemical data up hydrogeologic gradient to the west of this area within the La Jencia basin have much lower concentrations (< 0.25 mg/l). Unfortunately, there are no wells directly up hydrogeologic gradient to the west of the known hydrogeologic window within the La Jencia basin. Thus, the ability of particle-tracking analysis to delineate the location of the hydrogeologic window is not very precise at the intersection between the Socorro and La Jencia basin within the Socorro Peak block. There are additional wells that could be sampled to address this issue (see discussion Section 2.4.7 below).

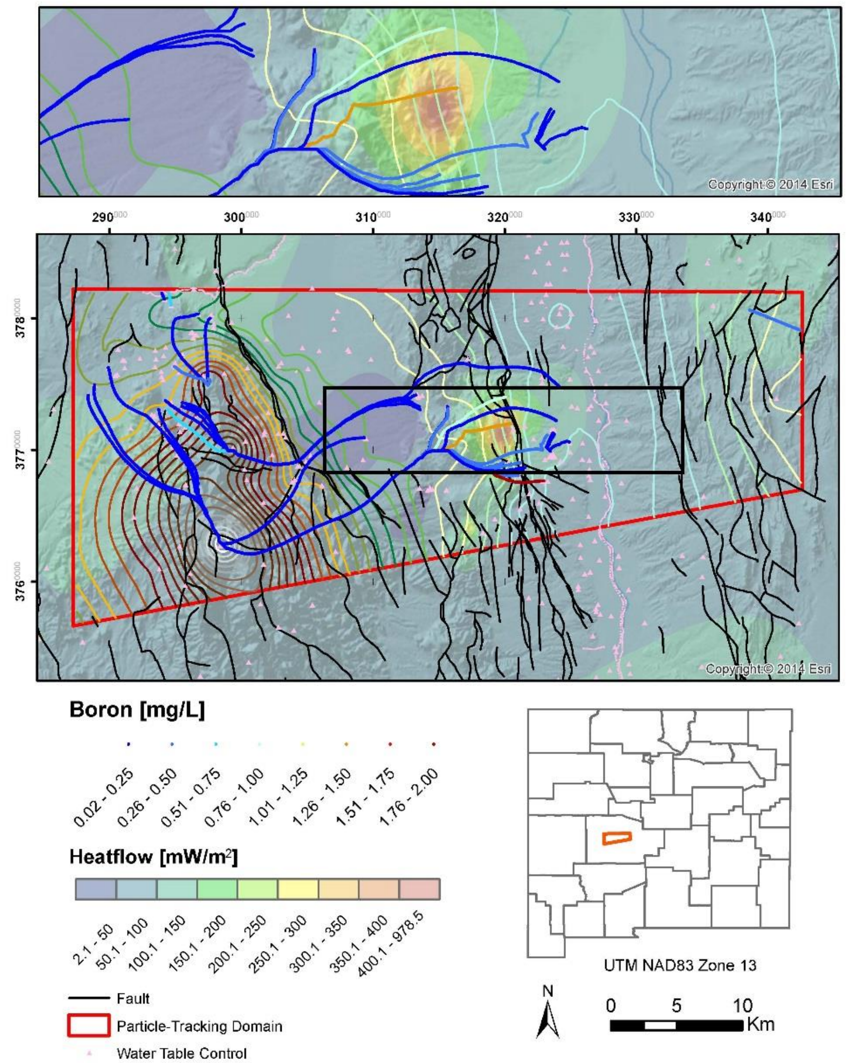

Figure 2-23: Boron particle trajectories for the Socorro La Jencia Basin (colored lines), heat flow (shaded color patterns), and fault locations (black lines). Heat flow is shown using the shaded (red to blue) patterns. Inset shows the particle trajectories and heat flow near the base of M-Mtn. which is the site of highest heat flow across the basin.

2.4.2.3 Acoma Region

Geothermal resources within the Acoma Basin were discussed by Goff et al. (1983). These authors concluded that the high-temperature geothermal potential in this region is limited. This region is situated at the intersection of the Colorado Plateau and the Rio Grande rift along the Lucero Uplift (Callender and Zilinski 1976). However, the chalcedony geothermometer in some wells within the Lucero uplift are as high as 30-60 ^{o}C (Figure 2-10) and this region may host a low temperature resource. Within the Acoma study area, there are a series of wells located on the Comanche fault and associated fault splays that have elevated boron and lithium concentrations. These occur within hydrogeologic windows where Cretaceous confining units have been eroded away (cross-hatched pattern, Figure 2-24). To the south of the Comanche fault within the Acoma study area, crystalline basement crops out (see cross-sectional modeling section). While there is an abundance of down gradient wells with low boron concentrations, there are a limited number of up gradient wells to the west with published boron and lithium concentration data. The San Andres aquifer comes close to the surface to the west of the fault that seems to be the source of the elevated conservative ion concentrations in the middle of the Acoma Basin. That fault seems to be dying out, forming horsetails to the north.

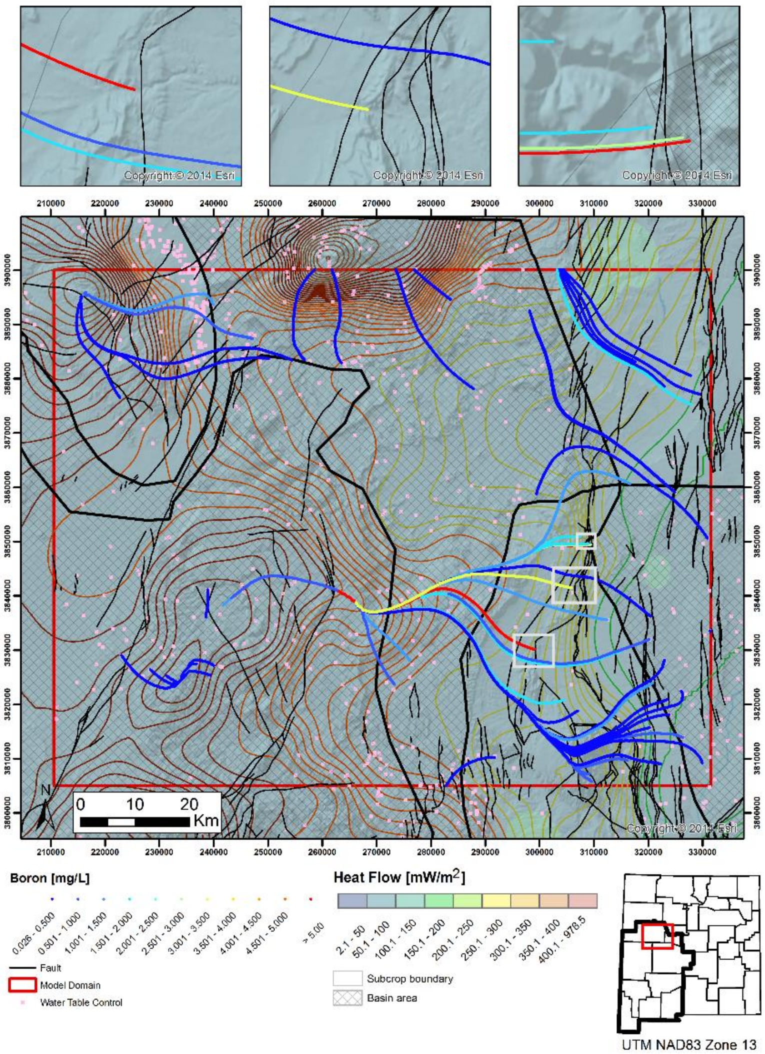

Figure 2-24: Boron particle trajectories for the Acoma basin (colored lines) heat flow (shaded color patterns), and fault locations (black lines). The cross-hatched pattern shows the location where Cretaceous confining units are present. Inset shows particle trajectories along segments of the Comanche fault zone. Heat flow is shown using the shaded (red to blue) patterns.

2.4.2.4 Gila

The Gila region in the western portion of our study area has a number of known hot springs (Witcher, 2002b). High temperatures (up to 80 ºC) at depths of less than 100m occur within the Tertiary Bloodgood Canyon Tuff along the Gila River (Witcher, 2002b). The highest heat flow measurements near the small communities of Cliff and Riverside are located north of a bedrock constriction along the Gila River. The region of high heat flow does have four wells with elevated boron concentrations (Figure 2-25).

The elevated boron concentrations from the three closely spaced wells at Riverside (yellow lines) appear to emanate from mapped faults that cut the Pliocene to Pleistocene Gila Conglomerate.

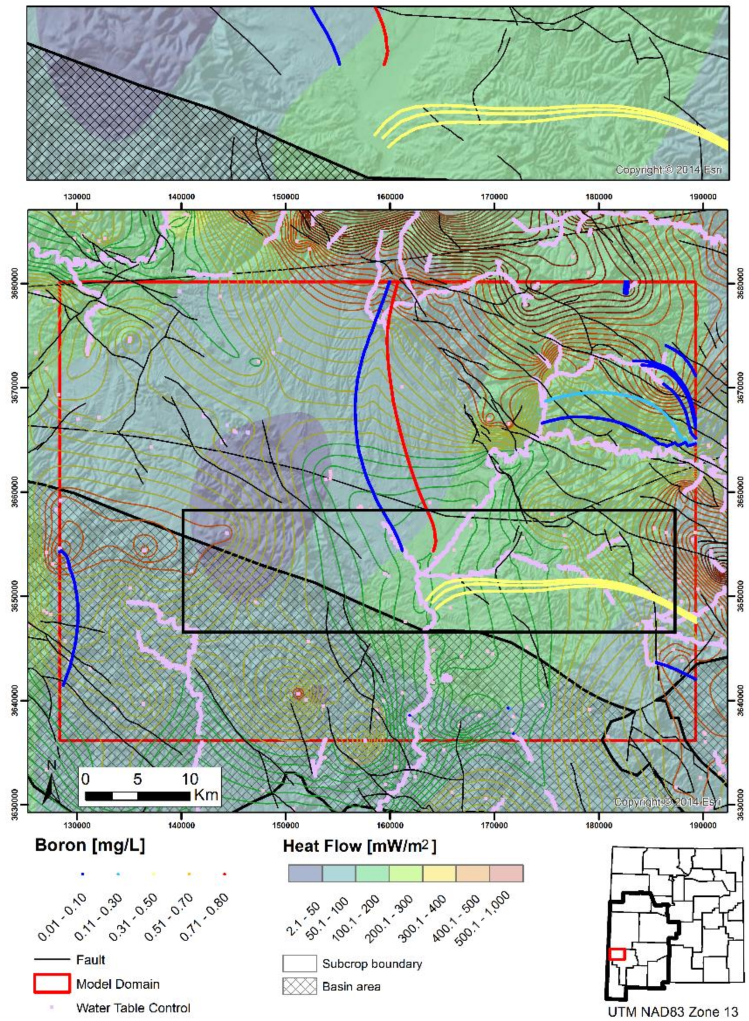

Figure 2-25: Boron particle trajectories for the Gila region (colored lines) and water table contours. Heat flow is shown using the shaded (red to blue) patterns.

2.4.3 Particle-tracking: Discussion & Conclusions

The work presented here represents one of the first attempts to incorporate advective transport into geothermal exploration. When applied to the Socorro geothermal system, high boron concentrations were found to be associated with the known geothermal discharge area at the base of Socorro Peak. Both down gradient wells in Socorro near the Rio Grande and upgradient wells within the La Jencia basin had lower concentrations allowing us to broadly locate the position of the resource. However, the number of wells with measured boron concentration within the La Jencia basin was low and limited our ability to identify the exact position of the upflow zone using existing geochemical data. This could be addressed by targeted geochemical data collection in the future (Figure 2-26). Figure 2-26 suggests that there are about 2-4 times as many unsampled wells compared to wells with geochemical data. The particle-tracking analysis identified potential exploration targets along the Gila River and the Comanche fault within the Lucero uplift. However, similar limitations were found when applying the particle-tracking approach in that there are a limited number of up- and down-gradient wells to refine the location of the geothermal resource. However, Figure 2-26 suggests that additional wells could be sampled and boron and lithium data used to refine the analysis in these regions. Targeted geochemical data collection during Phase II could help to refine the location of potential geothermal resources using particle-tracking.

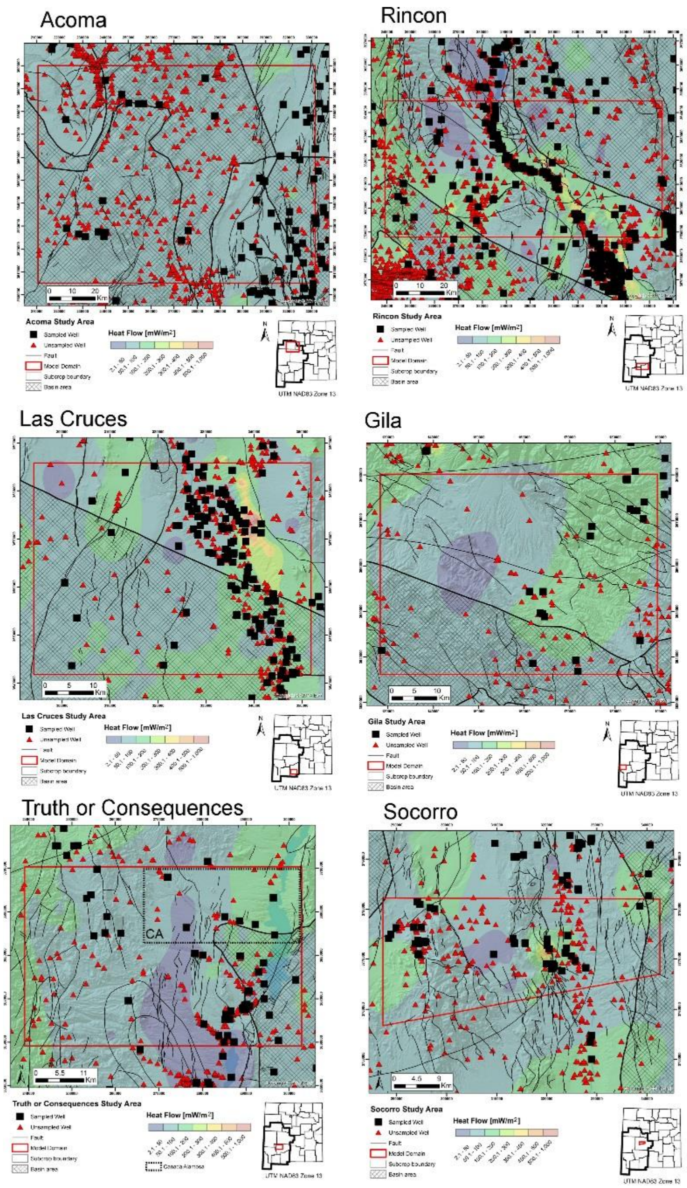

Figure 2-26: Plot showing locations of existing geochemical data (black squares) and wells that have no geochemical data (red triangles).

2.4.3.1 PFLOTRAN Advection-Dispersion Modeling Results

The above particle-tracking analysis only considers advective transport. In reality, transport is both advective and diffusive. We developed a model of advective-dispersive transport for the Acoma region using PFLOTRAN. Potential source locations were evaluated systematically throughout the model domain (e.g. Figure 2-27). Source location size is fixed at approximately 5 km x 5 km squares. A total of 625 source locations were evaluated. Initial concentration throughout the model domain was set to 1×10^{-6} mol/L, approximately the value of lowest measured boron concentrations in the domain. Longitudinal dispersivity was set to approximately 1/10 of the cell size (430 m) and the transverse dispersivity is set to approximately 1/100 of the cell size (43 m). The source strength was calibrated to the boron measurements using a Levenberg-Marquardt algorithm at each potential source location. The objective function of the calibration is the sum-of-squared errors (SSE) defined as

$$\Phi(\theta) = \Sigma(c_{m,i} - c_{s,i})^2$$

where $c_{m,i}$ is the ith measured concentration, $c_{s,i}$ is the ith simulated concentration, and θ is the model parameter representing source strength.

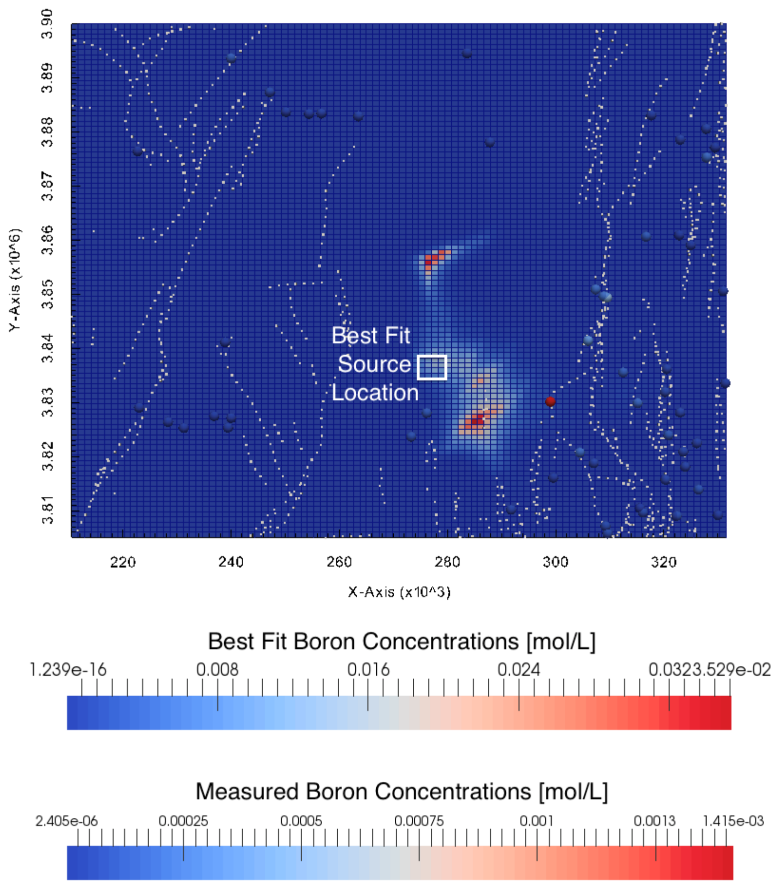

Figure 2-27: PFLOTRAN computational grid and example of one scenario showing simulated boron concentration for best fit source locations (white squares). White dots denote fault locations that could serve as hydrothermal upflow zones.

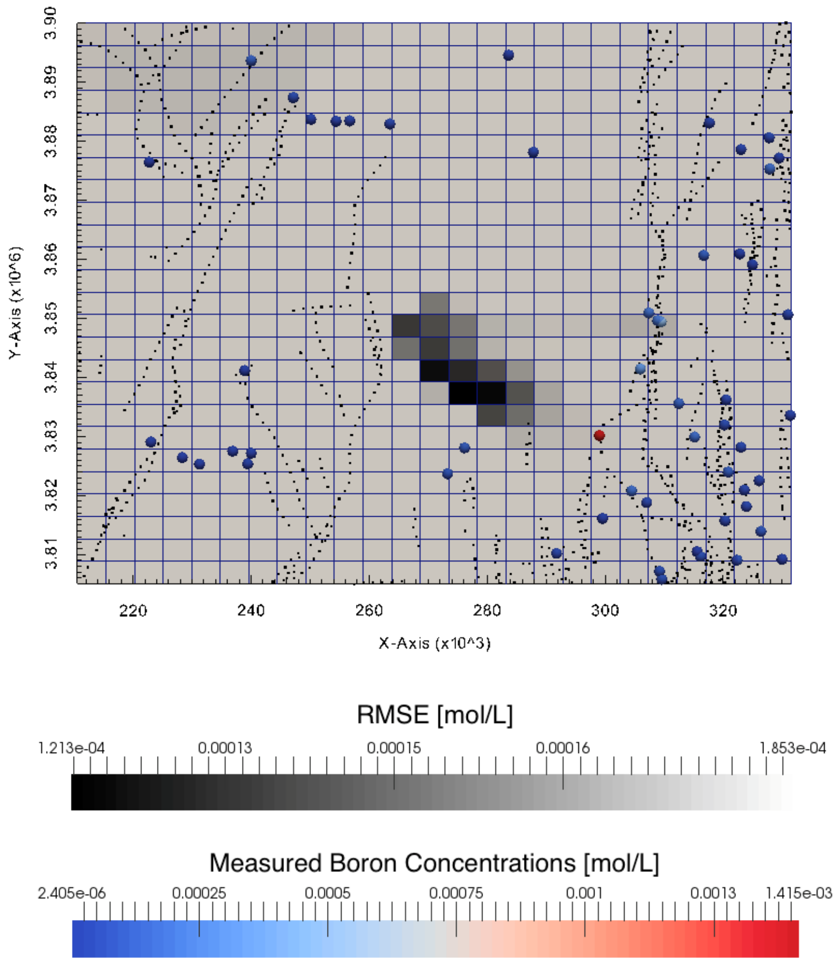

Figure 2-28: Contour map (gray scale) of calculated root mean squared error for 625 potential geothermal upflow zones across Acoma region. Colored circles denote observed boron concentrations. Dotted lines show fault zone locations. The Comanche fault has highest boron concentrations.

Each calibration involved tens of model simulations. The initial source strength of the calibrations are set to 5×10^{-5} mol/L. Preliminary results with dispersivities included as calibration parameters indicated that for most source locations, the dispersivity coefficients were insensitive and not beneficial, and were therefore fixed at the values indicated above. The analysis does not account for fast, preferential pathways, such as fracture flow. Information on preferential pathways is not currently available, but could lead to different results in the analysis.

The optimal source location was determined based on how well simulated concentrations matched measured concentrations using the root-mean-squared-error (RMSE) easily derived from the resulting SSE of the calibrations for each potential source location. By inspection of the Figure 2-28, it is apparent that the analysis identifies a group of source locations near the center of the model domain that are able to match the measured concentrations better that other locations. These locations are up gradient from the highest concentration measurements along the Comanche fault zone. Source locations located nearer to the high concentration measurements along the Comanche fault zone were unable to fit the data as well due to the low concentration measurements down gradient from those locations. These results suggest that the Comanche fault zone may not be the actual source location of hydrothermal fluids. In fact, the fluids appear to be associated with a fault cutting the 3-4 Ma Mesa del Oro lava flow ~20 km to the west. Thus, this conclusion does not contradict the particle-tracking results. Collection of additional well data up gradient from the Comanche fault zone will help to refine these model predictions (Figure 2-24).

2.4.4 Advective-Dispersive Modeling Discussion & Conclusions

Advective-dispersive transport modeling suggests that the optimal source location is located up hydrogeologic gradient from the Comanche fault zone. This scenario is not inconsistent with the particle-tracking results (Figure 2-21 and Figure 2-24). The forward modeling approach requires more parameters (dispersivity, upflow zone concentrations, upflow zone locations) that are not well known. Sensitivity analysis suggested that the results were not highly sensitive to dispersivity. This method would be improved by incorporation of additional data collecting geochemical samples up gradient of the Comanche fault zone (Figure 2-26).

2.5 Integrated Framework Development

The data and ArcGIS layers presented in sections 2.2.5 to 2.2.10 were integrated into a framework to coordinate our work to ultimately produce a "prospectivity map" that indicates the likelihood of a blind geothermal resource based on the hydrogeologic windows concept. Figure 2-29 shows the Integrated Framework.

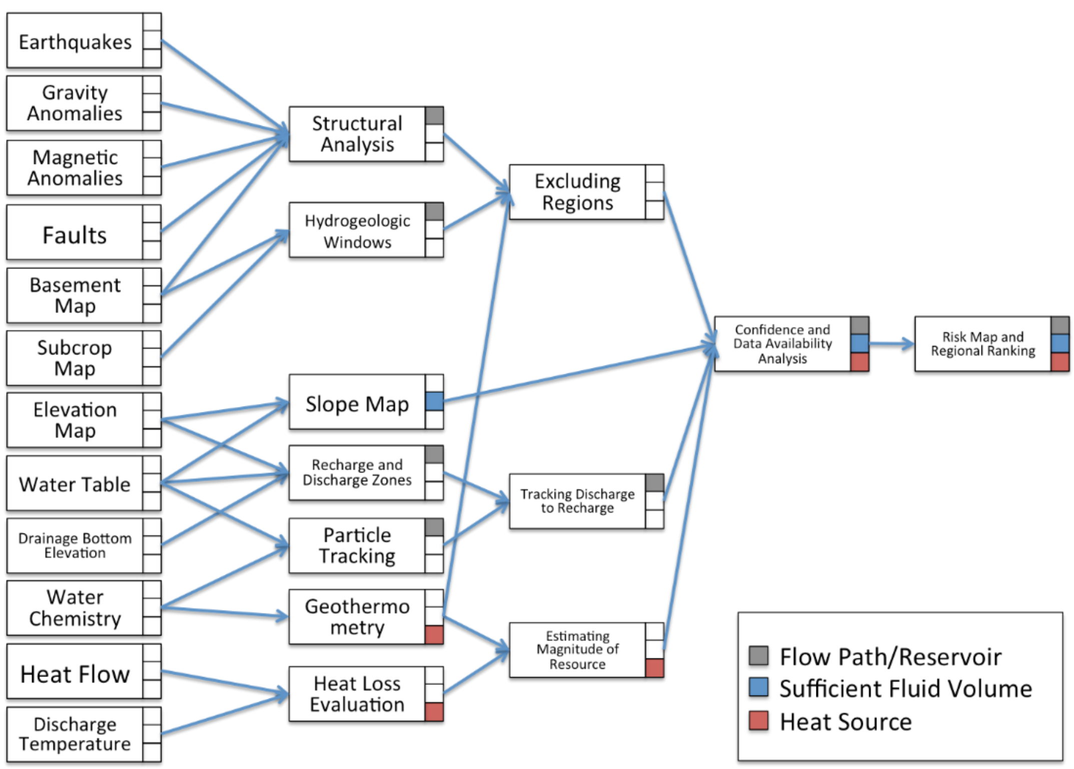

Figure 2-29: The Integrated Framework for Identifying Blind Geothermal Prospects with the Hydrogeologic Windows Concept

The flow indicated in the Integrated Framework is organized around identifying three necessary characteristics of a geothermal resource: permeability, fluid, and heat. Our integrated framework combines outputs from individual analyses in order to enhance the physical understanding of the determinants of a geothermal system and increase the likelihood of the success of future exploration projects. By following this framework, future projects can gain detailed information about the physical properties of geothermal systems—the fluid flow path, the regions that form a reservoir within the flow path, the magnitude of heat source, and the areas where there is sufficient fluid/gravitational potential energy to create an advective geothermal system—as well as a means of ranking the regions that have geothermal potential based upon risk.

Our prospectivity map described in Section 2.5.1 is combines the spatial data and analyses, into one map to indicate the prospects that a location contains an exploitable geothermal system. Here we briefly describe how the data was analyzed and combined to produce the prospectivity map, and more detailed descriptions are provided in Section 2.5.3.

In our framework, some of the data (e.g., subcrops, groundwater discharge regions) are exclusive indicators, meaning that the existence of a hydrogeologic window outside of these regions is theoretically impossible. The other data contribute information about the amount of permeability, heat, or fluid in a location, each of which is necessary but not sufficient for an exploitable geothermal resource (Figure 2-29). Using the point locations of thermal wells and springs as known geothermal resources, we performed spatial association analysis (Section 2.5.3) to determine the thresholds above which heat flow, lithium, boron, and earthquake magnitude are positively associated with known geothermal resources, and determined how the spatial association for each signature depends on the distance of an observation from a geothermal resource.

Typical approaches for spatial association analysis only consider the location of a signature relative to geothermal resources (Carranza, Wibowo, Barritt, & Sumintadireja, 2008; Poux & Suemnicht, 2012). These approaches are suitable for determining a signature may be related to a geothermal resource, but may not take advantage of the magnitude of an observation. For example, the distances between faults and geothermal resources can be used to construct the spatial association curve, but such an analysis depends on the presence or absence of a fault—binary data that does not contain information on magnitude. In contrast geothermometry or earthquake data, for example, contains information on the spatial location of an observation *and* the magnitude of the observation. Holding everything else constant, a higher concentration of lithium in sampled water is likely to indicate that a geothermal resource is closer than if a sample from that same location had a lower concentration of lithium. Conventional spatial association analyses would treat each observation equally, but we developed a method to use data on the magnitude of the observation within the spatial association analyses. This new method was applied to data where observations have a location *and* a magnitude: lithium, boron, earthquakes, and heat flow. The spatial association analysis for known faults, inferred faults, and earthquakes (without magnitude) only used the location of an observation relative to the known geothermal site. The spatial association analyses for each signature are described in more detail in Section 2.5.3.

2.5.1 Prospectivity Analysis

The results of the spatial association analyses for each signature were applied to the observations of that signature. For each observation, the relationship between spatial association and distance was assigned to

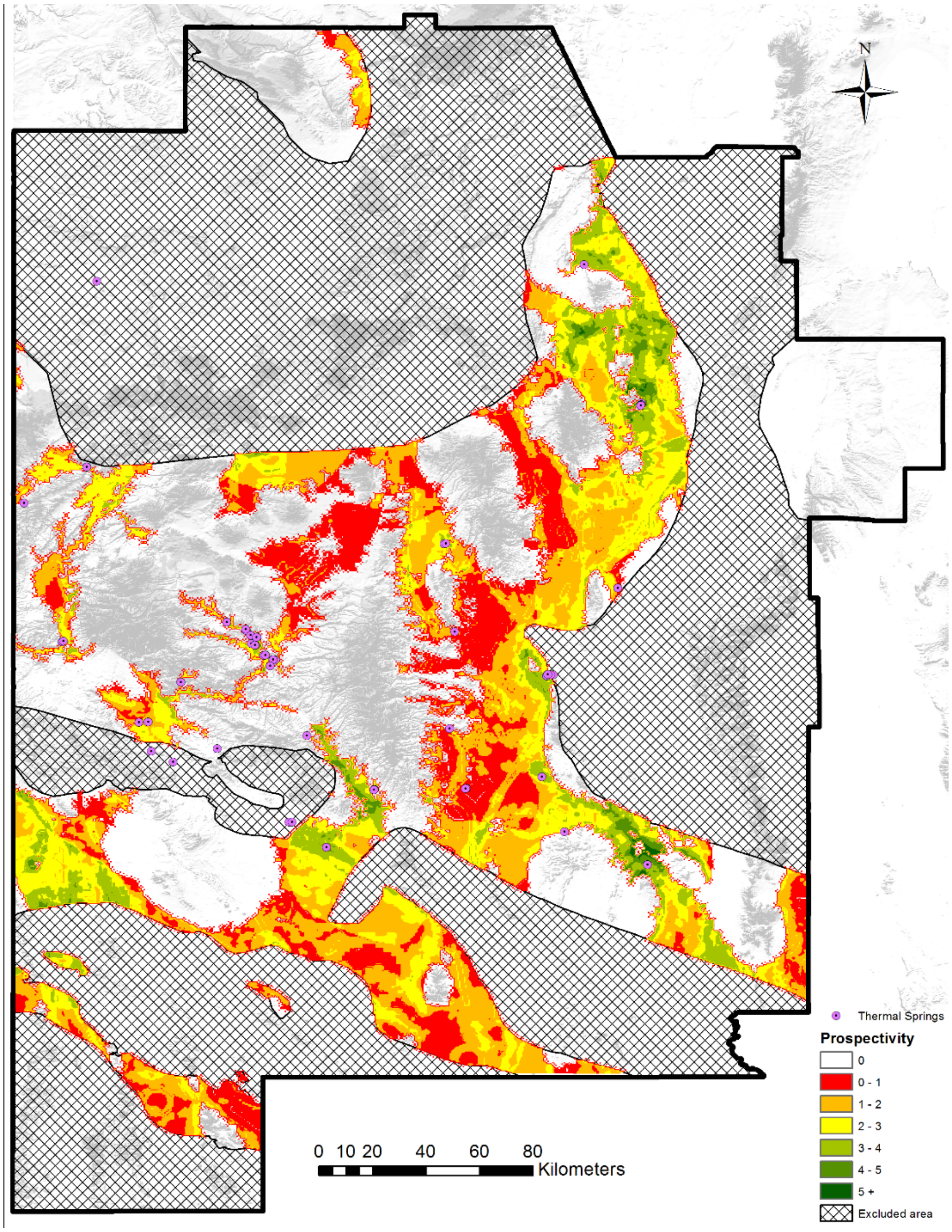

Figure 2-30: Prospectivity Map of Existing and Potential Geothermal Resources.

the location in a manner that emanated radially outward from an observation and, if applicable, took into account the magnitude of the observation. Since the spatial association analysis is a product of analyzing all observations of a signature relative to all known geothermal sites, applying these results spatially can cover areas where there are few observations and improve the ability to infer if an unknown geothermal resource may be present. The prospectivity value was calculated by,

Prospectivity = (HF + BT + KF + IF + Li + B + Eq + ∇WT) x SC x DZ

Where HF = heat flow, BT = basement temperature, KF = known faults, IF = inferred faults, Li = lithium, B = boron, Eq = earthquakes, ∇WT = water table gradient, SC = subcrop, and DZ = discharge zones. In terms of the three necessary characteristics of a geothermal resource, these signatures provide information on the presence of heat (HF, Li, B, BT), permeability (KF, IF, Eq, SC), and fluid (∇WT, DZ). The values for each of the signatures inside the parentheses are scaled between 0 and 1, as described in Section 2.5.3, so that each signature contributes at most the same amount to the overall prospectivity calculation.

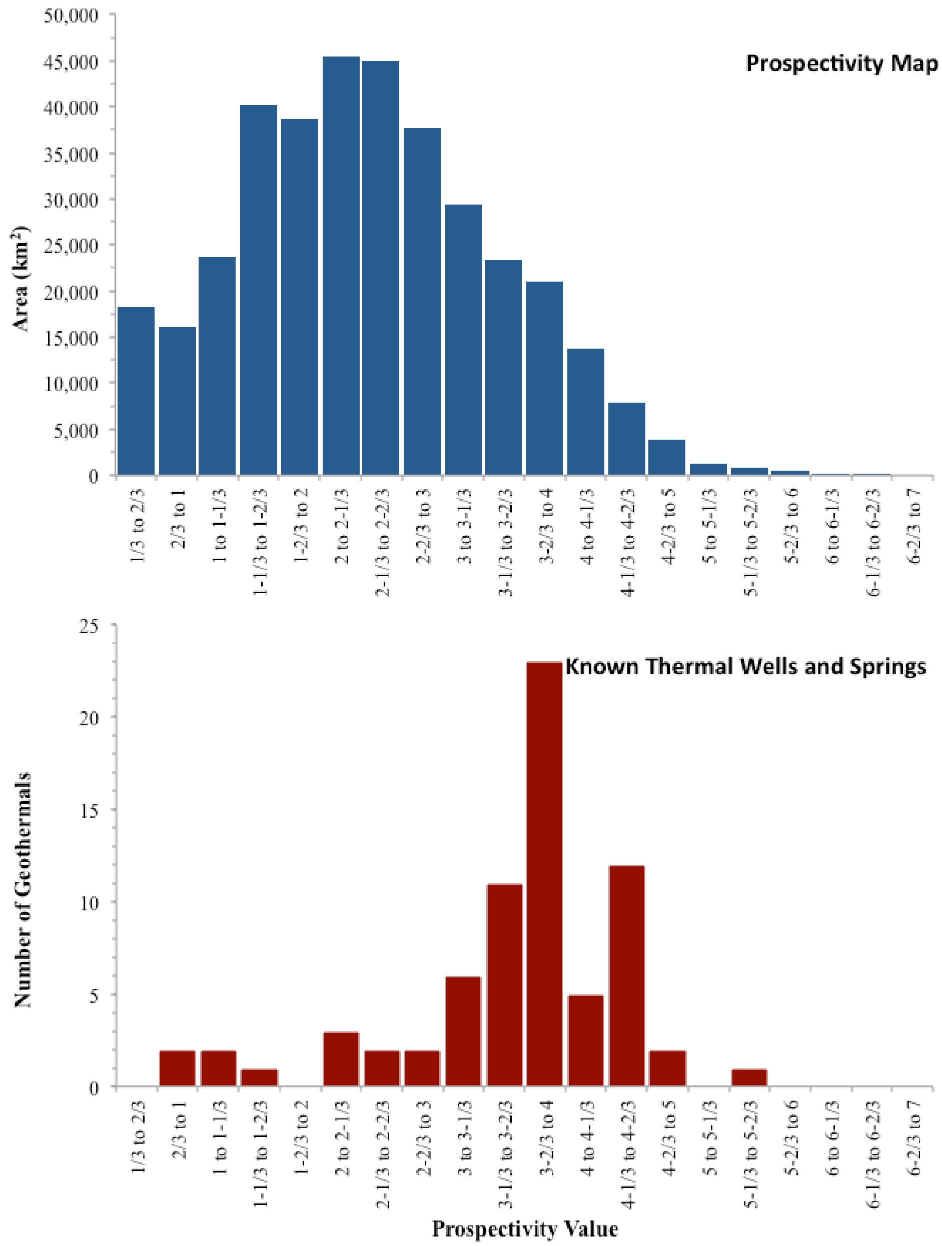

Figure 2-31: Distribution of the Values in The Prospectivity Map (top) and the Prospectivity Values for the Known Thermal Wells and Springs (bottom).

The prospectivity map in Figure 2-30 is color-coded from red to green, where green indicates where the highest estimated prospects for geothermal resources are located. While "risk" might be considered to be the opposite of "prospect" and thus high prospects may be considered to be low risks, we will use the term "prospect" or "prospectivity" instead of "risk". This choice is partly because we believe that "prospectivity" is more consistent with the approach taken here and with the goal for the DOE Play Fairways Analysis projects. In general, high prospectivity values will be less risky targets for geothermal development than areas that have low or zero prospectivity. In addition, the prospectivity map is constructed from available data, from which we are able to develop the "prospects" of the existence of a geothermal resource.

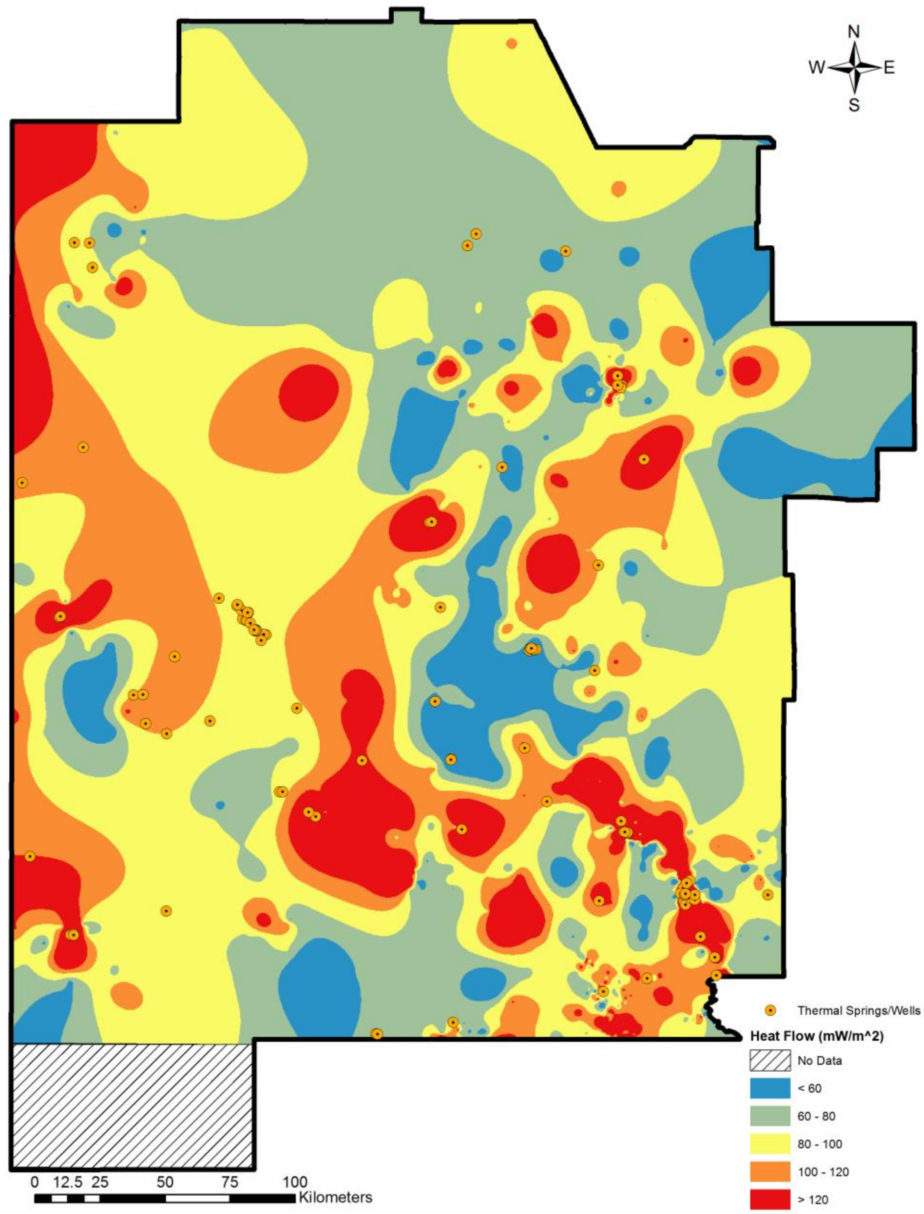

Figure 2-32: Heat Flow Map for Our Case Study in New Mexico.

The prospectivity map in Figure 2-30 also shows the unique locations of 55 known thermal springs and of 60 known thermal wells for a total of 115 unique locations of known geothermal sites. In total, we used data on 170 thermal spring and 355 thermal wells, but there were only 115 unique locations in these data. The known geothermal sites should have high prospectivity values if the concept of hydrogeologic windows and our analysis and integration of the signatures, as outlined in the integrated framework (Figure 2-29), are useful for locating geothermal resources. Figure 2-31 shows that the known geothermal sites are indeed predicted very well by the prospectivity map. The top of Figure 2-31 shows distribution of the area within the prospectivity map by the prospectivity value. The bottom of Figure 2-31 shows distribution of the known geothermal sites by the prospectivity value, and is skewed to the left with most of the known geothermal sites having high prospectivity values, whereas the distribution of the area in the prospectivity map is skewed to the right, with the majority of the mass of the distribution much lower than for the known geothermal sites.[1]

The prospectivity map in Figure 2-31 also identifies the known geothermal resources better than if heat flow is used alone. Figure 2-32 shows the heat flow map, in which heat flow has been binned into five categories: <60 mW/m^2, 60-80 mW/m^2, 80-100 mW/m^2, 100-120 mW/m^2, and > 120 mW/m^2. The heat flow map is used for this initial comparison because heat flow provides a simple point of departure for assessing prospective areas for their geothermal potential, and areas with heat flow above 100 mW/m^2 (orange and red in Figure 2-32) and may be considered areas with high heat flow and could thus be used as an initial screen.

Table 2-4 summarizes the number of thermal wells and springs in the heat flow map in Figure 2-32. The table shows that heat flow with a threshold of 100 mW/m^2 locates about half (62/115) of the known thermal wells and springs. But the area in which the heat flow is greater than 100 mW/m^2 is 24,338 km^2, which is a very large area to cover if prospecting for potential geothermal locations. Further, a cluster of 23 known thermal wells and springs (roughly halfway between the northern and southern boundaries of the area, and roughly 1/3 to the east of the western boundary) is not in the area with high heat flow; these known geothermal sites are in the area where the heat flow is only 80-100 mW/m^2. This is partly due to the lack of heat flow data—which are data at a point—throughout the case study region, and thus the heat flow map is based in part on interpolations of point data, which further highlights shortcomings in alternative approaches to identifying geothermal prospects.

Table 2-4: Characteristics of How the Heat Flow Map Identifies Known Thermal Wells and Springs (Geothermal sites) within Our Case Study in New Mexico

Heat Flow (mW/m^2)	**Geothermal Sites In Area**	**Area (km^2)**	**Density (geothermal sites/km^2)**
60+	106	86,968	0.001
80+	99	58,130	0.002
100+	62	24,338	0.003
120+	52	7,867	0.007

Figure 2-33 shows that there are 53 thermal wells and springs in areas where the heat flow is less than 100 mW/m^2, but twenty of those 53 known geothermal sites are in areas with positive prospectivity if heat flow is not considered in the prospectivity calculation. In contrast, there are 47 thermal springs and wells that

[1] There are 43 thermal wells and springs with prospectivity values between 0 and 1/3 that are not shown in Figure 2-31, because there are 1.5 million km^2 in this bin. This amount of area is roughly two orders of magnitude larger than the area in the rest of the bins for the prospectivity values. Showing this bar would distort the depiction of the distribution of prospectivity values, even if the Y-axis is shown on a log scale.

exist in regions with a prospectivity value of 0, of which only 14 are inside the regions with heat flow greater than 100 mW/m^2.

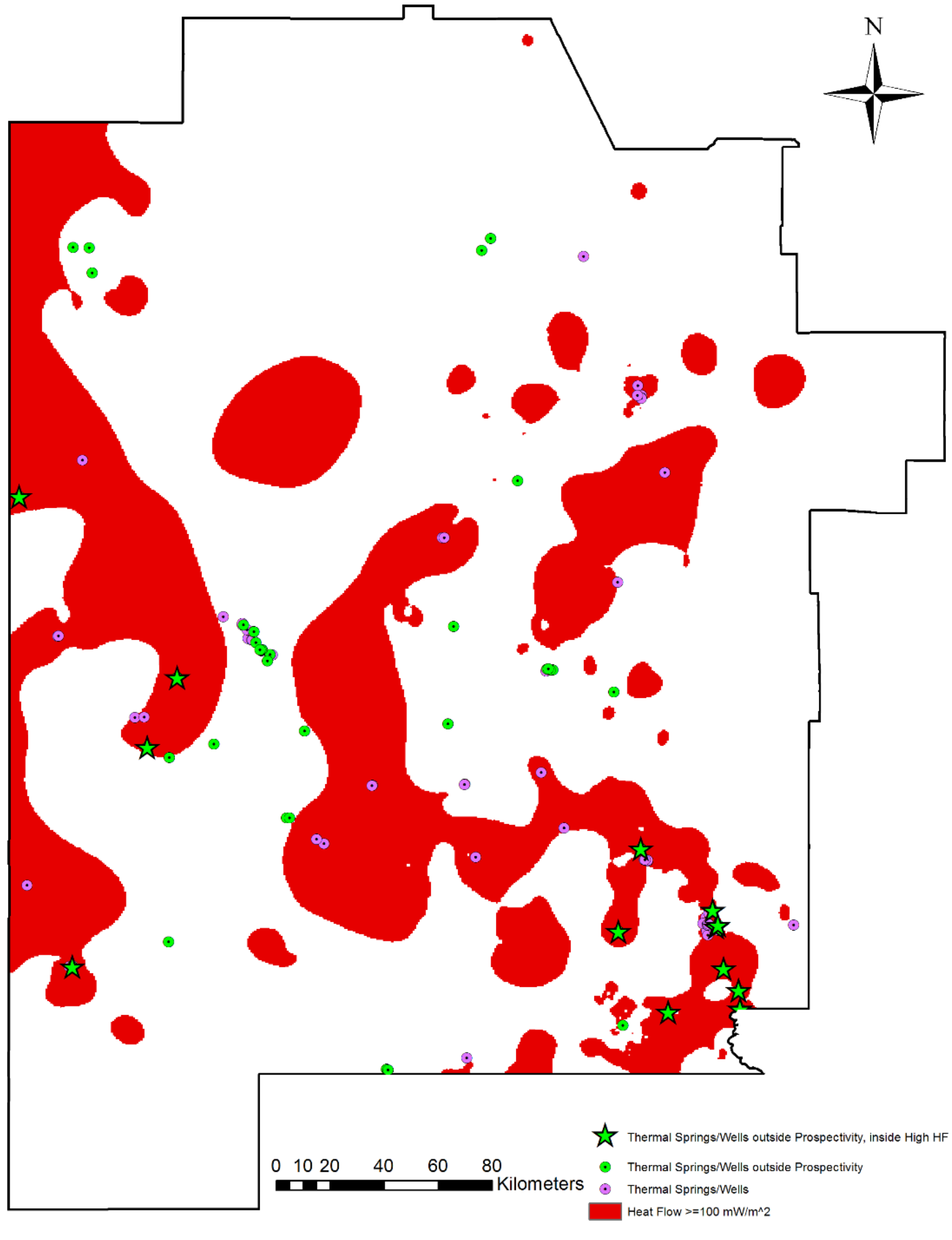

Figure 2-33: Fifty-Three Wells are Outside of Regions with Heat Flow > 100 mW/m^2, Only 14 out of 47 thermal springs and wells without a Prospectivity Value are in areas with >100 mW/m^2.

Our prospectivity map identifies known geothermal sites with better resolution than heat flow alone. For example, there is a thin line with positive prospectivity in Figure 2-30 that traces the same arc as this cluster of thermal wells and springs (average prospectivity for these geothermal sites is 3.2, max is 4.0). Further, the prospectivity map substantially reduces the area to consider. Table 2-5 shows a summary of the Prospecitivity map. Table 2-5 shows that 62 known geothermal sites are located in areas with a prospectivity value greater than two, which equals the number that are identified in the region with high heat flow (>100 mW/m^2) in Figure 2-30. The area with prospectivity greater than two is also much smaller than the area with high heat flow: 7,906 km^2 vs. 24,338 km^2. The density of the number of thermal wells and springs that are located per unit of area is 0.008 for the prospectivity map, and more than 2.5x the density in the heat flow map (0.003). For higher heat flow (>120 mW/m^2) 52 known geothermal sites are in an area of 7,867 km^2, whereas 42 are identified in a much smaller area (2,702 km^2) with prospectivity greater than 3, and the density is more than twice as much.

Table 2-5: Characteristics of How Our Prospectivity Map Identifies Known Thermal Wells and Springs (Geothermal sites) with Our Case Study in New Mexico – The left side of the table is based on the value in the prospectivity map, and the right side of the table is based on the quintile in which the prospectivity value falls.

Value	Geothermal Sites	Area (km^2)	Density	Quintile (Prospectivity Value)	Geothermal Sites	Area (km^2)	Density
> 0	68	18,375	0.004	>0% (0.00)	68	18,375	0.004
> 1	65	14,547	0.004	>20% (0.96)	65	14,697	0.004
> 2	62	7,906	0.008	>40% (1.46)	64	11,009	0.006
> 3	42	2,702	0.016	>60% (2.06)	61	7,338	0.008
> 4	6	454	0.013	>80% (2.73)	52	3,654	0.014

The right side of Table 2-5 summarizes the prospectivity map by quintiles, in order to characterize the efficacy of the prospectivity map in a way that considers the imperfect and incomplete data. The prospectivity value corresponding to each quintile is indicated in parentheses under the percentage of the quintile. The quintiles reinforce the depiction of the distribution of prospectivity values by area in Figure 2-31. For example, 80% of the area with positive in the Prospectiviy map has a prospectivity value of 2.73 or less. There are 52 known geothermal sites located in the 3,654 km^2 that have prospectivity values in the top 20% (i.e., > 2.73).

We also compare our prospectivity map with maps that use data typically used for geothermal prospecting: heat flow, lithium, boron, and subsurface faults. We present these results in two ways, one which depends on the presence or absence of data indicating a potential geothermal resource and a more nuanced analysis that uses our approach for producing prospectivity values with only these data.

Table 2-6: Basic Analysis of Geothermal Prospectivity Using Heat Flow, Lithium, Boron, and Known Faults – The "Presence" analysis on the left side of the table was conducted with a 1 assigned if the signature was present above a threshold, 0 otherwise. The "Prospectivity" analysis on the right side of the table used the results of our analysis of the signatures.

Value	PRESENCE (1-0)			PROSPECTIVITY ANALYSIS		
	Geothermal Sites	Area	Density	Geothermal Sites	Area	Density
>0	110	72,670	0.002	110	72,670	0.002
>1	91	35,377	0.003	91	27,303	0.003
>2	49	10,522	0.005	23	3,657	0.006
>3	7	975	0.007	6	187	0.032

Figure 2-34 shows the prospectivity map for this basic analysis, and corresponds to the right side of Table 2-6. Table 2-7 has the data for the quintiles associated with the prospectivity analysis. A direct comparison between the left side of Table 2-5 and of Table 2-6 cannot be made because the number of signatures that are being used are different, and thus the maximum prospectivity values differ between the basic analysis and the analysis with all of the signatures. The quintiles as presented in Table 2-7 facilitate a more robust comparison. In general, the basic analysis does not reduce the area of interest or the density of known geothermal sites in that area as well as the prospectivity analysis using all of the signatures, as shown in Figure 2-30 and in Table 2-5.

Table 2-7: Prospectivity Quintiles for Basic Analysis using Heat Flow, Lithium, Boron, and Known Faults

Quintile	Geothermal Sites	Area	Density
>0% (0)	110	72,670	0.002
>20% (0.33)	108	60,349	0.002
>40% (0.67)	104	44,434	0.002
>60% (1.00)	91	27,303	0.003
>80% (1.67)	68	12,294	0.006

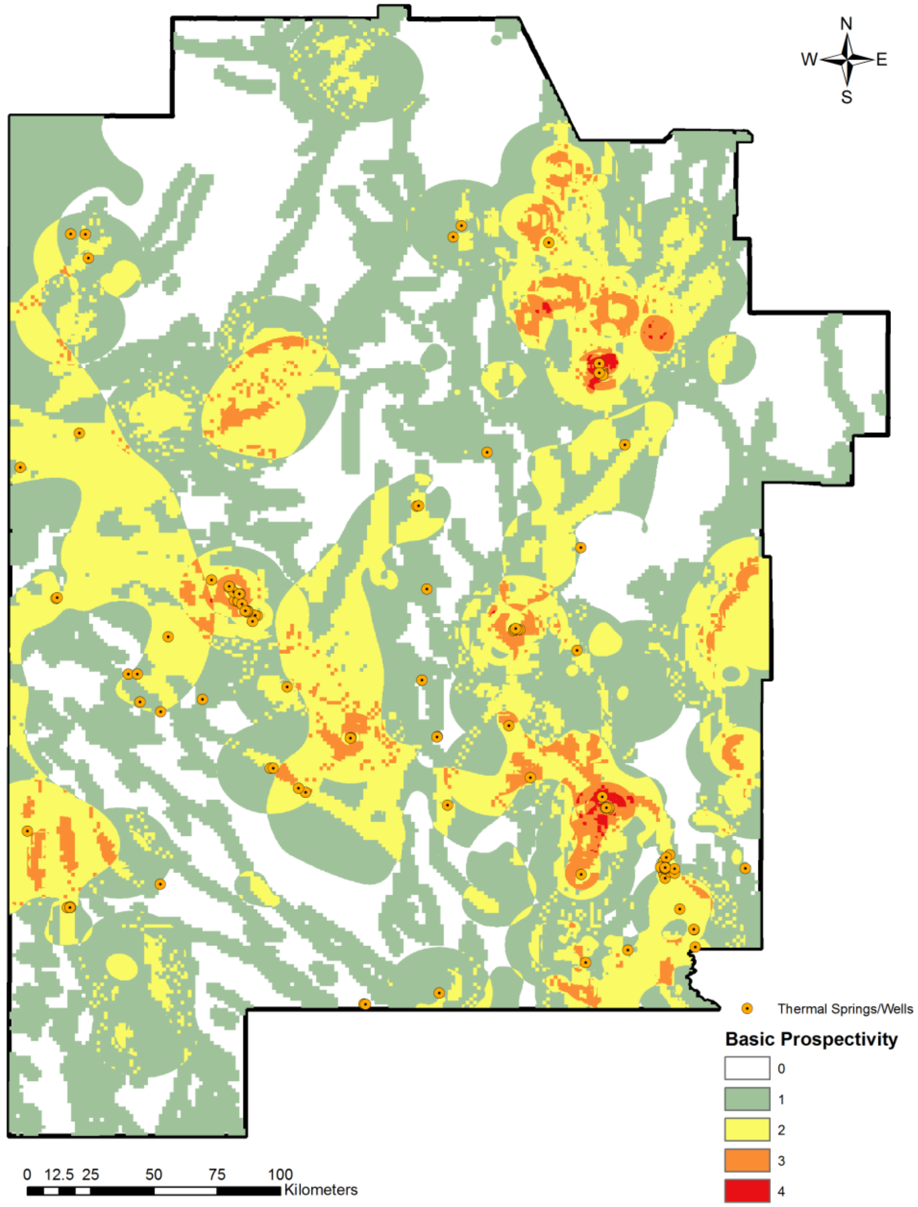

Figure 2-34: Prospectivity Map for Basic Analysis including only Heat Flow, Lithium, Boron, and Known Faults

In addition to this comparison between the prospectivity map using all of the signatures (Figure 2-30, Table 2-5) and one using a reduced number of typical signatures (Figure 2-34, Table 2-6, Table 2-7), we also investigated the sensitivity of the results if one signature were removed from the prospectivity analysis. Each marker in Figure 2-35 is for a quintile of the prospectivity analysis results. The thick, black line indicates the results for the number of known geothermal sites that are within the area identified by the quintile. The thin grey lines indicate the results for removing one signature. Removing one signature at a time could inform decisions about prioritizing data collection of one signature over the other, but there is no consistent trend that allows us to have a definitive conclusion about which signatures contribute the least to the results. We can conclude, though, that using the full array of signatures in the prospectivity analysis results in more known geothermal sites being identified in roughly the same amount of area than if a signature is not considered.

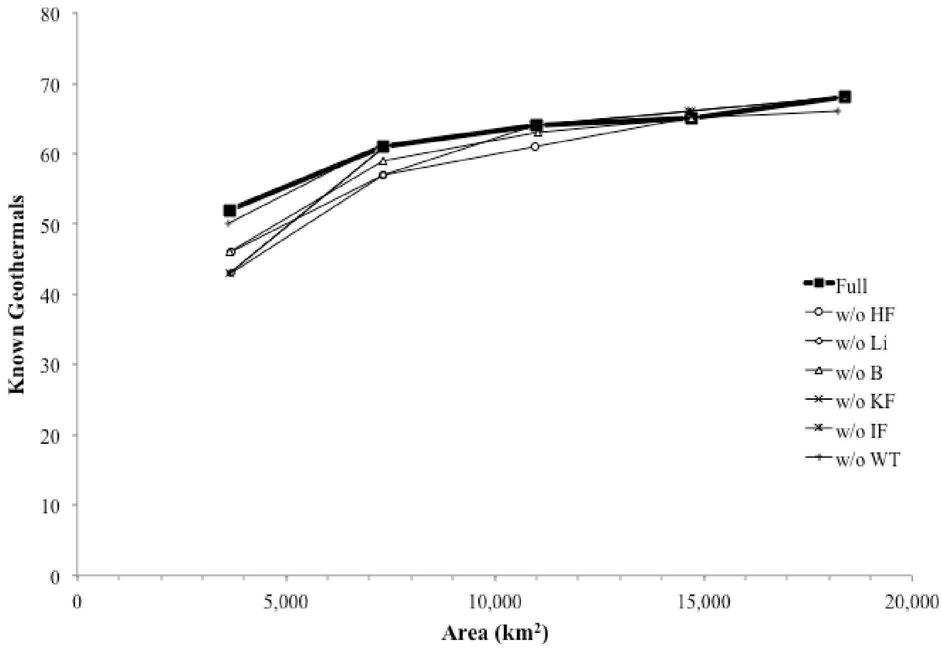

Figure 2-35: Sensitivity of Prospectivity Results to the Removal of Signatures –The thick black line shows the results for the Prospectivity analysis using all of the signatures; the thinner, grey lines are the results of the Prospectivity analysis when one signature is removed. Each marker contains the results for a quintile.

The comparison between the prospectivity map using all of the signatures and those using a reduced number of typical signatures indicates that our implementation of an integrated framework based on the hydrogeologic windows concept results in the capability to narrow in on geothermal prospects in a way that improves upon existing approaches that may use a simpler analysis of a smaller number of geothermal indicators.

2.5.2 Spatial Association Analysis (general methodology)

Our approach to quantifying the spatial association of known geothermal resources with observed signatures is based on the notion that randomly distributed observations will have an intensity (λ) that is uniform across an area (A), where intensity is defined as the number of expected observations per unit area. A spatial point process is the stochastic process through which values are assigned to an observation in space. Under a random distribution (a homogeneous Poisson process), the intensity of the entire region A should be $\hat{\lambda} = \frac{N}{|A|}$, where N is the number of events in the region, and $|A|$ is the area of the region. If the spatial point process responsible for assigning values to these points is also a random process, points can be removed based upon these assigned values, and this removal process will be equivalent to removing the points at random. Removing points at random will not alter the intensity, and therefore λ will remain uniform throughout the region A. If the values are not randomly assigned, but instead reflect some underlying spatial distribution, then the intensity will vary within the region A based upon the spatial point process responsible for generating these values. For example, if the values are a function of the distance from geothermal sites, the intensity around geothermal locations will be higher than in the rest of the study area. Figure 2-36 provides a depiction of this methodology.

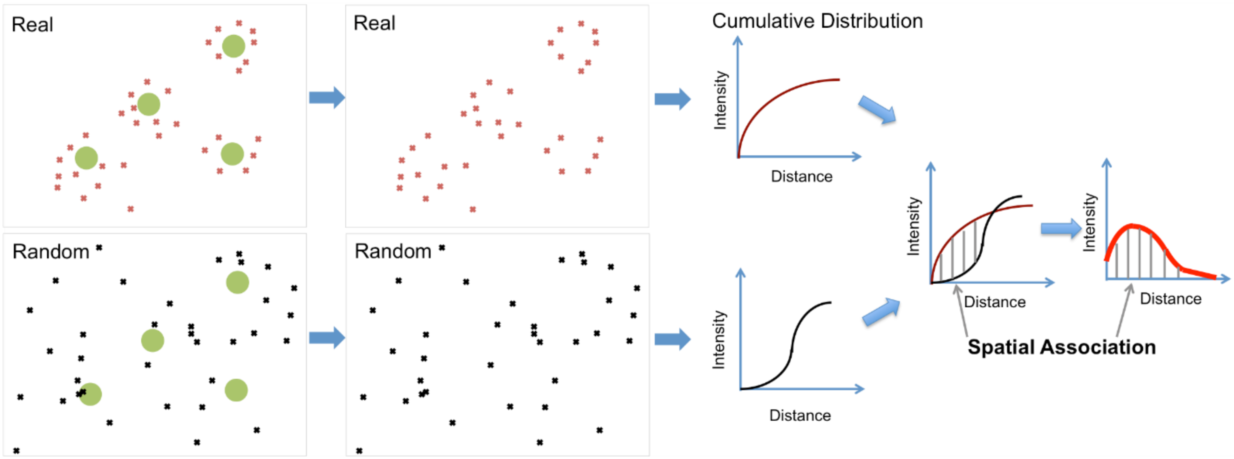

Figure 2-36: Depiction of Spatial Association Methodology

The multivariate K-function describes the expectation for randomly distributed events i with intensity λ_i within a distance h of events in j:

$$K_{ij}(h) = \frac{E[\text{number of events in } i \text{ within } h \text{ of a randomly chosen event in } j]}{\lambda_i}$$

The conceptual outcome of this function is the area within which we would expect to see the given number of points at the given intensity. Under a random distribution of points, without considering edge effects, the value of the K-function should be $\approx \pi h^2$. When edge effects are taken into account, this function can be estimated by:

$$\widehat{K}_{ec}(h) = (\widehat{\lambda_\iota} \widehat{\lambda_J} A)^{-1} \sum_k \sum_l w(i_k, j_l) \cdot \delta(d(i_k, j_l) < h)$$

where $\widehat{\lambda_\iota}$ is the intensity of the events in i, $\widehat{\lambda_J}$ is the intensity of the events in j, A is the area of the study region, $d(i_k, j_l)$ is the distance between events in i and j, $\delta(d(i_k, j_l) < h) = \begin{cases} 1 & d(i_k, j_l) < h \\ 0 & d(i_k, j_l) \geq h \end{cases}$, and $w(i_k, j_l)$ is the ratio $\frac{2\pi d(i_k, j_l)_{in}}{2\pi d(i_k, j_l)}$, or the fraction of the circumference that lies inside the boundary (Dixon, El-shaarawi, & Piegorsch, 2002). The deviation from randomness can be determined by using $\hat{L}$, where $\hat{L}(h) = \sqrt{\frac{\widehat{K}_{ec}(h)}{\pi}}$. The conceptual outcome of this function is the radius that will sweep out the necessary area as defined by the K function. So if the data were generated randomly, $\hat{L}(h) - h \approx 0 \; \forall h$. The $\hat{L} - h$ plot is referred to as the $\hat{L}$ plot (Waller & Gotway, 2004).

The values for $\widehat{\lambda_J}$ and A will remain constant for the $\widehat{K}_{ec}$ function. Therefore, holding h constant as well, $\widehat{K}_{ec}$ will increase as $\widehat{\lambda_\iota}$ decreases. In terms of geothermal resources, as the number of points above the threshold decreases, the amount of spatial association will increase. Because the same is true if the data are generated randomly, the randomly generated data can be used to create an envelope. Still holding h constant, the expected mean of this envelope for K will increase at the same rate as the value for $\widehat{K}_{ec}$, because the only variable for both of these functions is $\widehat{\lambda_\iota}$. Therefore, $\hat{L} - h$ and the expected mean of $L - h$ would also increase at the same rate. So, by subtracting only the expected mean values of $L(h)$ from the values of $\hat{L}(h)$, we can determine the degree of spatial association for a given concentration threshold, determining $\widehat{\lambda_\iota}$. Holding $\widehat{\lambda_\iota}$ constant, and varying h, the expected mean of $L - h$ should remain equal to zero, while the value of $\hat{L} - h$ should vary, thus revealing the degree of spatial association at the distance h. By rotating this function around each observation on a map we can obtain circular distributions of spatial association, or “ripples” that emanate outward from an observation. The radial distributions for each signature are the basis for the prospectivity signature layer, where the values of spatial association for these “ripples” are linearly is scaled so that the maximum value is one.

2.5.3 Spatial Association Analysis (Application to Signatures)

2.5.3.1 Geochemical tracers/Geothermometers

We conducted spatial association analyses on the various geochemical tracers/geothermometers data (Section 2.2.8). We prioritized the analyses of lithium, boron, and chalcedony during the development of the approach to spatial analysis that considers the magnitudes of the observations, and thus we were not able to include spatial association analyses of the ratios (Cl/Br, Li/Cl, and B/Cl) in Phase I. In our analysis, lithium and boron concentrations displayed spatial association that decreased rapidly with distance (Figure 2-37, Figure 2-38). These two geochemical tracers also had substantial spikes in their respective spatial association for concentrations above a given threshold (Li ≥ 1.315 mg/L, B≥ .839 mg/L). Our initial analyses of spatial association for Chalcedony concentrations displayed neither of these trends, and thus we not included in the present version of the prospectivity map (Figure 2-30).

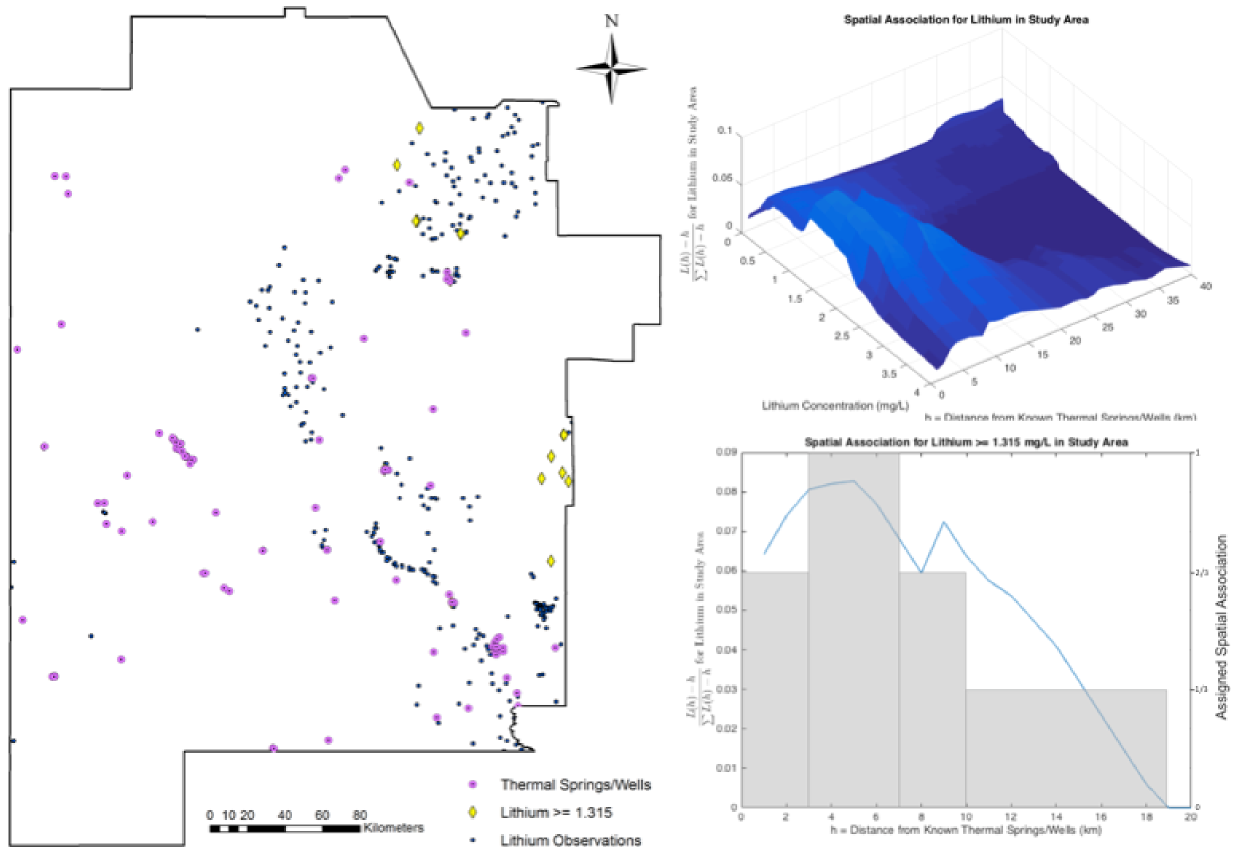

Figure 2-37: Lithium Observations, Spatial Association by Concentration and above a Threshold of 1.315 mg/L.

Figure 2-39 shows an example of how the results of spatial association analyses were included in the prospectivity map. We partitioned each spatial association curve into quartiles and assigned the weighted average of the spatial association curve within each quartile as the prospectivity value for that quartile. The distances associated with each quartile defined the inner and outer radii of a buffer that was applied to the prospectivity map around an observation. For example, the buffers for observations of boron above the 0.839 mg/L threshold were assigned the prospectivity values based on distance from the observation as shown in the lower right corner of Figure 2-38. Regions where buffers from different observations of the same signature overlapped were not summed; instead, the maximum value of the buffer quartiles were assigned in order to avoid biasing the overall prospectivity map due to observations of the same signature in relatively close proximity. In Phase II, we plan to improve this method to more precisely represent the spatial association curve.

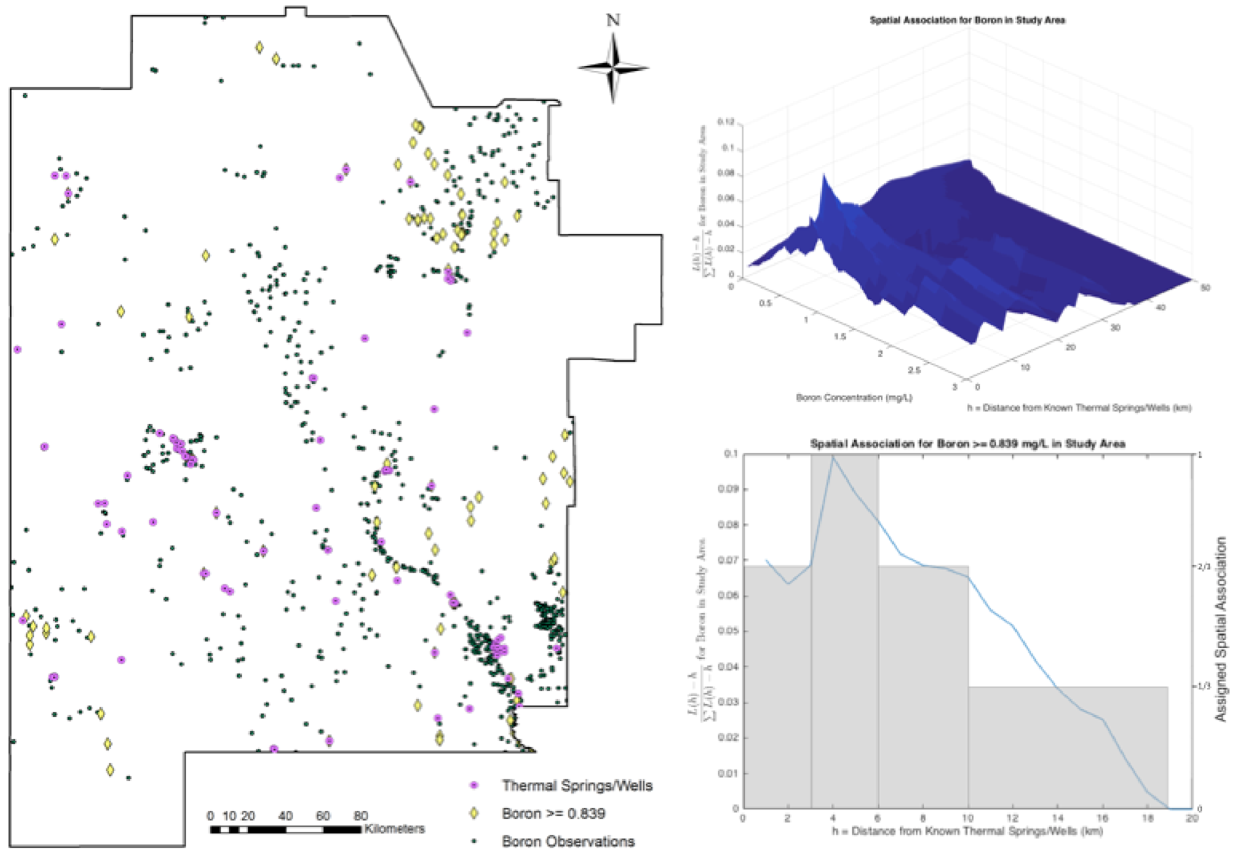

Figure 2-38: Boron Observations, Spatial Association by Concentration and Above a Threshold of 0.839 mg/L.

2.5.3.2 Known Faults

Fault data (Section 2.2.5) provide information about where permeable pathways may allow water to flow through a potential hydrogeologic window to/from the surface or shallower regions in the subsurface (Coolbaugh et al. (2005)). The spatial association between faults and known geothermal sites is essentially zero beyond 2.7 km from a known fault to a known geothermal site (Figure 2-39). We created buffers with a maximum distance of 2.7 km around each fault, where the profile of the value of these buffers as distance increases from the faults to the 2.7 km limit was determined by the distribution of spatial association over that distance.

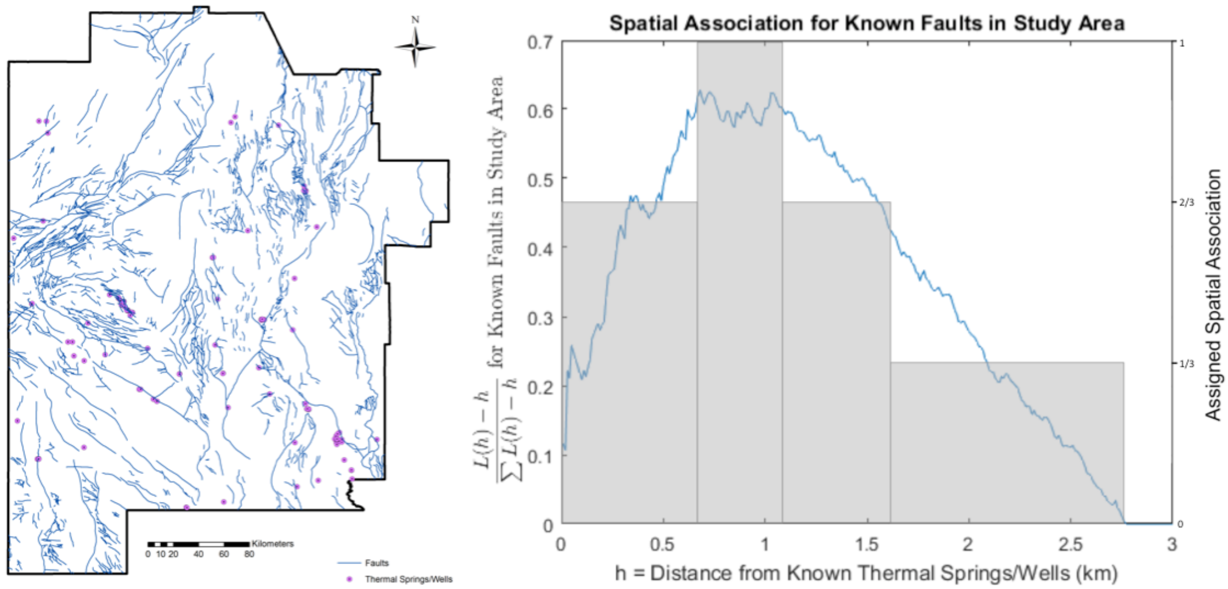

Figure 2-39: Known Faults, Known Geothermal sites, and Spatial Association Between the Faults and the Known Geothermal sites.

2.5.3.3 Inferred Faults

These regions were derived from the gravitational gradient. Areas with large changes in gravity suggest that a discontinuity may exist in the subsurface and may indicate the existence of a fault (Section 2.2.5). These gravitationally-derived, 'inferred faults' could be pathways for fluids to be exchanged and heated between different layers in the subsurface. The spatial association between all earthquakes and known geothermal sites is essentially zero at more than 1.6 km from an earthquake (Figure 2-40). We created buffers with a maximum distance of 1.6 km around each earthquake, where the profile of the value of these buffers as distance increases from the earthquakes to the 1.6 km limit was determined by the distribution of spatial association over that distance.

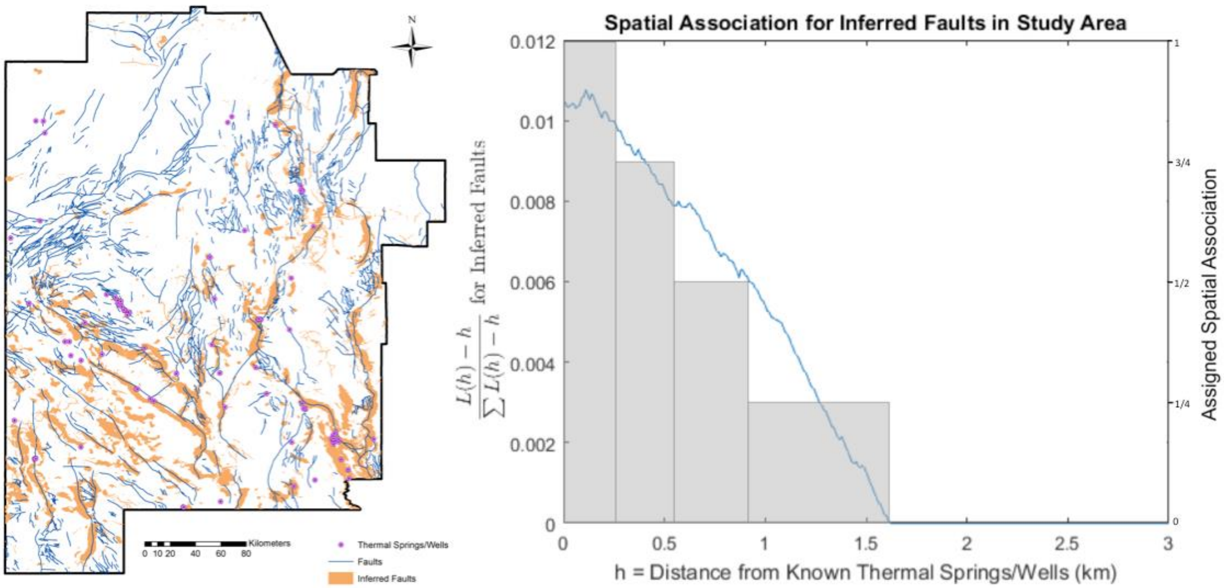

Figure 2-40: Inferred Faults, Known Geothermal sites, and Spatial Association.

2.5.3.4 Earthquakes

Despite having varying magnitudes, our analysis did not identify a discernable trend in the dependence of spatial association on the magnitude of the earthquakes and known geothermal sites. The spatial association between all earthquakes and known geothermal sites is essentially zero at more than 27.6 km from an earthquake. We created buffers with a maximum distance of 27.6 km around each earthquake, where the profile of the value of these buffers as distance increases from the earthquakes to the 27.6 km limit was determined by the distribution of spatial association over that distance (Figure 2-41).

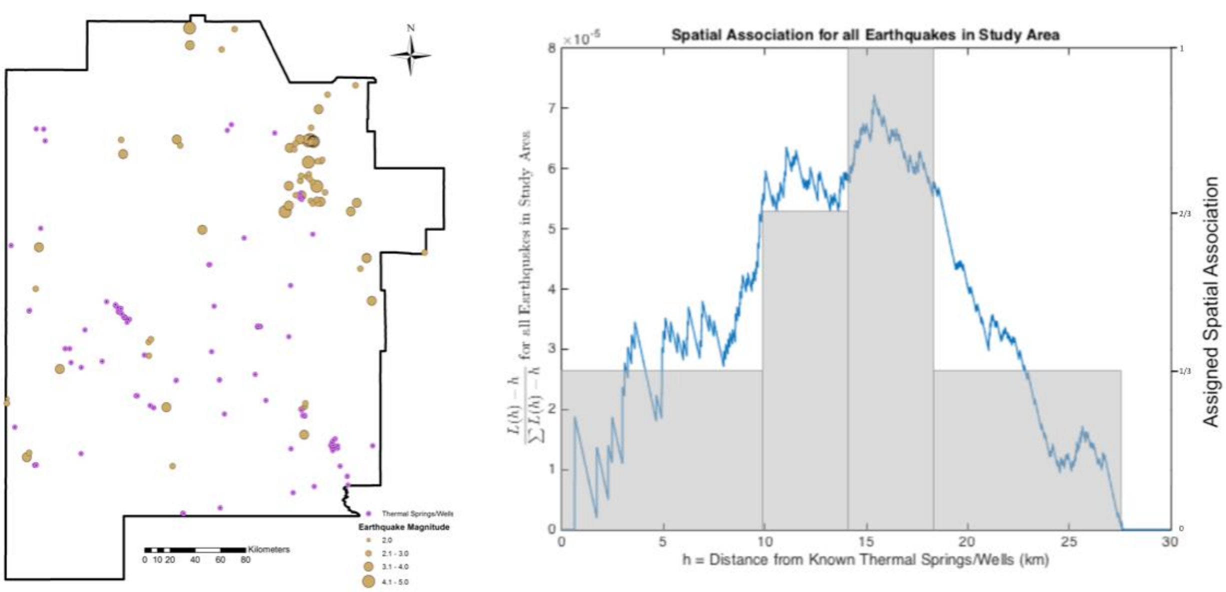

Figure 2-41: Earthquakes, Known Geothermal sites, and the Spatial Association.

2.5.3.5 Heat Flow

Our spatial association analysis of heat flow (Section 2.2.9) had a high spatial association with geothermal resources, but it did not reveal a threshold and extended out to 80 km from known geothermal sites (Figure 2-42). We believe that these results are primarily driven by the lack of heat flow data for regions near many known geothermal sites; for example the cluster of thermal springs and wells that was highlighted in our description of the usefulness of the Prospecitivity Map in Section 2.5.1had an interpolated heat flow between 80 and 100 mW/m^2, which is low. We chose to use a threshold of 100 mW/m^2 assigned a prospectivity value of one to regions with this amount of heat flow or greater. Regions where the interpolated heat flow was below100 mW/m^2 were assigned prospectivity values to zero. In our Phase II proposal, we include tasks to refine the spatial analysis of heat flow to better characterize the relationship of this signature with geothermal resources.

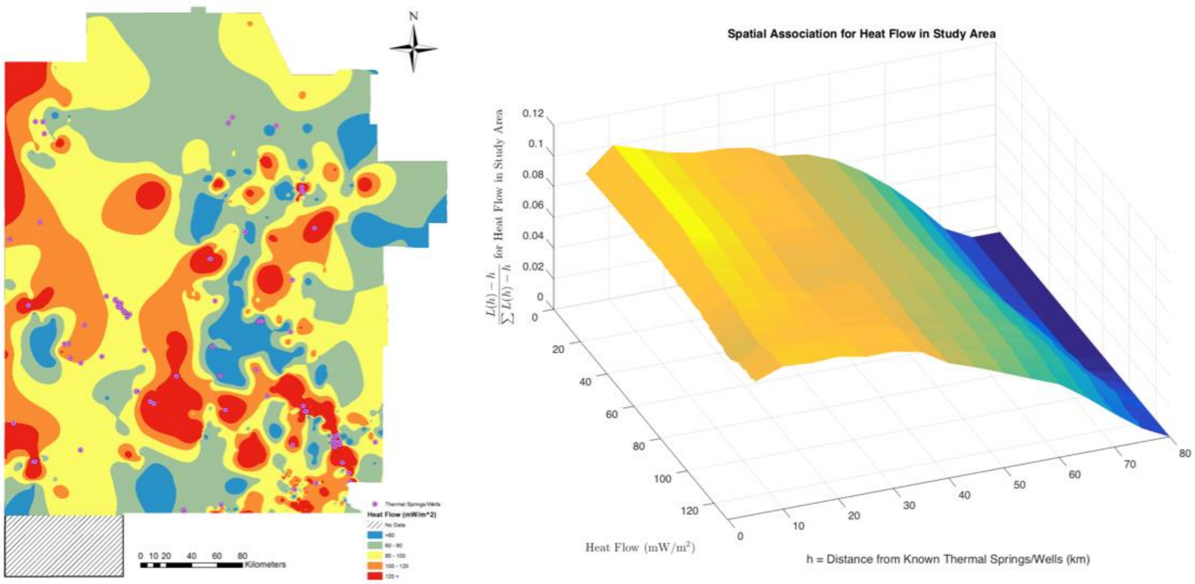

Figure 2-42: Heat Flow, Known Geothermal sites, and Spatial Association.

2.5.3.6 Basement Temperature

Using the geothermal gradient map (Section 2.2.9) and the depth to basement map, we created a basement temperature map of the region. We divided by the maximum value of the basement temperature to establish a normalized basement temperature map (we did not need to subtract the minimum since it was zero).

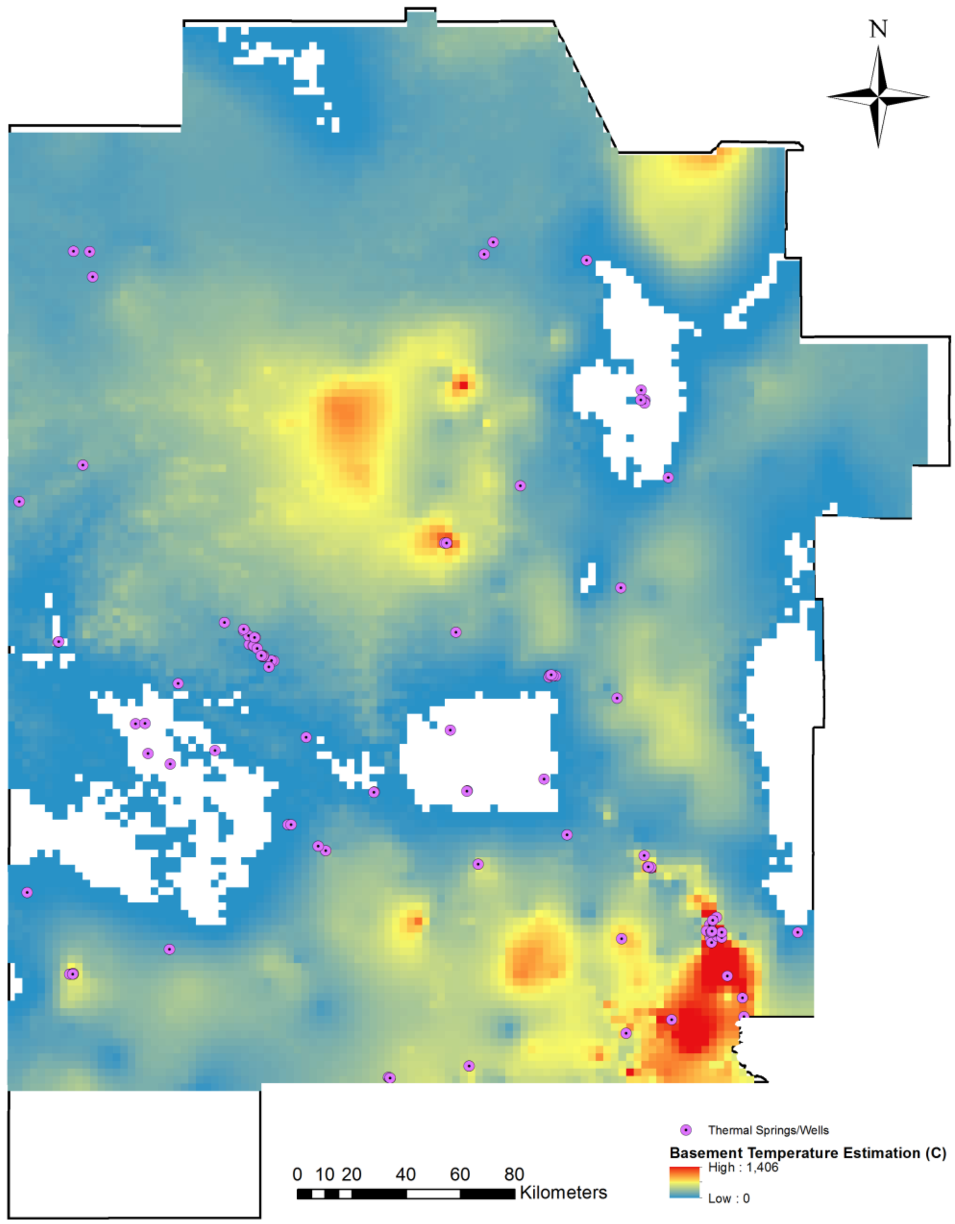

Figure 2-43: Basement Temperature in Our Study Region.

2.5.3.7 Water Table Gradient

Substantial changes in the water table elevation (Section 2.2.8) where there are not similar changes in the topography suggest that water is being displaced to/from another area. For the prospectivity map, the minimum value of the water table gradient was subtracted from the water table gradient, and then divided by the maximum value so that all regions received a prospectivity value between 0 and 1.

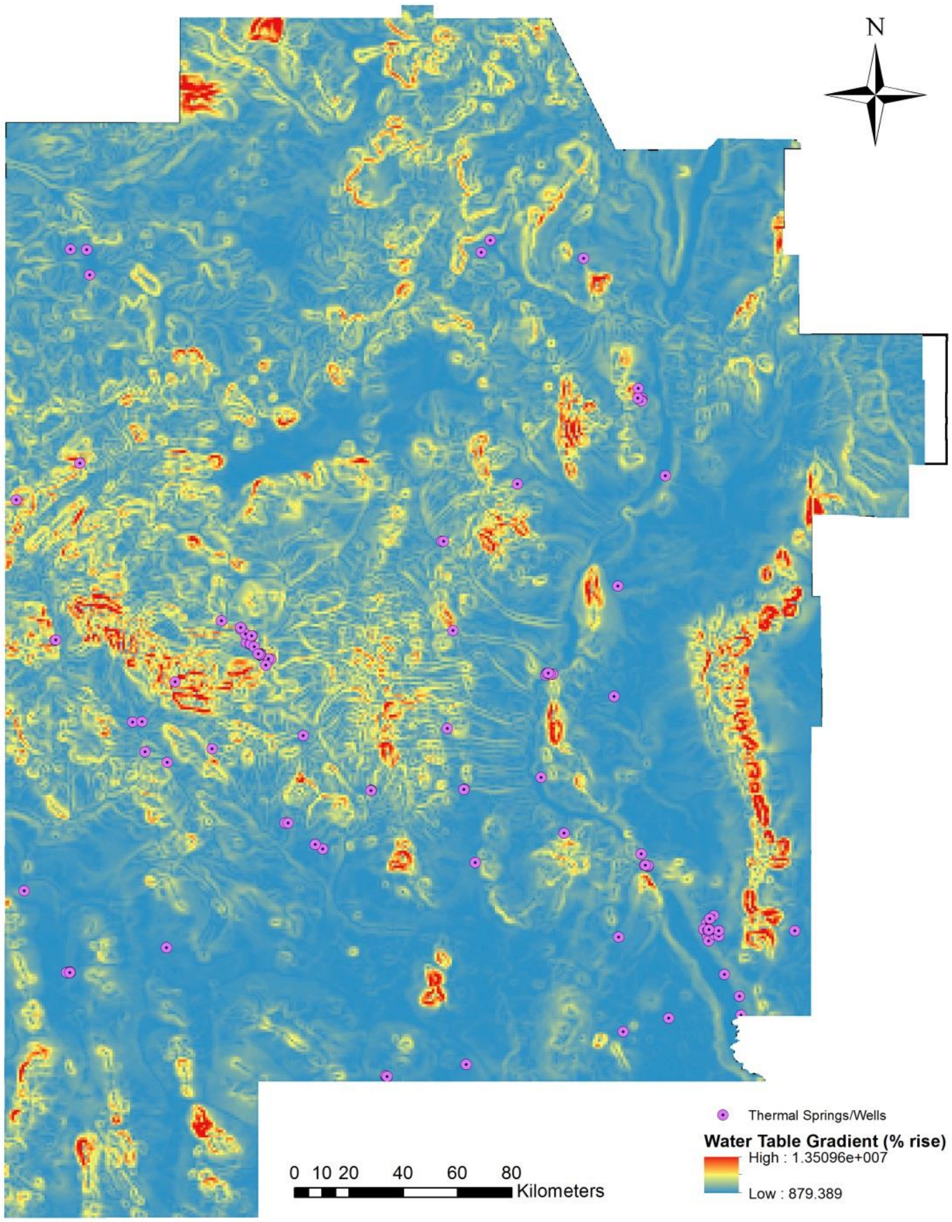

Figure 2-44: The Gradient in the Water Table within Our Study Region.

Theoretically, hydrogeologic windows can only exist in a subcrop and in a discharge zone, and thus the absence of at least one of these two signatures suggests that a hydrogeologic window cannot exist (Figure 2-45). In the prospectivity calculation the values for the subcrop map and for the recharge/discharge zones were multiplied across all other layers, so that only regions where both signatures are present receive prospectivity values.

2.5.3.8 Subcrops

The subcrop map identifies which regions could not contain a hydrogeologic window, based on the presence of different types of rocks in the subsurface (Section 2.2.6). Regions inside the subcrop were assigned a prospectivity value of 1, and regions outside of the subcrop were assigned a prospectivity value of 0.

2.5.3.9 Recharge and Discharge Zones

Recharge zones are the regions where water can enter the water table and flow into a hydrogeologic window. Discharge zones are regions where that water could be discharged from a hydrogeologic window (Section 2.2.7). Discharge zones were assigned a prospectivity value of one, whereas recharge zones were assigned a prospectivity value of zero.

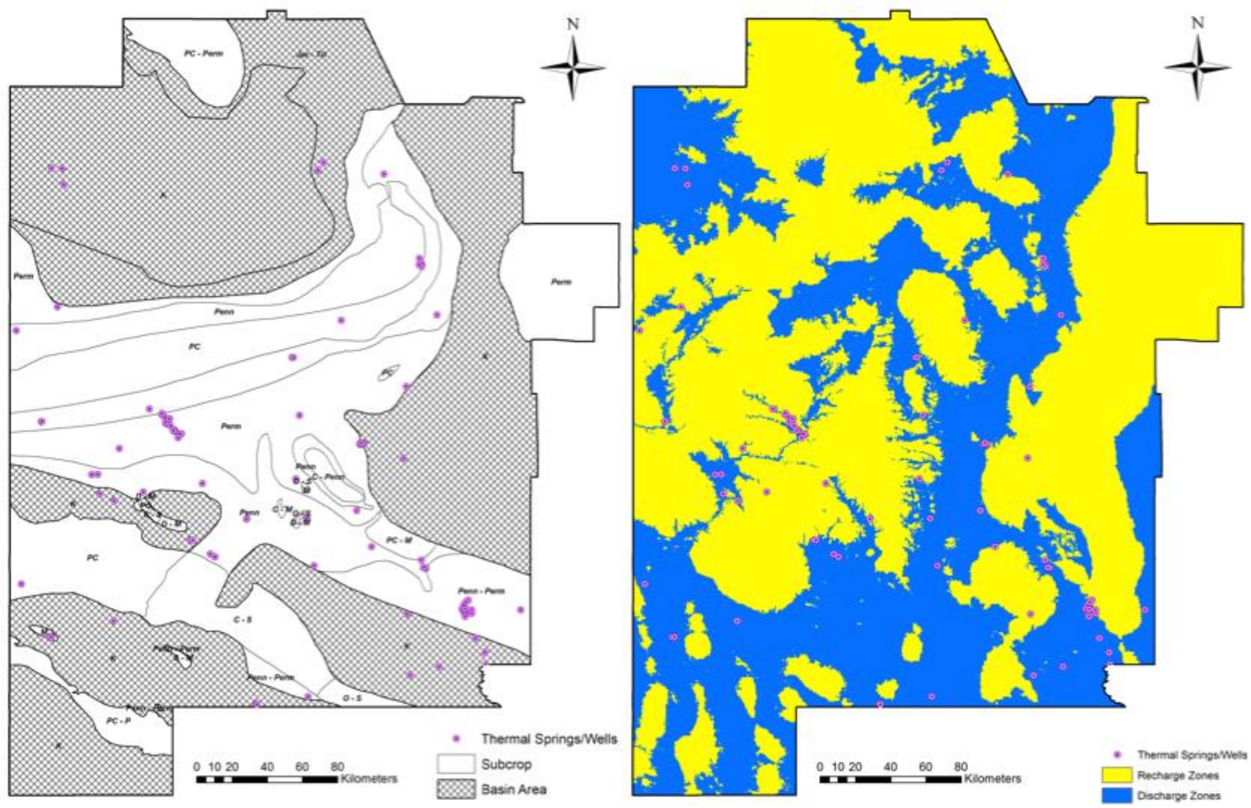

Figure 2-45: Exclusionary Signatures: Subcrop Map (left) and Recharge / Discharge Zones (right).

2.5.4 Data Availability

Mapping efforts intended to identify potential geothermal prospects will be limited by the locations of data that are available, and the information that having data conveys. For example, data on subsurface temperatures could presumably be acquired for anywhere in the study region, but borehole temperature measurements are limited to locations where wells have been drilled. The predictive capability of an analysis will be limited by the amount, location, and types of data that are used. In this subsection, we present the Construction of a Data Availability map which, when used in conjunction with the prospectivity map, identifies the degree to which locations may contain geothermal resources, as well as the confidence that can be placed in that assessment.

To create the Data Availability map, we conducted a data density analysis on each of the different types of observations from wells (e.g., heat flow, basement temperature, lithium, boron, and water table). We did not conduct a data density analysis on signatures that are observed on regional basis (e.g., faults, inferred faults, earthquakes), because the absence of a fault or earthquake, for example, does not represent a lack of data for any particular location. Each data density analysis uses a search radius of ½ the standard distance. The standard distance gives an indication of the dispersion of the data, which can be considered a complementary measure to data density (Bachi, 1962). The standard distance is:

$$SD = \sqrt{\frac{\sum_{i=1}^{n}(x_i - \bar{x})^2}{n} + \frac{\sum_{i=1}^{n}(y_i - \bar{y})^2}{n}}$$

where $(\bar{x}, \bar{y})$ is the mean center of the data and (x_i, y_i) are the coordinates of the i^{th} point. One data density analysis was conducted for each applicable signature, using only the points for that signature. The result of each data density analysis was normalized so that the maximum value was set to one, and the rest of the values were scaled linearly between 0 and 1. The normalized data density analyses were summed to produce one map in order for data on each signature to contribute equally to the Data Availability Map. This Data Availability map is shown in Figure 2-46.

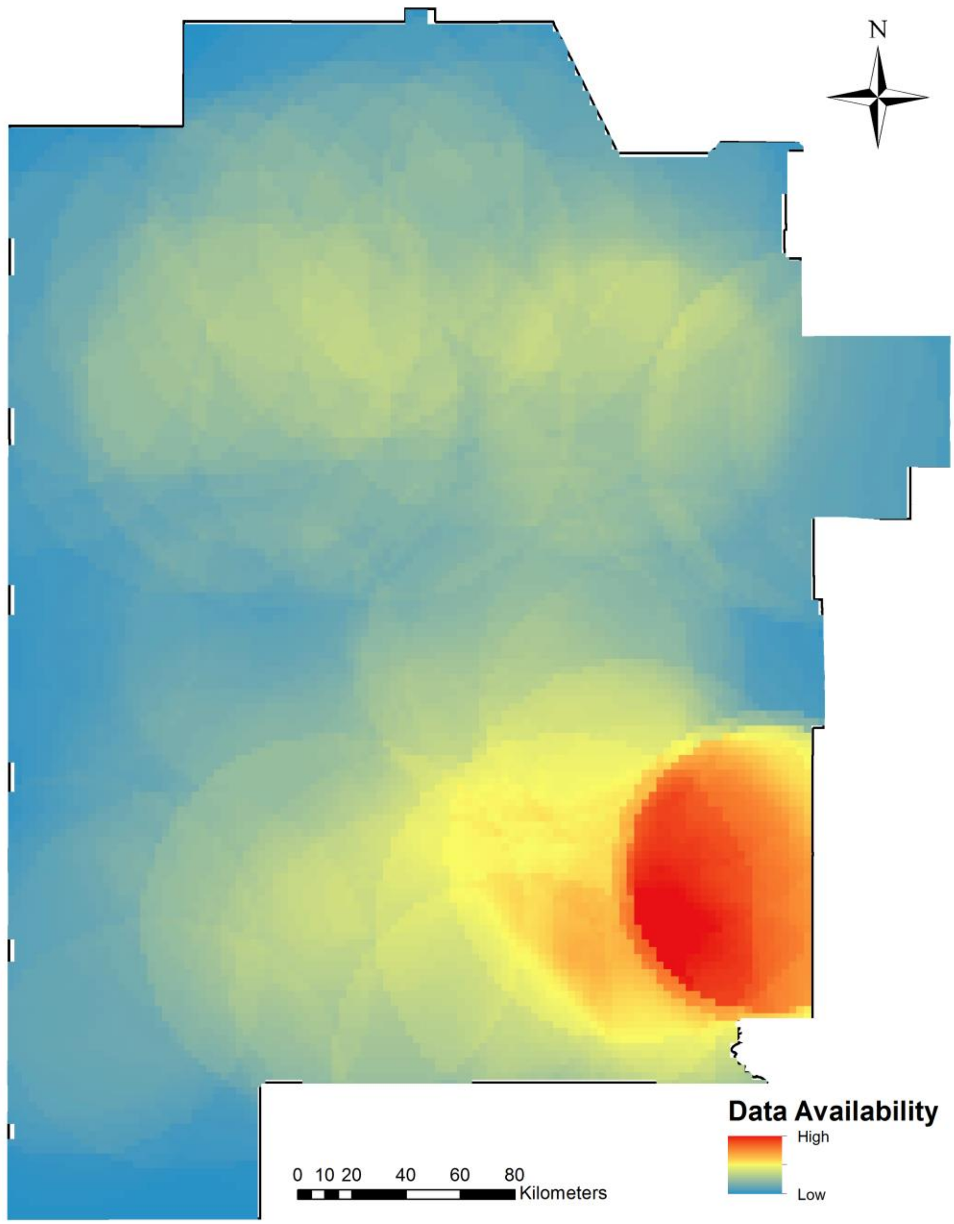

Figure 2-46: Density Plot of Data Used in the Prospectivity Analysis.

The Data Availability map shows that the southeast corner of our study area has the most data. As a consequence, the prospectivity values in this region could be considered to be the most robust, and areas with high prospectivity values in these regions are likely to be good targets for further investigation and analysis of geothermal potential. In contrast, areas that have high prospectivity values in regions with lower data density could be good targets for further data collection to clarify uncertainties regarding their potential for containing geothermal resources. Both of these conditions were considered in the selection of target locations for Phase II research.

Section 3. References

Ander,M, . E., R. Goss, and D. W. Strangway, 1984, Detailed magnetotelluric/ audiomagnetotellurics study of the Jemez volcanic zone, New Mexico, J. Geophys. Res., 89, 3335-3353, 1984.

Arehart, G. B. and Donelick, R. A., 2006. “Thermal and isotopic profiling of the Pipeline hydrothermal system: Application to exploration for Carlin-type gold deposits.” Journal of Geochemical Exploration, v. 91, p. 27-40.

Arehart, G. B. and Donelick, R. A., 2006. “Thermal and isotopic profiling of the Pipeline hydrothermal system: Application to exploration for Carlin-type gold deposits.” Journal of Geochemical Exploration, v. 91, p. 27-40.

Bachi, R. (1962). Standard Distance Measures and Related Methods for Spatial Analysis. *Regional Science Association*, *10*, 83–132.

Baldwin, J.A., and Anderholm, S.K., 1992. Hydrogeology and ground-water chemistry of the San Andres-Glorieta aquifer in the Acoma Embayment and eastern Zuni Uplift, West-Central New Mexico. U.S. Geological Survey Water-Resources Investigations Report 91-4033.

Barroll, M. W., and M. Reiter, Analysis of the Socorro hydrogeothermal system: Central New Mexico, J. Geophys. Res., 95, v. 21,949-21,963, 1990.

Bear, J. (2013). Dynamics of fluids in porous media. Courier Corporation.

Beardsmore, G.R. and J.P. Cull, 2001, Crustal Heat Flow. A Guide to Measurement and Modelling, Cambridge University Press, 319 p.

Ben-Haim, Yakov. Information-gap decision theory: decisions under severe uncertainty. Academic Press, 2001.

Bucker, C., and L. Rybach, 1996, A simple method to determine heat production from gamma logs: Marine and Petroleum Geology, v.13 (4), p. 373-375.

Butler, J.J., Jr., and X. Zhan, Hydraulic tests in highly permeable aquifers, Water Resour. Res., v. 40, W12402, doi:10.1029/2003WR002998, 2004.

Caldwell, T.G., Bibby, H.M. and Brown, C. (2004). The Magnetotelluric Phase Tensor. Geophys J. Int. 158, 457-469.

Callender, J. F. and R. E. Zilinski, Jr., 11Kinematics of Tertiary and Quaternary Deformation Along the Eastern Edge of the Lucero Uplift, Central New Mexico, 11 N.M. Geol. Soc. Spec. Pub.~' 53-61 (1976).

Carranza, E. J. M., Wibowo, H., Barritt, S. D., & Sumintadireja, P. (2008). Spatial data analysis and integration for regional-scale geothermal potential mapping, West Java, Indonesia. Geothermics, 37(3), 267–299. doi:10.1016/j.geothermics.2008.03.003

Chapin, C. E., Chamberlin, R. M., Osburn, G. R., White, D. W., & Sanford, A. R. (1978). Exploration framework of the Socorro geothermal area, New Mexico.Field guide to selected cauldrons and mining districts of the Datil–Mogollon volcanic field, New Mexico: New Mexico Geological Society, Special Publication, 7, 115-129.

Chave, A.D. and Jones, A.G. (2012) The Magnetotelluric Method, Theory and Practice. Cambridge University Press.

Clemons, R.E., 1984, Geology of Capitol Dome quadrangle, Luna County, New Mexico: New Mexico Bureau of Mines and Mineral Resources Geologic Map 56, 1 sheet, scale 1:24,000.

Coolbaugh MF, Arehart GB, Faulds JE, Garside LJ (2005) Geothermal systems in the Great Basin, western United States: modern analogues to the roles of magmatism, structure, and regional tectonics in the formation of gold deposits. In: Geological Society of Nevada Symposium 2005: Window to the World (eds Rhoden HN, Steininger RC, Vikre PG), pp. 1063–82. Nevada Geological Society, Reno, NV.

Coolbaugh, M., Kratt, C., Faulds, J., Zehner, R., and Sladek, C., 2013, Active geothermal systems of the Mina Deflection, southwestern Nevada, in L.J. Garside, ed., Geothermal and Petroleum

Developments in Several Extensional Basins of the Central Walker Lane, Nevada: 2013 Nevada Petroleum and Geothermal Society Field Trip Guidebook, Oct. 12-13, 2013, p. 101-116.

Cooper, H. and CE Jacob, 1946, A tereralized graphical method for evaluatin formation constants and summarizing well field history, Trans. Of Am. Geophy. Union, v. 29, p. 526-534.

Cron, B., 2011, “Geochemical characteristics and microbial diversity of CO2-rich mound springs of the Tierra Amarilla anticline, New Mexico.” University of New Mexico M.S. thesis, 122 pp.

Daniel H. Koning, Andrew P. Jochems, Shari A. Kelley, Virginia T. McLemore, and Colin T. Cikoski, 2014, Geologic map of the Monticello 7.5-Minute Quadrangle, Sierra and Socorro Counties, New Mexico New mexico Bureau of Geology and Mineral Resources,Open-file Geologic Map – 245: 1:24000.

Deer W.A., Howie R.A., and Zussman J., 1992. “An Introduction to the Rock-forming Minerals.” Essex: Longman Scientific and Technical; New York: Wiley, 2nd edition, ISBN 0470218096, 696pp.

Dixon, P. M., El-shaarawi, A. H., & Piegorsch, W. W. (2002). Ripley’s K function. Encyclopedia of Environmetrics, 3, 1796–1803. Retrieved from http://www.biostat.umn.edu/~dipankar/pubh8472/RipleysK.pdf

Eakin, T. E. 1966, A regional interbasin groun-water system in the Wite River Area, southeastern Nevada, Water Resources Research, v. 2(2), p. 251-271.

Faulder, D. D., S. D. Johnson, and W. R. Benoit. Flow and permeability structure of the Beowawe, Nevada hydrothermal system. No. INEL/CON--97-00017; CONF-970114--3. Lockheed Idaho Technologies Co., Idaho Falls, ID (United States), 1997.

Faulds, J.E., Coolbaugh, M.F., Hinz, N.H., Cashman, P.H., Kratt, C., Dering, G., Edwards, J., Mayhew, B., and McLachlan, H., 2011, Assessment of favorable structural settings of geothermal systems in the Great Basin, western USA: Geothermal Resources Council Transactions, v. 35, p.777-784.

Ferguson, G., & Grasby, S. E. (2011). Thermal springs and heat flow in North America. Geofluids, 11(3), 294-301.

Fialko, Y., and Pearse, J., 2012, Sombrero uplift above the Antiplano-Puna Magma Body: Evidence of a Ballooning Mid Crustal Diapir, Science, v. 338, no. 6104, p. 250-252.

Fialko, Y., and Simons, M., 2001, Evidence for on-going inflation of the Socorro magma body, New Mexico, from Interferometric Synthetic Aperture Radar imaging, Geophysical Research Letters, v. 28, p. 3549–3552.

Fialko, Y., Simons, M., and Khazan, Y., 2001, Finite source modeling of magmatic unrest in Socorro, New Mexico, and Long Valley, California, Geophysical Journal International, v. 146, p. 191-200.

Finnell, T.L., 1987, Geologic map of the Cliff quadrangle, Grant County, New Mexico, U. S. Geological Survey, Miscellaneous Investigations Series Map 1-1768.

Forster C, Smith L (1989) The influence of groundwater flow on thermal regimes in mountainous terrain: a model study. Journal of Geophysical Research, 94, 9439–51.

Fournier, R. O., 1981, Application of water geochemistry to geothermal exploration and reservoir engineering, in Rybach, L., and Muffler, L. J. P., eds, Geothermal Systems: Principles and Case Histories: John Wiley & Sons, New York , p. 109 – 143.

Fournier, R.O., 1977, Chemical geothermometers and mixing models for geothermal systems: Geothermics, v. 5, p. 51 – 50.

Frenzel, P.P., 1992, Simulation of ground-water flow in the San Andres-Glorieta aquifer in the Acoma embayment and eastern Zuni uplift, west central New Mexico: U.S. Geological Survey Water-Resources Investigations Report 91-4099, 381 p.

Fuge, R., 1988. "Sources of halogens in the environment, influences on human and animal health." Environmental Geochemistry and Health, v. 10, p. 51-61.

Gilmer, A., Mauldin, R., and Keller, G. 1986, A gravity study of the Jornado Del Muerto and Palomas Basins: New Mexico Geological Society Guidebook, 37th Field Conference, p. 131-134.

Goff, F. McCormack, T. Gardner, J, Trujillo P, Couce, D., Vidale, R, and Charles R. (1983) Water geochemistry of the Lucero Uplift, New Mexico: geothermal investigation of low-temperature mineralized fluids. No. LA-9738-OBES. Los Alamos National Lab., NM (USA).

Goode, D. J. (1996). Direct simulation of groundwater age. Water Resources Research, 32(2), 289-296.

Grew, E. S., 1996. “Borosilicates (exclusive of tourmaline) and Boron in Rock-forming Minerals in Metamorphic Environments”, in Grew, E. S. and Anovitz, L. M., eds. Boron: Mineralogy, Petrology and Geochemistry. Reviews in Mineralogy, Mineralogical Society of America. v. 33, p. 387-502.

Harder, V., Morgan, P., and Swanberg, C.A., 1980, Geothermal resources in the Rio Grande rift: Origins and potential, Geothermal Resources Council, Transactions, v. 4, p. 61-64.

Harp, Dylan R., and Velimir V. Vesselinov. "Contaminant remediation decision analysis using information gap theory." Stochastic Environmental Research and Risk Assessment 27.1 (2013): 159-168.

Hem, J. D., 1985. "Study and interpretation of the chemical characteristics of natural water." U.S. Geological Survey Water-Supply Paper 2254.

Hogan, J.F., Phillips, F.M., Mills, S.K., Hendrickx, J.M.H., Ruiz, J., Chesley, J.T., Asmerom,Y., 2007. Geologic origins of salinization in a semi-arid river: the role of sedimentary basin brines. Geology 35, 1063–1066.

Hohmann, G.W. and G.R. Jiracek, 1979, Bipole-dipole interpretation with three-dimensional models (Including field study of Las Alturas, New Mexico), Earth Science Lab., Univ. of Utah Research Inst., Salt Lake City, Utah, DOE/ET/28392-29, 78-1701.b.3.2.2, ESL 20, 20 p.

Howald T, Person M, Campbell A, Lueth V, Hofstra A, Sweetkind D, Gable CW, Banerjee A, Luijendijk E, Crossey L, Karlstrom K, Kelley S, and Phillips F, 2014. Evidence for Long-Time Scale (> 10^3 years) Changes in Hydrothermal Activity Induced by Seismic Events, Geofluids, doi: 10.1111/gfl.12113.

Jiracek, G.R. and M. Mahoney, 1981, Electrical resistivity investigation of the geothermal potential of the Truth or Consequences, New Mexico area; in New Mexico/DOE State-Coupled Low Temperature Resource Assessment Program, Fiscal Year 1980, Final Technical Report, U.S. Dept. of Energy, Sec. 2, Chap. 7, p.1-16

Jiracek, G.R., C. Smith, M.E. Ander, H.T. Holcombe, M.T. Gerety, and C.A. Swanberg, 1977, Geophysical studies at Lightning Dock KGRA, Hidalgo County, New Mexico, Geothermal Resource Council, Trans., 1, 157-158.

Jiracek, G.R., E.P. Gustafson, and P.S. Mitchell, 1983, Magnetotelluric results opposing magma origin of crustal conductors in the Rio Grande rift, Tectonophysics, 94, 299-326.

Jochems, A. P., Kelley, S. A., Seager, W. R., Cikoski, C. T., and Koning, D. J., 2014,Geologic map of the Hillsboro 7.5-Minute Quadrangle, Sierra County, New Mexico, New Mexico Bureau of Geology and Mineral Resources OF-GM-242, Scale 1:24,000.

Karra, S. and Kitay, C., PyFLOTRAN documentation release 1.0.0, Tech. Rep. LA-UR-15-21189, Los Alamos National Laboratory (2015).

Kennedy, B.M. and van Soest, M.C., 2007, Flow of mantle fluids through the ductile lower crust: Helium isotope trends, Science, v. 318, p. 1433-1436.

Larsen, S., and Reilinger, R., 1983, Recent measurements of crustal deformation related to the Socorro magma body, New Mexico: New Mexico Geological Society Guidebook, 34th Field Conference, p. 119-121.

Lawton, T.F., 2000, Inversion of Late Jurassic-Early Cretaceous extensional faults of the Bisbee Basin, southeastern Arizona and southwestern New Mexico: New Mexico Geological Society Guidebook, 51st Fall Field Conference, p. 95-102.

Lichtner, P.C., Hammond, G.E., Lu, C., Karra, S., Bisht, G., Andre, B., Mills, R.T., Kumar, J., PFLOTRAN user manual: A massively parallel reactive flow and transport model for describing surface and subsurface processes, Tech. rep., Report No.: LA-UR-15-20403, Los Alamos National Laboratory (2015)

Lohse, R. L., and Schoenmackers, R. 1985,Geothermal low-temperature reservoir assessment in northern Dona Ana County, New Mexico: New Mexico Research and Development Institute Re2ort NMERDI 2-71 -4220, Lozinsky, R. P., 1987, Cross section across the Jornada del Muerto, Engle, and Northern Palomas Basins, south-central New Mexico: New Mexico Geology 9(3) 55– 57.

Machette, M. N., Personius, S. F., Kelson, K. I., Haller, K. M., and Dart, R. L., 1998, Map and data for Quaternary faults and folds in New Mexico: Open-File Report98-521b, 358 pp.

Machette, M.N., 1987, Preliminary assessment of Quaternary faulting near Truth or Consequences, New Mexico: U.S. Geological Survey Open-File Report 87-652, 40 p.

Mack, G.H., Nightengale, A.L., Seager, W.R., and Clemons, R.E., 1994a, The Oligocene Goodsight-Cedar Hills half-graben near Las Cruces and its implication to the evolution of the Mogollon-Datil volcanic field and to the southern Rio Grande rift: New Mexico Geological Society, Guidebook 45, p. 135-142.

Mack, G.H., Seager, W.R., and Kieling, J., 1994b, Late Oligocene and Miocene faulting and sedimentation, and evolution of the southern Rio Grande rift, New Mexico: Sedimentary Geology, v. 92, p. 79-96.

Mack, G.H., and Stout, D.A., 2005, Unconventional distribution of facies in a continental rift basin: The Pliocene-Pleistocene Mangas Basin, south-western New Mexico, USA: Sedimentology, v. 52, p. 1187-1205.

Mailloux, B., Person, M., Strayer, P., Hudleston, P.J., Cather, S., Dunbar, N., 1999, Tectonic and Stratigraphic Controls on the Hydrothermal Evolution of the Rio Grande Rift, Water Resources Research, v. 35(9), p. 2641-2659.

McKenna, Jason R., and David D. Blackwell. "Numerical modeling of transient Basin and Range extensional geothermal systems." Geothermics 33, no. 4 (2004): 457-476.

McClenaghan, M. and Kjarsgaard, B., 2001, Indicator mineral and geochemical methods for diamond exploration in glaciated terrain in Canada, Geological Society, London, Special Publications 2001, v. 185, p. 83-123

McCraw, D. J., and Williams, S. F., 2012, Terrace stratigraphy and soil chronosequence of Cañada Alamosa, Sierra and Socorro Counties, New Mexico: New Mexico Geological Society, 63rd Annual Field Conference Guidebook, p. 475-489.

Mexico Bureau of Mines and Mineral Resources Bulletin 101, 42 p.

Minerals.” Essex: Longman Scientific and Technical; New York: Wiley, 2nd edition, ISBN 0470218096, 696pp.

Morgan, Paul, and James C. Witcher, 2011, Geothermal resources along the southern Rocky Mountains and the Rio Grande Rift. The Mountain Geologist, v. 48, no. 4, p. 81-94.

Morgan, P., Harder, V., Swanberg, C.A., and Dagget, P.H., 1981, A ground-water convection model for Rio Grande rift geothermal resources, Geothermal Resources Council, Transactions, v. 5, p. 193-196.

Owens, L. B., 2013, “Geochemical investigation of hydrothermal and volcanic systems in Iceland, New Mexico and Antarctica.” New Mexico Institute of Mining & Technology, Ph.D. dissertation.

Pearse, J., and Fialko, Y., 2010, Mechanics of active magmatic intraplating in the Rio Grande Rift near Socorro, New Mexico, Journal of Geophysical Research, v. 115, B07413, 16 p.

Pepin J, Person M, Phillips F, Kelley S, Timmons S, Witcher J, and Gable C, 2014, Deep Fluid Circulation within Crystalline Basement Rocks and the Role of Hydrogeologic Windows in the Formation of the Truth or Consequences, New Mexico Low-Temperature Geothermal System, Geofluids, doi: 10.1111/gfl.12111.

Pepin, J., Person, M., Phillips, F., Kelley, S., Timmons S. , Owens, L., Witcher, J., Gable C.,2015, “Deep fluid circulation within crystalline basement rocks and the role of hydrogeologic windows in the formation of the Truth or Consequences, New Mexico low-temperature geothermal system.” Geofluids, v. 15, p. 139–160, DOI: 10.1111/gfl.12111.

Person M. , Hofstra, A., Sweetkind, D, Stone, W., Cohen, D., Gable, C, Banerjee, A. 2012, Analytical and numerical models of hydrothermal fluid flow at fault intersections, Geofluids, v. 12, 312–326.

Pollock, D. W. 1994, "User’s guide for MODPATH/MODPATHPLOT: a particle-tracking post-processing package for MODFLOW." U.S. Geological Survey Open-File Reports 94-464.

Poux, B., & Suemnicht, G. (2012). Use of GIS geoprocessing to select the most favorable sites for geothermal exploration in Oregon. In *Transactions - Geothermal Resources Council* (Vol. 36 2, pp. 745–750). Retrieved from http://www.scopus.com/inward/record.url?eid=2-s2.0-84876254349&partnerID=40&md5=c1e7725d3559100797a905e27b79ecc5

Reiter M, Eggleston R, Broadwell B, Minier J (1986) Estimates of terrestrial heat flow from deep petroleum tests along the Rio Grande Rift in Central and Southern New Mexico. Journal of Geophysical Research, 91, 6225–45.

Ross, H. P., and Witcher, J. C., 1992, Self-potential expression of hydrothermal resources in the southern Rio Grande rift, New Mexico: Transactions, Geothermal Resources Council, v. 16, p. 247-253.

Ross, H. P., and Witcher, J. C., 1998, Self-potential surveys of three geothermal areas in the southern Rio Grande rift, New Mexico: New Mexico Geological Society 49th Annual field Conference Guidebook, p. 93-100.

Sanford RM, Bowers RL, Combs J (1979) Rio Grande Rift geothermal exploration case history, Elephant Butte prospect, south-central New Mexico. Transactions, Geothermal Resources Council, 3, 609–12.

Sass JH, Lachenbruch AH, Munroe RJ, Green GW, Moses TH Jr (1971) Heat flow in the western United States. Journal of Geophysical Research, 76, 6356–431.

Seager, W. R., 1986, Third-day road log, from Truth or Consequences to southeastern Caballo Mountains and San Diego mountain via I-25and the Jornada Del Muerto, in Clemons, R. E., King, W. E., and Mack, G. H., eds., Truth or Consequences Region: New Mexico Geological Society 37th Annual Field Conference Guidebook, p. 35-52.

Seager, W. R., and Hawley, J. W., 1973, Geology of Rincon Quadrangle, New Mexico: New Mexico Bureau of Mines and Mineral Resources Bulletin 101, 42 p.

Seager, W. R.; Hawley, J. W.; Kottlowski, F. E.; Kelley, S. A., 1987,Geology of East Half of Las Cruces and Northeast El Paso 1 degree by 2 degree Sheets, New Mexico, GM-57

Seager, W.R., and Mack, G.H., 1991, Geology of Garfield quadrangle, Sierra and Doña Ana Counties, New Mexico: New Mexico Bureau of Mines and Mineral Resources Bulletin 128, 2 pls., scale 1:24,000.

Seager, W.R., and Mack, G.H., 2005, Geology of the Caballo and Apache Gap quadrangles, Sierra County, New Mexico: New Mexico Bureau of Geology and Mineral Resources Geologic Map 74, scale 1:24,000.

Skotnicki, S.J., 2011, Geologic map of the Circle Mesa quadrangle, Grant County, New Mexico: New Mexico Bureau of Geology and Mineral Resources Open-file Digital Geologic Map OF-GM 225; 1:24000.

Skotnicki, S.J., 2011, Geologic map of the Circle Mesa quadrangle, Grant County, New Mexico: New Mexico Bureau of Geology and Mineral Resources Open-file Digital Geologic Map OF-GM 225; 1:24000.

Smith L, and Chapman D. S.,1983, On the thermal effects of groundwater flow: 1. Regional scale systems: Journal of Geophysical Research, 88, B1, 593–608.

Summers, W.K., 1976, Catalog of thermal waters in New Mexico: New Mexico Bureau of Mines and Mineral Resources Hydrogeologic Report 4, 80 p.

Theis CV, Taylor GC, Murray CR (1941) Thermal waters of the Hot Springs Artesian Basin, Sierra County, NM. Fourteenth and Fifteenth Biennial Reports of the State Engineer of New Mexico, 1938–1942, 421–92.

Trauger, F.D., 1972, Water Resources and General Geology of Grant County, New Mexico; Hydrologic Report 2, New Mexico Bureau of Mines and Mineral Resources, 211 p.

Vice, G. S., Faulds, J. E., Ehni, W. J., & Coolbaugh, M. F. (2007). Structural controls of a blind geothermal system in the northern Pyramid Lake area, northwestern Nevada. Geothermal Resources Council Transactions, 31, 133-137.

Wahl, D. E., 1980, Mid-Tertiary volcanic geology in parts of Greenlee County, Arizona and Grant County, New Mexico (Ph.D. dissertation): Tempe, Arizona State University, 144 p.

Waller, L. A., & Gotway, C. A. (2004). Applied Spatial Statistics for Public Health Data. Hoboken, N.J.: John Wiley & Sons.

Wargo, J.G., 1959, Geology of the Schoolhouse Mountain quadrangle, Grant County, New Mexico: Tucson, University of Arizona, unpublished Ph. D. dissertation, 187 p.

Welch, Alan H., Daniel J. Bright, and Lari A. Knochenmus. "Water resources of the Basin and Range carbonate-rock aquifer system, White Pine County, Nevada, and adjacent areas in Nevada and Utah." US Geological Survey Scientific Investigations Report 5261 (2007): 96.

Williams, A.J., Crossey, L.J., Karlstrom, K.E., Newell, D., Person, M., Woosley, E., 2013. “Hydrogeochemistry of the Middle Rio Grande aquifer system - fluid mixing and salinization of the Rio Grande due to fault inputs.” Chemical Geology, v. 351, p.281-298.

Witcher, J. C. (1991). The Rincon geothermal system, southern Rio Grande rift, New Mexico; a preliminary report on a recent discovery. Geothermal Resources Council, Transactions, 15, 205-212.

Witcher, J. C., & Lund, J. W. (2002b). Gila Hot Springs. Geo-Heat Cent Q Bull, v 23, p. 25-29.

Witcher, J. C., 1988, Geothermal resources of southwestern New Mexico and Southeastern Arizona: New Mexico Geological Society, 39th Field Conference Guidebook, Southwestern New Mexico, p. 191-197.

Witcher, J. C., 1991a, Radon soil-gas surveys with diffusion-model corrections in geothermal exploration: Transactions, Geothermal Resources Council, v. 15, p. 301-308.

Witcher, J. C., 1991b, The Rincon geothermal system, southern Rio Grande rift, New Mexico: a preliminary report on a recent discovery: Transactions, Geothermal Resources Council, v. 15, p. 205-212.

Witcher, J. C., 1998, The Rincon SLH1 geothermal well, in 3rd day road logs, New Mexico Geological Society 49th Annual field Conference Guidebook, p. 35-38.

Witcher, James C. "Geothermal direct-use well for commercial greenhouses radium springs, New Mexico." GHC Bulletin, December (2001): 1-7.

Witcher, James C. "The Rincon geothermal system, southern Rio Grande rift, New Mexico; a preliminary report on a recent discovery." Geothermal Resources Council, Transactions 15 (1991): 205-212.

Witcher, James C., and R. A. Cunniff. (2002a): "Geothermal energy at New Mexico State University in Las Cruces." GHC Bull v. 12 p. 30-36.

Section 4. Appendix A (Bios)

Richard S. Middleton
Los Alamos National Laboratory, Earth and Environmental Sciences, Los Alamos NM, 87545
Phone: 505-665-8332; Email: rsm@lanl.gov

EDUCATION:

2006	Ph.D., University of California, Santa Barbara (Geography and Operations Research)
1999	M.S., University of Leicester, Geographical Information Science
1996	B.S., Lancaster University, Geography

PROFESSIONAL EXPERIENCE:

- ***Los Alamos National Laboratory (2009-present)***, Research Scientist, Earth and Environmental Sciences,
  CO_2 capture and storage (CCS), wind energy and transmission modeling, biofuels and optimal watershed design, basin-scale energy development (climate-land-energy-water), spent nuclear fuel transportation and storage optimization, advanced small modular reactor (aSMR) siting, water-energy-carbon modeling for oil shale and oil sands development
- ***Oak Ridge National Laboratory (2007-2009)***, Research Scientist, Computational Sciences and Engineering/Energy and Transportation Sciences
  Project lead for next generation supply chain optimization and management, biofuels infrastructure modeling, geospatial data modeling and visualization, transportation
- ***Los Alamos National Laboratory (2006-2007)***, Postdoctoral Researcher, Earth and Environmental Sciences
  Water management and reservoir optimization for in situ oil shale development, GIS and infiltration modeling, CCS model development, geospatial decision making
- ***University of California, Santa Barbara (2003)***, Guest Lecturer, Teaching/Research Asst Dept of Geography

RELEVANT PUBLICATIONS:

- **Middleton, R. S.**; Levine, J. S.; Bielicki, J. M.; Viswanathan, H. S.; Carey, J. W.; Stauffer, P. H., Jumpstarting commercial-scale CO_2 capture and storage with ethylene production and enhanced oil recovery in the U.S. Gulf. Greenhouse Gases: Science and Technology 2015, In press.
- **Middleton, R. S.**; Carey, J. W.; Currier, R. P.; Hyman, J. D.; Kang, Q.; Karra, S.; Jiménez-Martínez, J.; Porter, M. L.; Viswanathan, H. S., Shale gas and non-aqueous fracturing fluids: Opportunities and challenges for supercritical CO 2. Applied Energy 2015, 147, 500-509.
- Dai, Z., **Middleton, R.S.**, Viswanathan, H., Fessenden-Rahn, J., Bauman, J., Pawar, R., Lee, S.-Y., McPherson, B. (2014) An Integrated framework for optimizing CO_2 sequestration and enhanced oil recovery, *Environmental Sciences and Technology Letters*, DOI 10.1021/ez4001033.
- **Middleton, R.S.** and Eccles, J.K., (2013). Fracking, renewables, and natural gas power: the complex future of carbon capture and storage, *Applied Energy 108*, 66-73.
- **Middleton, R.S.** and Bielicki, J.M. (2009). A scalable infrastructure model for carbon capture and storage: *SimCCS*, *Energy Policy* 37, 1052-1060.
- **Middleton, R.S.** and Brandt, A.R., (2013). Using infrastructure optimization to reduce greenhouse gas emissions from oil sands extraction and processing, *Environmental Science and Technology 47*, 1735-1744.
- **Middleton, R.S.**, Keating, G.N., Stauffer, P.H., Jordan, A.B., Viswanathan, H.S., Kang, Q., Sullivan, E.J., Chu, S.P., Carey, J.W., Mulkey, M.L., Esposito, R.A., Meckel, T.A. (2012). The cross-scale science of CO_2 capture and storage: from pore scale to regional scale, *Energy and Environmental Science 5*, 7328-7345.x
- Phillips, B., and **Middleton, R.S.** (2012). *SimWIND*: A Geospatial Infrastructure Model for Optimizing Wind Power Generation and Transmission, *Energy Policy* 43, 291–302.
- **Middleton, R.S.**, Keating, G.N., Stauffer, P.H., Viswanathan, H.S., & Pawar, R.J. (2012). The effect of geologic reservoir uncertainty on CCS infrastructure, *International Journal of Greenhouse Gas Control* 8, 132-142.
- **Middleton, R.S.** (2013). A new optimization approach to energy network modeling: anthropogenic CO_2 capture coupled with enhanced oil recovery, *International Journal of Energy Research 37*, 1794-1810.

RELEVANT ACTIVITIES:

- Steering committee and a leading author for the energy-water-land interactions technical input report for the 2014 National Climate Assessment
- Energy-water nexus representative for Los Alamos National Laboratory

Jeffrey Bielicki
The Ohio State University, Department of Civil, Environmental, and Geodetic Engineering (CEGE), joint with The John Glenn College of Public Affairs (JGC)
(CEGE) 283b Hitchcock, 2070 Neil Avenue; (JGC) 310c Page Hall, 1810 College Road, Columbus, OH 43210
P: (614) 688-2131/2113, bielicki.2@osu.edu

Education:

2010-13	Research Associate (post-doc), University of Minnesota
2009	Ph.D., Harvard University, Public Policy (Energy, Environmental, and Science)
2003	M.P.A., Harvard University, Systems Analysis, Science and Technology Policy
2000	M.B.A., University of Chicago, Economics, Strategy, Organizational Behavior
1996	B.S., Valparaiso University, Mechanical Engineering

Positions:

2013-	Assistant Professor, The Ohio State University; (joint) Civil, Environmental, and Geodetic Engineering; John Glenn College of Public Affairs
2010-2013	Research Associate, University of Minnesota
2009-2010	Weinberg Fellow, Oak Ridge National Laboratory
2006-2009	Research Fellow, Harvard University
1993-2000	Mechanical Engineer, Fermi National Accelerator Laboratory (co-op 1993-95)

RELEVANT PUBLICATIONS:

1. Adams, B., Kuehn, T., **Bielicki, J.**, Randolph, J., and Saar, M. (2015). “A Comparison of the Electric Power Output of CO_2 Plume Geothermal (CPG) and Brine Geothermal Systems for Varying Reservoir Conditions.” *Applied Energy, 140,* 365-377. http://dx.doi.org/10.1016/j.apenergy.2014.11.043
2. Buscheck, T., **Bielicki, J.,** Chen, M., Sun, Y., Hao, Y., Edmunds, T., Saar, M., and Randolph, J. (2015). “Multi-Fluid Sedimentary Geothermal Energy Systems for Dispatchable Renewable Electricity.” *Proceedings World Geothermal Congress 2015*. Melbourne Australia, 19-25 April 2015.
3. Saar, M., Buscheck, T., Jenny, P., Garapti, N., Randolph, J., Karvounis, D., Chen, M., Sun, Y., and **Bielicki, J.** (2015). “Numerical Study of Multi-Fluid and Multi-Level Geothermal Fluid Systems.” *Proceedings World Geothermal Congress 2015.* Melbourne Australia, 19-25 April 2015.
4. **Bielicki, J.,** Peters, C., Fitts, J., and Wilson, E., (2015). “An Examination of Geologic Carbon Sequestration Policies in the Context of Leakage Potential.” *International Journal of Greenhouse Gas Control, 37,* 61-75. http://dx.doi.org/10.1016/j.ijggc.2015.02.023
5. Adams, B., Kuehn, T., **Bielicki, J.**, Randolph, J., and Saar, M, (2014). “On the Importance of the Thermosiphon Effect in CO_2 Plume Geothermal (CPG) Power Systems”. *Energy, 69*, 409-418.
6. **Bielicki, J.**, Calas, G., Ha-Duong, M., Middleton, R. (2014). “National Corridors for Climate Change Mitigation: Managing Industrial CO_2Emissions in France.” *Greenhouse Gases: Science and Technology*, *4(3),* 264-277.
7. **Bielicki, J**., Pollak, M., Fitts, J., Peters, C., and Wilson, E. (2014). “Causes and Financial Consequences of the Impacts of Leakage from Geologic CO_2 Storage Reservoirs.” *International Journal of Greenhouse Gas Control, 20,* 272-284. http://dx.doi.org/10.1016/j.ijggc.2013.10.024
8. Middleton, R., Clarens, A., Liu, X., **Bielicki, J.**, and Levine, J. (2014). “CO_2 Deserts: Implications of Existing CO_2 Supply Limitations for Carbon Management.” *Environmental Science & Technology, 48,* 11713-11720. http://dx.doi.org/10.1021/es5022685
9. Kuby, M., **Bielicki, J**., and Middleton, R. (2011). “The Optimal Spatial Deployment of CO_2 Capture and Storage with a Price on Carbon.”*International Regional Science Review, 3*, 285-305. http://dx.doi.org/10.1177/0160017610397191
10. Middleton, R., and **Bielicki, J.** (2009). “A Scaleable Infrastructure Model for Carbon Capture and Storage: *SimCCS*.” *Energy Policy, 37,* 1052-1060. http://dx.doi.org/10.1016/j.enpol.2008.09.049

CURRENT STUDENTS: (*Primary; **Committee): *Hagley, Paige;**Herak,Patrick; *Hunter, Kelsey; *Langenfeld, Julie; **Matheny, Ashley; *Ogland-Hand, Jonathan, *Patel, Iti; **Rey-Sanchez, Camilo; **Saltos, Theodore; *Sutula, Glenn; **Vines, Chante’; *Wang, Yaoping

Dylan Harp
Los Alamos National Laboratory, Earth and Environmental Sciences, Los Alamos NM, 87545
Phone: 505-667-5532; Email: dharp@lanl.gov

Education:

2009	Ph.D., University of New Mexico, Civil Engineering
2005	M.S., University of New Mexico, Civil Engineering
2004	B.S., University of New Mexico, Civil Engineering, Summa Cum Laude

Professional experience:

- ***Los Alamos National Laboratory (2012-present)***, <u>Research Scientist</u>, Earth and Environmental Sciences,
  PI for geothermal model analysis and visualization tool development, PI for development of the ASCEM Uncertainty Quantification Toolset, Task lead of geologic CO_2 sequestration wellbore integrity modeling studies, groundwater flow and contaminant transport for the NNSS site, arctic permafrost degradation modeling
- ***Los Alamos National Laboratory (2010-2012)***, <u>Postdoctoral Researcher</u>, Earth and Environmental Sciences,
  Groundwater flow and contaminant transport for the LANL site, development of performance assessment framework for high-level nuclear waste repositories
- ***Los Alamos National Laboratory (2005-2010)***, <u>Graduate Research Assistant</u>, Earth and Environmental Sciences
  Modeling of aquifers with heterogeneous properties

SELECTED PUBLICATIONS:

- **<u>Dylan R Harp</u>**, Rajesh Pawar, J William Carey, and Carl W Gable. Development of reduced order models of transient wellbore leakage at geologic carbon sequestration sites. NRAP Special Edition; International Journal of Greenhouse Gas Control. In Review
- **<u>Dylan R Harp</u>**, AL Atchley, SL Painter, ET Coon, CJ Wilson, VE Romanovsky, and JC Rowland. Effect of soil property uncertainties on permafrost thaw projections: A calibration-constrained analysis. Cryosphere Discussions. In Review.
- Amy B Jordan, Philip H Stauffer, **<u>Dylan R Harp</u>**, J William Carey, and Rajesh J Pawar. A response surface model to predict CO2 and brine leakage along cemented wellbores. International Journal of Greenhouse Gas Control, 33:27-39, 2015.
- **<u>Dylan R Harp</u>**, Philip H Stauffer, Phoolendra K Mishra, Daniel G Levitt, and Bruce A Robinson. Thermal modeling of high-level nuclear waste disposal in a salt repository. Nuclear Technology, 187(3):294-307, 2014.
- **<u>Dylan R Harp</u>** and Velimir V Vesselinov. Accounting for the influence of aquifer heterogeneity on spatial propagation of pumping drawdown. Journal of Water Resource and Hydraulic Engineering, 2(3), 2013.
- **<u>Dylan R Harp</u>** and Velimir V Vesselinov. Contaminant remediation decision analysis using information gap theory. Stochastic Environmental Research and Risk Assessment, 27(1):159–168, 2013.
- **<u>Dylan R Harp</u>** and Velimir V Vesselinov. An agent-based approach to global uncertainty and sensitivity analysis. Computers & Geosciences, 40:19–27, 2012.
- **<u>Dylan R Harp</u>** and Velimir V Vesselinov. Analysis of hydrogeological structure uncer- tainty by estimation of hydrogeological acceptance probability of geostatistical models. Advances in Water Resources, 36:64–74, 2012.
- **<u>Dylan R Harp</u>**, Zhenxue Dai, Andrew V Wolfsberg, Jasper A Vrugt, Bruce A Robinson, and Velimir V Vesselinov. Aquifer structure identification using stochastic inversion. Geophysical Research Letters, 35(8), 2008.

RELEVANT ACTIVITIES:

- Principal investigator for the New Mexico Small Business Assistance (NMSBA) Robust Analysis of Risk for Exploration and Development of Geothermal Energy (RAREDGE) software development project.

Satish Karra

Computational Earth Sciences (EES-16), Los Alamos National Laboratory, Los Alamos, NM 87545
Phone: 505-606-1894, E-mail: satkarra@lanl.gov

Education:

- Ph.D. in Mechanical Engineering, Texas A&M University, 2011.
- M.S. in Mechanical Engineering, Texas A&M University, 2007.
- B.Tech. in Mechanical Engineering, Indian Institute of Technology Madras, 2005.

Professional Experience:

- Staff Scientist, Earth and Environmental Sciences, Los Alamos National Laboratory, 2013-present.
- Postdoctoral Associate, Earth and Environmental Sciences, Los Alamos National Laboratory, 2011-2013.
- Lecturer, Texas A&M University, 2009-2010.
- Graduate Research Assistant, Texas A&M University, 2007-2009.
- Graduate Teaching Assistant, Texas A&M University, 2005-2007.

Honors & Awards:

- Argonne Training Program on Extreme-Scale Computing (ATPESC) Scholar, 2013.
- Honorable Mention Award, Postdoc Research Day, Los Alamos National Laboratory, 2012.
- Outstanding Graduate Student Teaching Award, Department of Mechanical Engineering, Texas A&M University, 2010.
- Mechanical Engineering Graduate Fellowship, Department of Mechanical Engineering, Texas A&M University, 2005–06.
- '*Graduate Pool'* Graduate Fellowship, Department of Mechanical Engineering, Texas A&M University, College Station, 2005–06.
- Prathibha Scholarship, State Government of Andhra Pradesh, India, 2001–05.

Selected Publications:

- P.C. Lichtner and **S. Karra**, Modeling multiscale-multiphase-multicomponent reactive flows in porous Media: application to CO_2 sequestration and enhanced geothermal energy using PFLOTRAN, book chapter in Computational Models for CO_2 Sequestration and Compressed Air Energy Storage, Taylor & Francis/CRC press.
- **S. Karra**, S. Painter and P.C. Lichtner, Three-phase numerical model for subsurface hydrology in permafrost-affected regions. The Cryosphere, *in press*.
- S. Painter and **S. Karra**, Constitutive model for unfrozen water content in subfreezing unsaturated soils (2013). Vadoze Zone Journal, *in press.*
- **S. Karra**, Modeling the diffusion of a fluid through viscoelastic polyimides. Mechanics of Materials 66:120-133 (2013).
- K.C. Lewis, **S. Karra** and S. Kelkar, A model for tracking fronts of stress-induced permeability enhancement. Transport in Porous Media 99:17–35 (2013).
- **S. Karra** and K. R. Rajagopal, A model for degradation of polyimide due to oxidation. Mechanics of Time-dependent Materials 16:329–342 (2012).
- **S. Karra** and K. R. Rajagopal, Modeling the non-linear viscoelastic response of high temperature polyimides. Mechanics of Materials 43(1):54-61 (2011)
- **S. Karra** and K. R. Rajagopal, Development of three dimensional constitutive theories based on lower dimensional experimental data. Applications of Mathematics 54(2), 147–176 (2009).
- S. Kelkar, K. Lewis, **S. Karra**, G. Zyvoloski, S. Rapaka, H. Viswanathan, P.K. Mishra, S. Chu, D. Coblentz and R. Pawar, Modeling coupled thermo-hydro-mechanical processes in subsurface geological media using the simulator FEHM (2013). LA-UR-13-21444, *under review.*

Co-author of PFLOTRAN: P.C. Lichtner, G.E. Hammond, C. Lu, **S. Karra**, G. Bisht, B. Andre, R.T. Mills and J. Kumar, PFLOTRAN v2.0: A massively parallel reactive flow and transport code for describing surface and subsurface processes LA-CC-09-047.

Shari Kelley

Professional Preparation

New Mexico State University	Geological Sciences	B.S.	1979
Southern Methodist University	Geophysics	Ph.D.	1984

Appointments:

July 2010 – present: Senior geophysicist/ field geologist, New Mexico Bureau of Geology and Mineral Resources, Socorro, NM 87801.

July 2005 – July, 2010: Field geologist, web information specialist, New Mexico Bureau of Geology and Mineral Resources, Socorro, NM 87801.

January, 1995 - present: Adjunct Faculty, Department of Earth and Environmental Science, New Mexico Institute of Mining and Technology, Socorro, NM, 87801.

September, 1984 - January, 2005: Consulting geoscientist; fission-track analysis for ARCO, Amoco, Mobil, Cornell University, and University of Wyoming; geothermal resource evaluation, seismic data interpretation; geologic mapping.

January, 1987 - December, 1994: Adjunct Assistant Professor of Geological Sciences, SMU, Dallas, TX.

September, 1985 - May, 1986; September, 1988 - December, 1994: Part-time instructor, physical and historical geology, Richland Community College, Dallas, TX.

Related Publications:

Person, M., Phillips, F., Kelley, S., Timmons, S., 2013, Assessment of the Sustainability of Geothermal Development within the Truth or Consequences Hot-Springs District, New Mexico, New Mexico Bureau of Geology and Mineral Resources Open-file Report 551, 65 pp.

Huang, L, Kelley, S. Zhang, Z., Rehfeldt, K., Albrecht, M., Kaufman, G., 2011, Imaging faults with reverse-time migration for geothermal exploration at Jemez Pueblo in New Mexico: Los Alamos National Laboratory Report LA-UR-11-10640, 11 p.

Albrecht M., Goff F., Gardner J., Kelley S., WoldeGabriel G., Dewhurst W., Sirles P., Kaufman G., 2011: Multi-disciplined geothermal exploration at the Pueblo of Jemez, New Mexico, Proceedings, Geothermal Research Council Annual Meeting, California, San Diego, 2011.

Kelley, S.A., 2010, Geothermal energy: Lite Geology, no. 28, p.1-6.

Kelley, S.A., Chapin, C.E., Cather, S.M., and Person, M., 2009, Thermal history of the eastern Socorro Basin, Socorro County, New Mexico, based on apatite fission-track thermochronology: New Mexico Geological Society Guidebook 60, p. 121-132.

Other Publications:

Kelley, S.A., McIntosh, W.C., Goff, F., Kempter, K.A., Wolff, J.A., Esser, R., Braschayko, S., Love, D., and Gardner, J.N., 2013, Spatial and temporal trends in pre-caldera Jemez Mountains volcanic and fault activity, Geosphere, v. 9, p. 614-646.

Kelley, S.A. and Chamberlin, R.C., 2012, Our growing understanding of the Rio Grande rift: New Mexico Earth Matters, v. 12, no.2, p. 1-4.

Goff, Fraser; Gardner, Jamie N.; Reneau, Steven L.; Kelley, Shari A.; Kempter, Kirt A.; Lawrence, J., 2011, Geologic Map of the Valles Caldera, Jemez Mountains, New Mexico, New Mexico Bureau of Geology and Mineral Resources Geologic Map, GM-79, scale 1:50,000.

Cather, S.M., Chapin, C.E., and Kelley, S.A., 2012, Diachronous episodes of Cenozoic erosion in southwestern North America and their relationship to surface uplift, paleoclimate, paleodrainage, and paleoaltimetry*:* Geosphere, December 2012, v. 8, p. 1177-1206, first published on October 18, 2012, doi:10.1130/GES00801.1

Mark Person
Department of Earth & Environmental Sciences, NM Tech
MSEC 208, 810 Leroy Place, Socorro, NM 87801
575-835-5634 (voice), 575-835-6436 (fax), mperson@nmt.edu

Professional Preparation:

Franklin and Marshall College,	Geology	B.S.	1980
New Mexico Tech,	Hydrology	M.A.	1987
Johns Hopkins University,	Geology	Ph.D.	1990
Paris School of Mines	Hydrogeology	Post-doc.	1990-1991

Appointments:

2009-present Professor of Hydrology, New Mexico Tech
2001-2009 Boyce Chair of Geosciences, Professor of Hydrogeology, Indiana University
2000 Professor, University of Minnesota
1997-2000 Associate Professor, University of Minnesota
1993-2000 Gibson Hydrogeology Chair, University of Minnesota
1993-1997 Assistant Professor, University of Minnesota
Assistant Professor, University of New Hampshire

Five Publications Most Relevant to Proposed Activity:

Pepin J, Person M, Phillips F, Kelley S, Timmons S, Witcher J, and Gable C, 2014, Deep Fluid Circulation within Crystalline Basement Rocks and the Role of Hydrologic Windows in the Formation of the Truth or Consequences, New Mexico Low-Temperature Geothermal System, Geofluids, doi: 10.1111/gfl.12111.Bense V. F., M. A. Person, 2008, Transient hydrodynamics within intercratonic sedimentary basins during glacial cycles, J. Geophys. Res., 113, F04005, doi:10.1029/2007JF000969.

Person M. , Hofstra, A., Sweetkind, D, Stone, W., Cohen, D., Gable, C, Banerjee, A. 2012, Analytical and numerical models of hydrothermal fluid flow at fault intersections, Geofluids, v. 12, p. 312–326.

Person M, Kelley S, Kelley R, Karra S, Harp D, Witcher J, Bielicki J, Sutula G, Middleton R, Pepin J, 2015, Hydrogeologic Windows: Detection of Blind and Traditional Geothermal Play Fairways in Southwestern New Mexico Using Conservative Element Concentrations and Advective-Diffusive Solute Transport, Geothermal Research Council Annual Meeting, September 22, 2015, Reno NV.

Witcher J, Person M, Kelley S, Kelley R, Karra S, Harp D, Bielicki J, Sutula G, Middleton R, Pepin J, 2015, Hydrogeologic Windows: Detection of blind and traditional geothermal play fairways in southwestern NM, New Mexico Geological Society Annual Meeting, Socorro NM, April 24, 2015.

Howald T, Person M, Campbell A, Lueth V, Hofstra A, Sweetkind D, Gable CW, Banerjee A, Luijendijk E, Crossey L, Karlstrom K, Kelley S, and Phillips F, 2014. Evidence for Long-Time Scale (> 10^3 years) Changes in Hydrothermal Activity Induced by Seismic Events, Geofluids, doi: 10.1111/gfl.12113.

Other Publications:

Person, M., Banerjee, A., Hofstra, D., Sweetkind, D., and Y. Gao, 2008, Hydrologic Models of Modern and Fossil Geothermal Systems withinin the Great Basin: Implications for Carlin-Type Gold Mineralization, Geosphere, vol. 4, no. 5, p.888-917.

Banerjee, A. Person, M., Hofstra, A., Sweetkind, D., Cohen, D., Unruh, J., Zyvoloski, G., Gable, C. W., Crossey L., and K. Karlestrom, 2011, Fault Controlled Helium Transport and Fluid-Rock Isotope Exchange In the Great Basin, USA, Geology, v. 39, p. 195-198.

Mailloux, B., Person, M., Strayer, P., Hudleston, P.J., Cather, S., Dunbar, N., 1999, Tectonic and Stratigraphic Controls on the Hydrothermal Evolution of the Rio Grande Rift, *Water Resources Research*, v. 35(9), p. 2641-2659.

Person, M. Cohen, D., Sabin, A, Unruh, J. Gable, C., and G. Zyvoloski, 2006, Isotope Exchange and Transport in the Coso Geothermal System, Geothermal Resources Council, GRC Annual Meeting 2006, Geothermal Resources-Securing Our Energy Future, Volume 1, GRC Transactions, Volume 30.

Person, M. Mulch, A. Teyssier, C. and Y. Gao, 2007, Isotope transport and exchange within metamorphic core complexes, *American Journal of Science*, v. 307, p. 555-589.

James Witcher

Witcher and Associates P. O. Box 3142, Las Cruces, NM 88003
Phone: (575) 521-0146 cell: (575) 649-4893 e-mail: jimwitcher@zianet.com

EDUCATION:
New Mexico Military Institute
New Mexico State University, B.S.
New Mexico State University, M.S.

EXPERTISE:
Exploration geology and geophysics; geologic mapping; terrestrial heat flow; soil radon occurrence and transport; hydrogeology of geothermal systems; inorganic aqueous geochemistry; forensic isotope hydrogeology; economic geology of geothermal resources; direct-use geothermal utilization and geothermal aquaculture and greenhouses; slim-hole geothermal well drilling operations; development of exploration models and methods for geothermal resources; regional geology of the southwestern United States and Rio Grande rift; ground-water hydrogeology; sources of salinity in groundwater and rivers

EXPERIENCE:
2005-2015 **Consultant and Principal**, Witcher and Associates, Las Cruces, NM
1995-2015 **Adjunct Faculty**, Geosciences Department, College of Arts and Sciences, New Mexico State University, Las Cruces
1986-2006 **Geothermal Projects Manager**, Southwest Technology Development Institute, Engineering College, New Mexico State University, Las Cruces, NM
1983-1986 **Geologist**, Stone and Witcher, Tucson, AZ
1977-1983 **Geologist**, Arizona Bureau of Geology and Mineral Technology, University of Arizona, Tucson, AZ

RELEVANT PUBLICATIONS:
Mack, G. H., Jones, M. C., Taylor, N. J., Ramos, F. C., Scott, S. R., and **Witcher, J. C.**, 2012, Mixed geothermal and shallow meteoric origin of opal and calcite beds in Pliocene-lower Pleistocene axial-fluvial strata, southern Rio Grande rift, Rincon Hills, New Mexico, USA: Journal of Sedimentary Research, v. 82, p. 616-631.

Szynkiewicz, A., **Witcher, J. C**., Modelska, M., Borrok, D. M., and Pratt, L. M, 2011, Anthropogenic sulfate loads in the Rio Grande, New Mexico (USA): Chemical Geology, v. 283, p. 194-209.

Morgan, P., and **Witcher, J. C**., 2011, Geothermal resources along the southern Rocky Mountains and the Rio Grande rift: The Mountain Geologist, v. 48, no. 4, p. 81-94.

Witcher, J. C., 2008, Evidence for large-scale Laramide tectonic inversion and a mid-Tertiary caldera ring fracture zone at the Lightning Dock geothermal system, New Mexico: New Mexico Geological Society 59th Annual Fall Field Conference Guidebook, p. 177-187.

Witcher, J. C., King, J. P., Hawley, J. W., Kennedy, J. F., Williams, J., Cleary, M., and Bothern, L. R., 2004, Sources of salinity in the Rio Grande and Mesilla Basin groundwater: New Mexico Water Resources Research Institute Technical Report 330, 168 p.

O'Donnell, T. M., Miller, K. C., and **Witcher, J. C**., 2001, A seismic and gravity study of the McGregor geothermal system, southern New Mexico: Geophysics, v. 66, no. 4, p. 1002-1014.

Witcher, J. C., 1991, The Rincon geothermal system, southern Rio Grande rift, New Mexico: a preliminary report on a recent discovery: Transactions, Geothermal Resources Council, v. 15, p. 205-212.

Witcher, J. C., 1988, Geothermal resources in southwestern New Mexico and southeastern Arizona, <u>in</u> Cretaceous and Laramide Tectonic Evolution of Southwestern New Mexico: New Mexico Geological Society 39th Annual Field Conference Guidebook, p. 191-197.

Witcher, J. C., Stone, C., and Hahman, W. R., 1982, The Geothermal Resources of Arizona: U. S. Department of Energy and the State

PROFESSIONAL AFFILIATIONS
New Mexico Geological Society (President, 1997 and Honorary Member, 2001)
Four Corners Geological Society
The Geological Society of America
Geothermal Resources Council
American Geophysical Union
Association of Ground Water Scientists and Engineers
Society of Economic Geologists

Section 5. Appendix B (Hydrothermal Model Results)

This appendix discusses two additional cross-sectional hydrothermal model output for San Acacia and Acoma.

5.1 San Acacia

For the San Acacia model which overlies the Socorro magma body, the cross section was extended to 20 km depth in order to represent higher heat flow conditions associated with the Socorro magma body. The model cross section runs east-west (Figure 5-1). There are a number of shallow wells that could be used to collect temperature and ^{14}C age dates during Phase 2. We tripled the heat flow beneath the Socorro magma body (240 mW/m^2). There are numerous confining units of different ages within the basin fill that restrict vertical circulation. This cross section also contains several faults zones. These fault zones were not represented in the current model due to time limitations. However, these features could serve as hydrogeologic windows. The boundary conditions imposed in these models is schematically illustrated in Figure 2-15. Due to the higher heat flow, two thermal convection cells formed above the magma body (Figure 5-2A). Vertical flow rates varied between -1.4 to 0.7 m/yr. The convection cells produced complex temperature patterns (Figure 5-2B) with little focused groundwater discharge or recharge across the hydrogeologic window located on the top east side of the cross section. Groundwater ages were much older than in other models as little inflow of young groundwater occurred (Figure 5-2C). These “closed” convection cells had much older groundwater ages on the order of several hundreds of thousands of years (^{14}C dead). No distinct outflow zone formed within the San Acacia model (Figure 5-2C). The thermal boundary condition we used were highly idealized. We are currently conducting a magnetotelluric survey across an east-west transect that follows our model cross section. This should reveal the presence of any magmatic body.

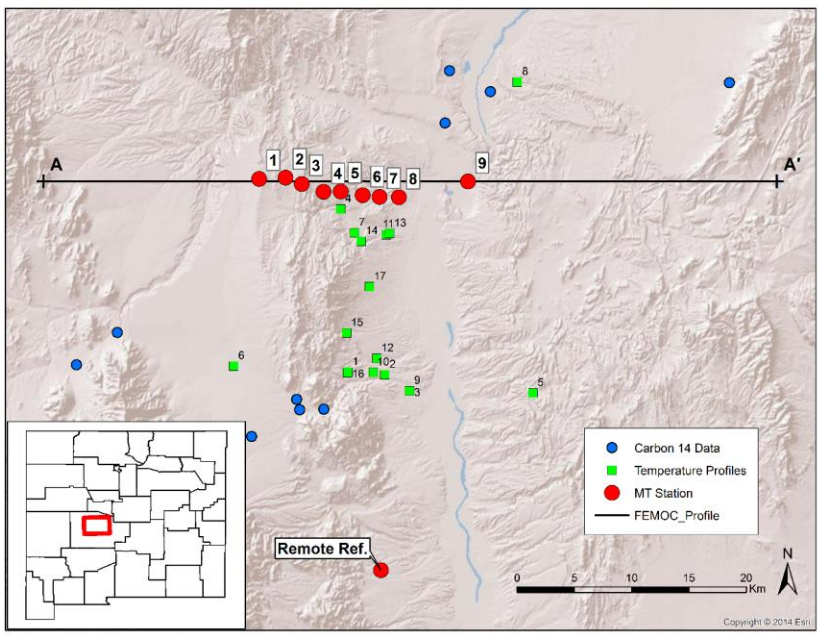

Figure 5-1: Base map showing location of hydrothermal cross sectional model for the San Acacia area. The red dots denote magnetotelluric stations that will be used to provide ground truth for the hydrothermal model during Phase 2. The green squares denote the location of temperature profiles that will be used to calibrate the models. Data from points 4, 7, 14, 13, 11 will be used in the model calibration exercise during Phase 2. Blue dots denote the locations of carbon-14 age data which will be used to calibrate the model.

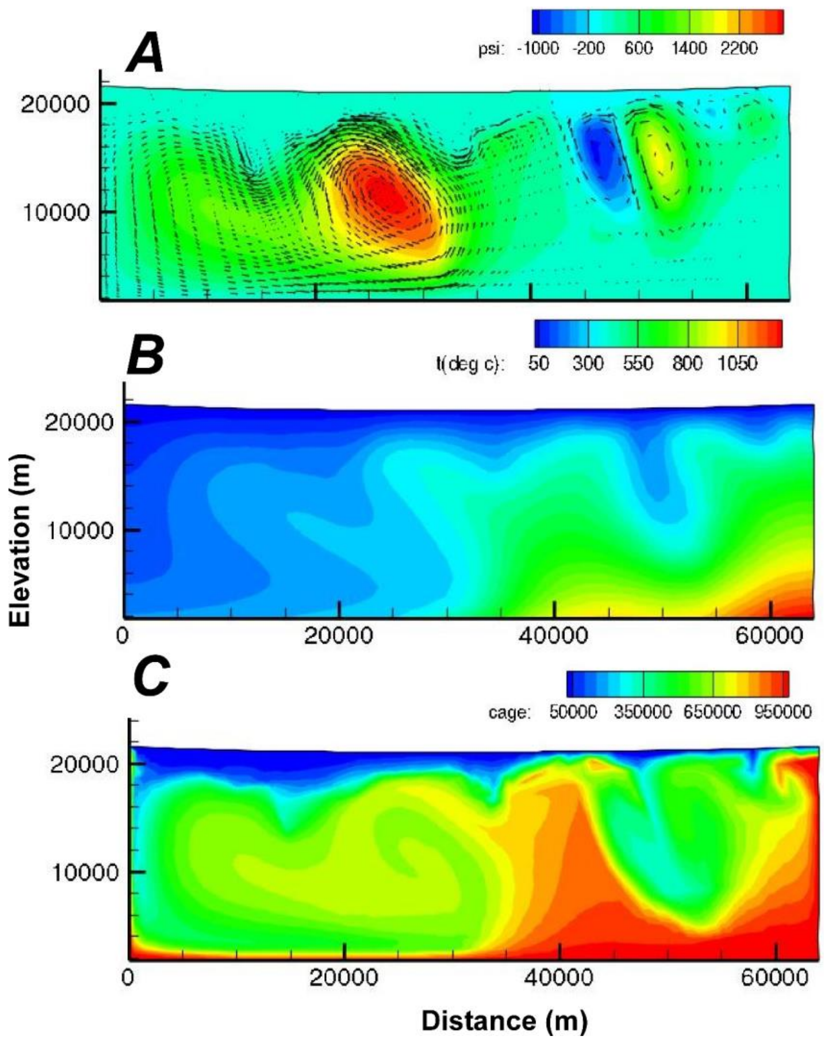

Figure 5-2: Cross sectional model of San Acacia geothermal system. (A) Computed stream functions (in m2/yr), (B) temperature (oC), and (C) groundwater residence times.

5.2 Acoma

For the Acoma Pueblo region, groundwater flow is predominately eastward towards the Rio Grande from Mt Taylor to the north and Mt Sedgwick to west (Figure 5-3) Along the Comanche Fault, there are several zones with elevated boron or to the east, perhaps along a volcanic dike (Figure 2-22). The basal heat flux in the model was uniformly set to 80 mW/m^2 for the Acoma model. In this model, crystalline basement permeability was 10^{-13} m^2. The sedimentary confining units were assigned a permeability of 10^{-17} m^2. A permeable dike was assigned a permeability of 10^{-13} m^2. The models cross section includes a region to the east of the Comanche fault zone where Precambrian basement crops out (Figure 2-15). Within the recharge area, computed temperatures are cooler than background values due to descending groundwater flow (Figure 5-4A). Groundwater discharge area temperatures within the hydrogeologic window are about 40 ^{o}C (Figure 5-4B). Groundwater flow resulted in shallow discharge of relatively saline fluids (about 90 ppt or 0.09 solute mass fraction; Figure 5-4C). This simulated concentration is too high suggesting our initial condition of increasing salinity with depth was too high. Groundwater residence time of 78,000 years (not shown) occur within the groundwater discharge area suggesting that warm spring waters would be carbon dead. Preliminary results from the Acoma Pueblo model are encouraging, in that they predict that a solute outflow plume was produced down adjacent to the crystalline basement hydrogeologic window at Acoma. We did not include permeable fault zones in the model shown in Figure 5-4. We plan to do this during phase 2. There are some shallow gradient holes that can be used to calibrate the Acoma model (Figure 5-3).

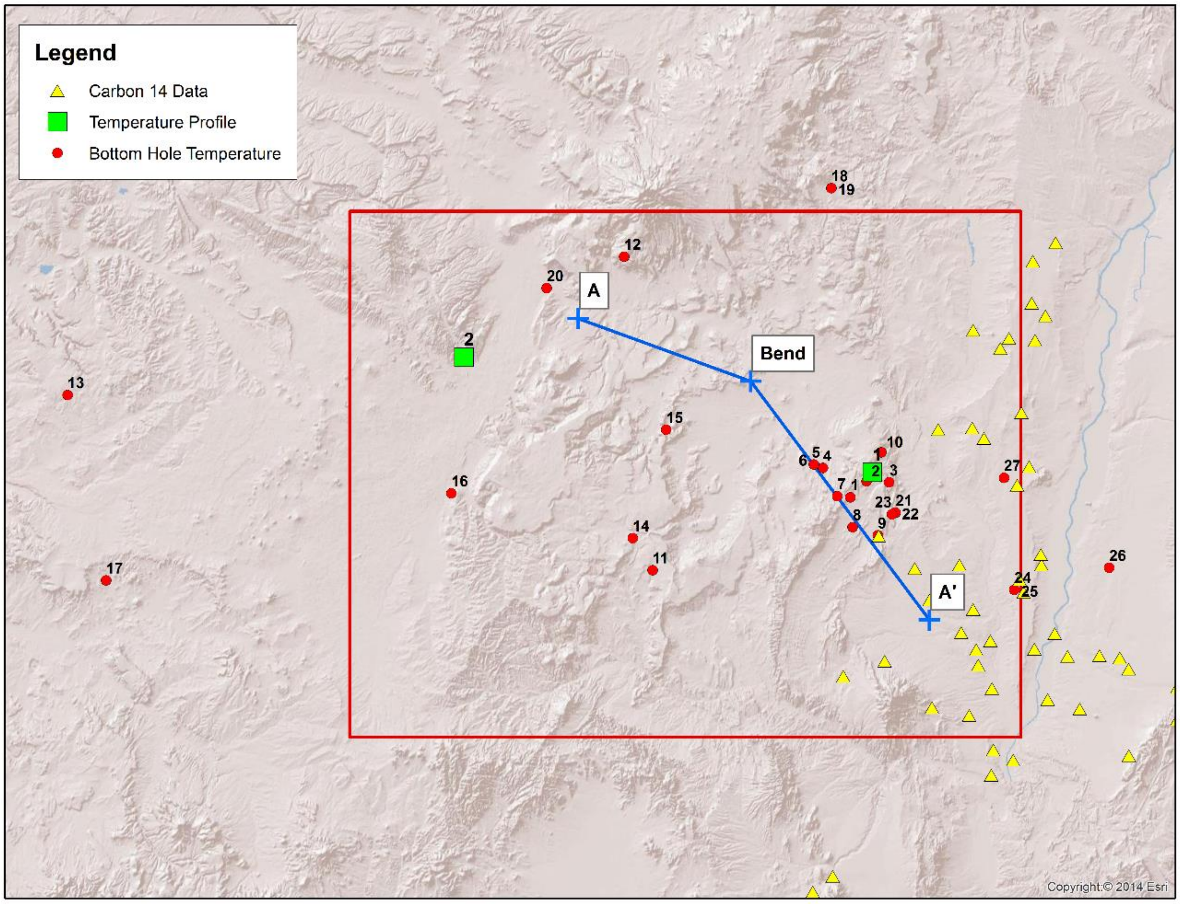

Figure 5-3: Base map showing location of cross-sectional hydrologic model for the Acoma Pueblo area. The green squares denote temperature-depth profiles data while the red circles denote bottom hole temperatures. Data from points 20, 5, 4, 7, 1, 6, 8, 9 will be used in the model calibration exercise. The yellow triangles show the location of carbon-14 age data that will be used to calibrate the hydrothermal model.

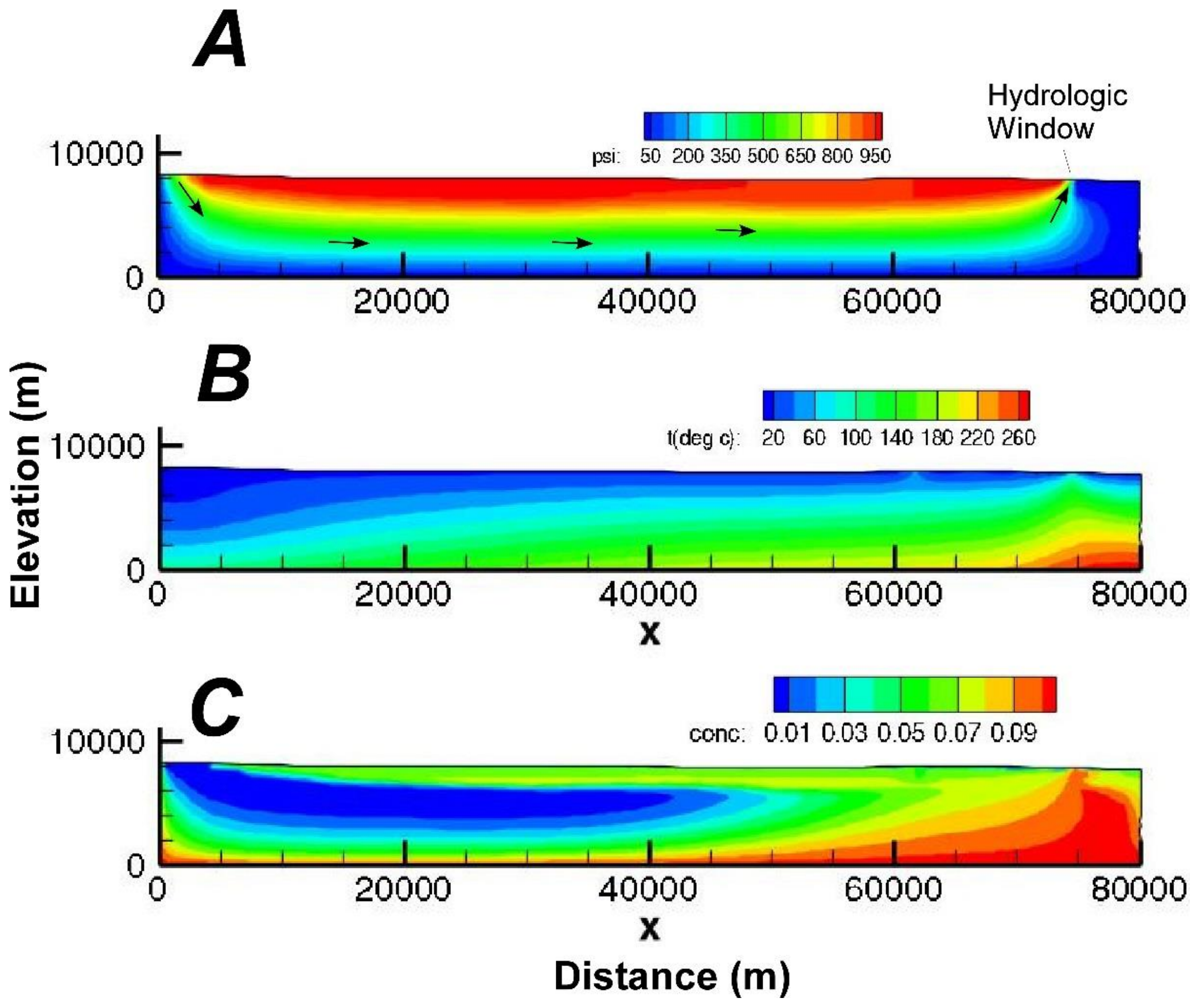

Figure 5-4: Hydrothermal model results for Acoma Pueblo cross sectional model after 1 Myr. (A) Computed stream functions (in m2/yr), (B) temperature (oC), and (C) total dissolved solids concentration (mass fraction).

Section 6. Appendix C (Particle-tracking Results)

In this appendix we present particle-tracking results are discussed for the Rincon, San Acacia, Las Cruces East Mesa, and Truth or Consequences areas.

6.1 Rincon-Radium Springs Region

For the Radium Springs (inset, Figure 6-1) area, high boron concentrations in wells are correlated with regions of high heat flow. There is a hydrogeologic window at Radium springs are associated with fractured permeable dikes (Witcher, 2001). Geothermal well temperatures at the Mason Greenhouse at Radium Springs range between 80-87 ^{o}C at less than 330 m (Witcher, 2001). While the well density is relatively high, there is a paucity of wells up hydrologic gradient of the region of known high heat flow at Radium Springs.

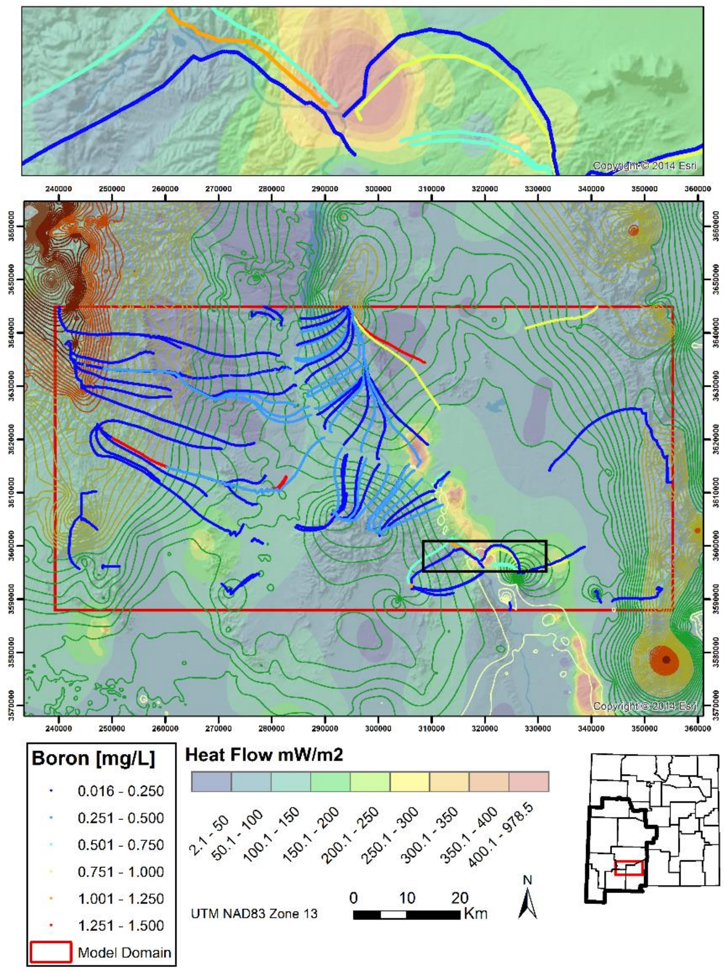

Figure 6-1: Boron particle trajectories for the Rincon region (colored lines) heat flow (shaded color patterns), and fault locations (black lines). Inset shows particle trajectories near the Radium springs geothermal prospect. Heat flow is shown using the shaded (red to blue) patterns.

For the Radium Springs (inset, Figure 6-2) area, high boron concentrations in wells are correlated with regions of high heat flow. There is a hydrogeologic window at Radium springs associated with fractured permeable dikes (Witcher, 2001). Geothermal well temperatures at the Mason Greenhouse at Radium Springs range between 80-87 ºC at less than 330 m (Witcher, 2001). While the well density is relatively high, there is a paucity of wells up hydrologic gradient of the region of known high heat flow at Radium Springs.

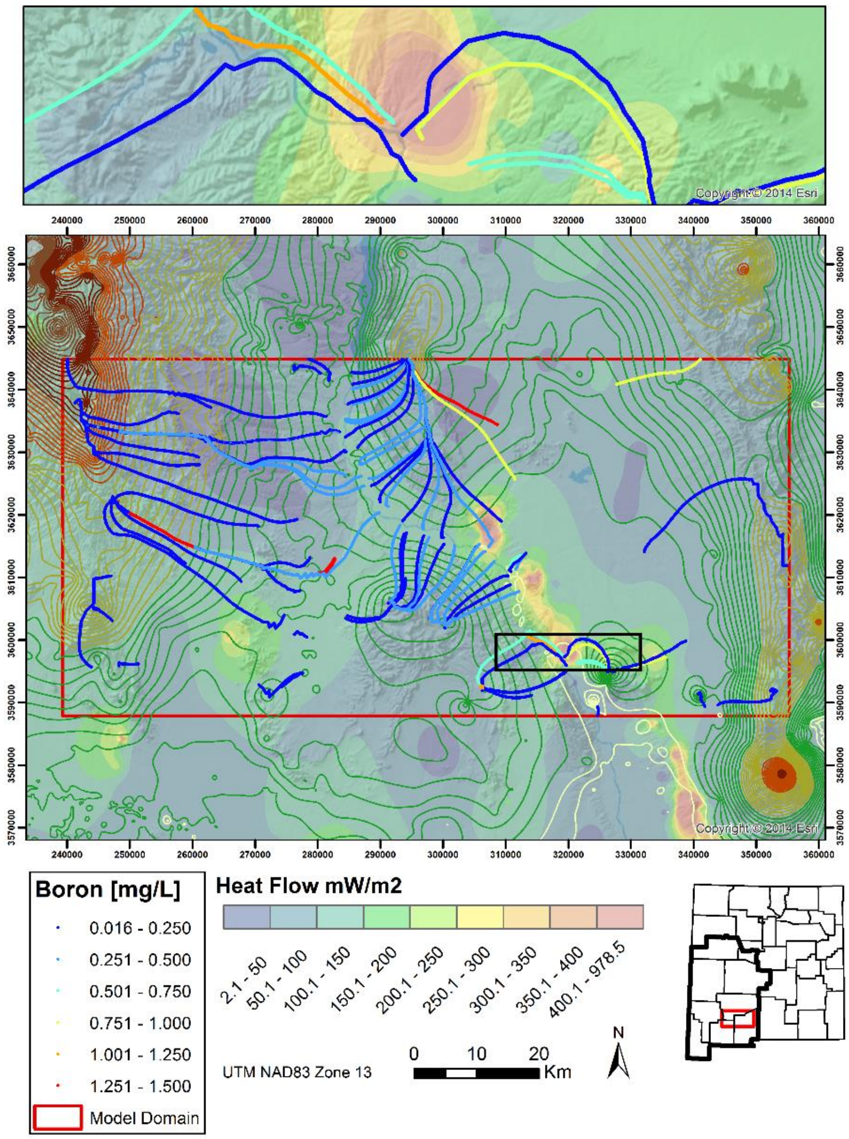

Figure 6-2: Boron particle trajectories for the Rincon region (colored lines) heat flow (shaded color patterns), and fault locations (black lines). Inset shows particle trajectories near the Radium springs geothermal prospect. Heat flow is shown using the shaded (red to blue) patterns.

6.2 San Acacia Region

The San Acacia region is an area of active seismicity and uplift. Geodetic measurements indicate ongoing dome-like surface uplift encompassing the Socorro magma body. The uplift is considered to be a result of thermal expansion and magma injection into the Socorro magma body. Previous studies based on historic leveling data and traditional geodetic surveys from 1911 to 1981 estimate uplift is occurring at the surface on the order of a few millimeters per year (Larsen and Reilinger, 1983). Subsequent studies using fifteen years of satellite data show that uplift persists at a rate up to 2-3 mm/yr (Fialko and Simmons, 2001; Pearse and Fialko, 2010; Figure 6-4). These localized uplift results are comparable in magnitude to lateral strain rates (~3 mm/yr) reported by Kennedy and van Soest (2007) for the Baisn and Range Province, which has elevated primordial helium signatures and enhanced fluid flow rates. Thus, this region is considered a prospective geothermal target albeit with limited available data. As part of an NSF grant to Mark Person and Shari Kelley, we have recently completed an east-west magnetotelluric transect across the center of the magma body. Along the Rio Grande rift near San Acacia on the Sevilleta Wildlife Refuge, elevated boron concentrations (> 3 mg/l) occur in wells in the vicinity of Indian Wells spring (inset, Figure 6-3). Both up gradient and down gradient wells have lower boron concentrations, suggesting this may be an up flow zone associated with a hydrogeologic window or fault system overlying the Socorro magma body. Indian Wells spring also has elevated $^3He/^4He$ ratios, suggesting a potential deep geothermal fluid source (Williams et al., 2013). Because this region is the southern terminus of the Albuquerque Basin, up flow of deep sedimentary basin fluids may also occur in this area (Hogan et al., 2007).

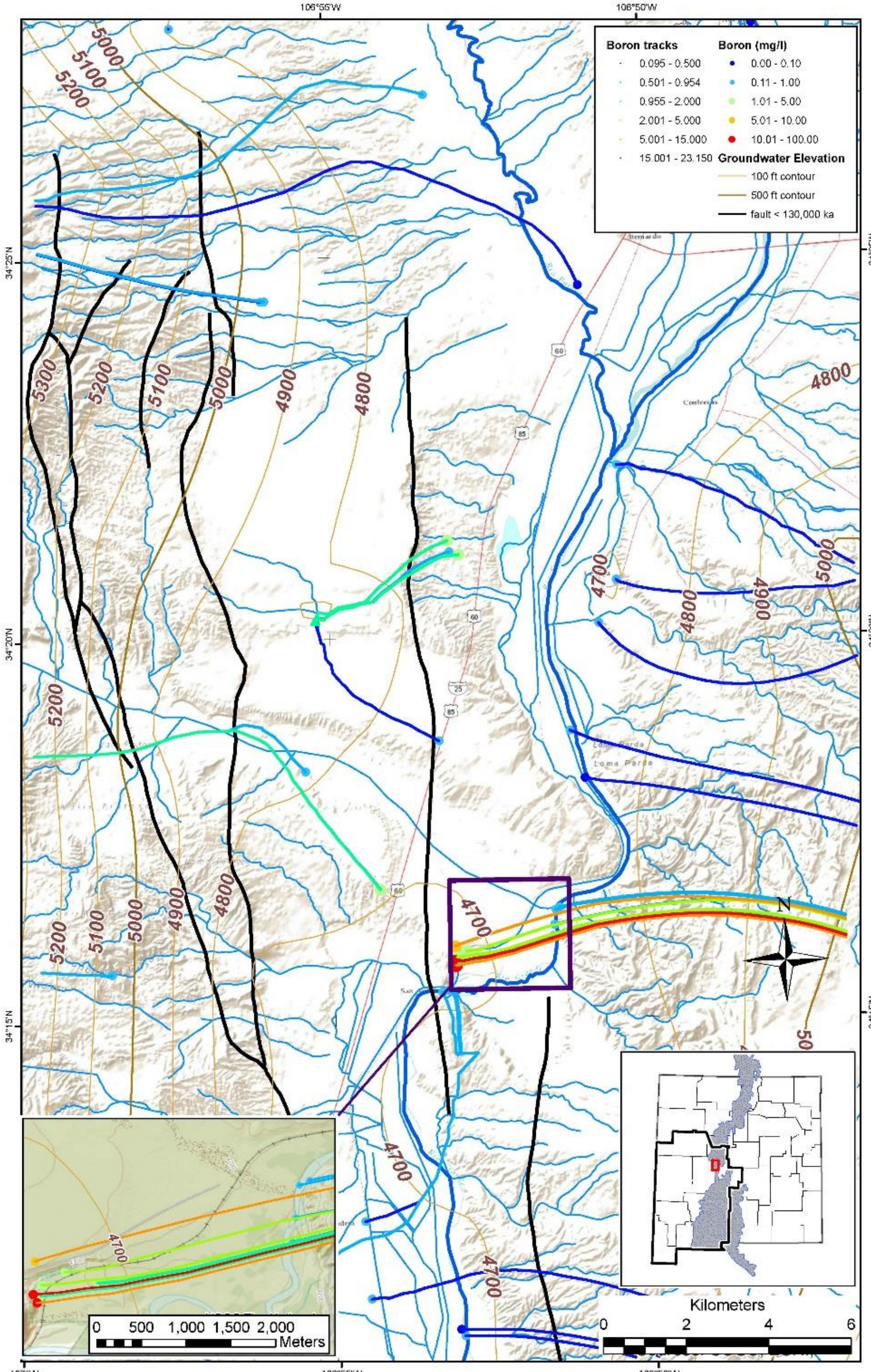

Figure 6-3: Boron particle trajectories for the San Acacia region (colored lines) overlying the Socorro magma body as well as fault locations (black lines). Inset shows particle trajectories in the vicinity of Indian Wells spring.

6.3 Las Cruces East Mesa Region

Legacy oil wells drilled in 1949 on the New Mexico State University campus encounter warm water and boiling conditions (Witcher, 2002a). Hot water (~ 63 ºC) as shallow as 10m depth have been encountered in productive sand horizons (Witcher, 2002a). In the 1990s, the NMSU campus began to utilize this hot water in a district heating system utilizing this resource. The Las Cruces East Mesa region has the highest density of wells of our 7 sites. Many of these are situated along the Rio Grande (Figure 6-4). There is some correlation between wells with high boron concentration and areas of high heat flow. Down gradient wells near the Rio Grande tend to have low boron concentrations. However, the correlations are not strong. That is, regions of highest heat flow do not strongly correlate to wells with highest boron concentrations. There is a paucity of up gradient wells to the east of the high heat flow areas.

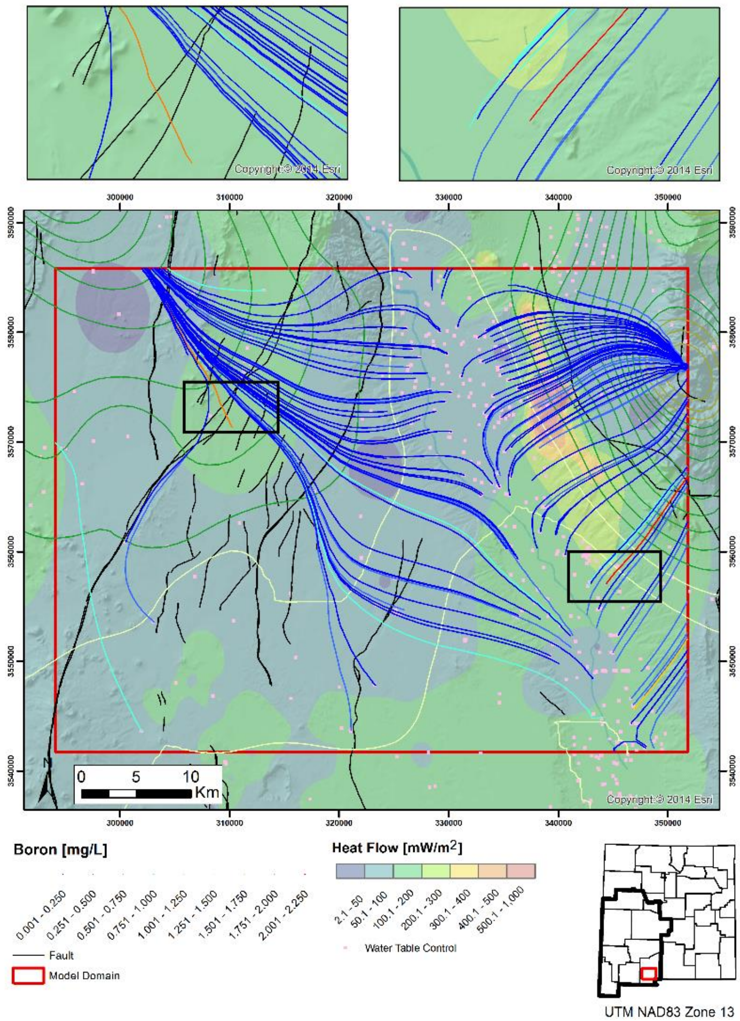

Figure 6-4: Boron particle trajectories for the Las Cruces – East Mesa region (colored lines). The inset shows particle trajectories in the vicinity of the NMSU campus. Heat flow is shown using the shaded (red to blue) patterns.

6.4 Truth or Consequences Region

Proterozoic bedrock crops out at the land surface within the hot springs district of Truth or Consequences (formerly known as Hot Springs, NM; Theis et al. 1939). Temperature within the bedrock reach 40 ºC within 20m of the land surface in a number of wells. Temperatures are isothermal below this depth suggesting this is an upflow zone. Pepin et al. (2013) used hydrothermal models contrained by ^{14}C ages and temperatures to estimate the crystalline basement permeability was about 10^{-12} m^2 (1000 mD) at depth up to 8 km. An aquifer test conducted this summer indicated the permeability of the shallow crystalline basement was 530,000 mD ($5x10^{-10}$ m^2). The Truth or Consequences hot-springs district has elevated lithium (up to 1.3 mg/l) and boron (up to 3.9 mg/l) concentrations in wells completed within a hydrogeologic window along the Rio Grande (Figure 6-5), where bedrock crops out near the land surface or is covered by a thin veneer of fluvial deposits. The boron particle trajectories track up gradient to the west and south. The well density if relatively low, down gradient wells to the south of the hot-springs district and up hydrologic gradient near the Elephant Butte Reservoir have lower lithium concentrations. There are also some wells with elevated boron concentrations along Alamosa Creek to the north and west of Truth or Consequences (to the west of the symbol, CA).

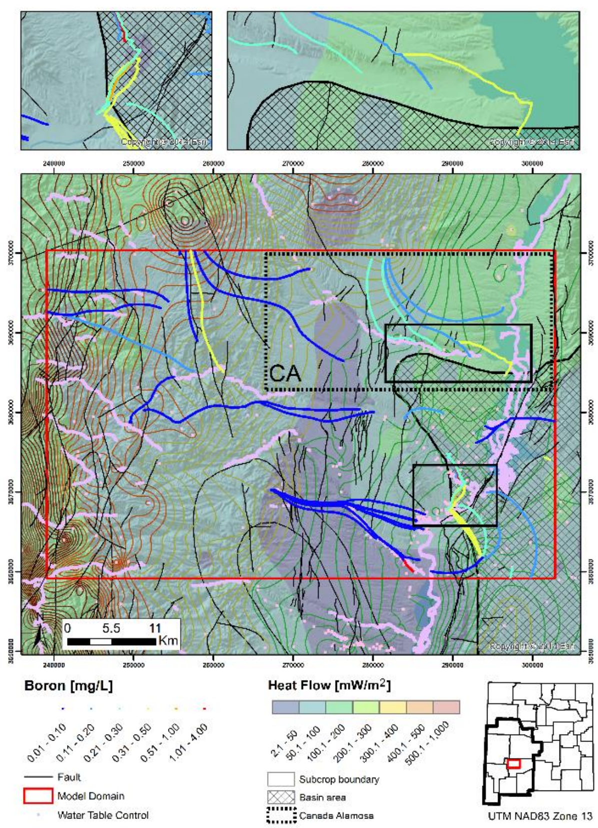

Figure 6-5: Boron particle trajectories for the Rincon region (colored lines) heat flow (shaded color patterns), and fault locations (black lines). Inset shows particle trajectories near the Truth or Consequences geothermal prospect. Heat flow is shown using the shaded (red to blue) patterns.